UNIVERSITY OF OKLAHOMA

GRADUATE COLLEGE

EVALUATION OF TURBULENCE MODEL PERFORMANCE FOR SIMULATION OF
LOW PRANDTL NUMBER FLUIDS IN NUCLEAR REACTOR COOLING SYSTEMS

A THESIS

SUBMITTED TO THE GRADUATE FACULTY

in partial fulfillment of the requirements for the

Degree of

MASTER OF SCIENCE

By

William Daniel Jock

Norman, Oklahoma

2020

EVALUATION OF TURBULENCE MODEL PERFORMANCE FOR SIMULATION OF
LOW PRANDTL NUMBER FLUIDS IN NUCLEAR REACTOR COOLING SYSTEMS

A THESIS APPROVED FOR THE

SCHOOL OF AEROSPACE AND MECHANICAL ENGINEERING

BY THE COMMITTEE CONSISTING OF

Dr. D. Keith Walters, Thesis Advisor

Dr. Ramkumar Parthasarathy

Dr. Feng Lai

ABSTRACT

Nuclear energy is a promising alternative to fossil fuel energy sources. With advances to current cooling technology, nuclear energy can achieve more energy production and run more efficiently than earlier reactor designs. Advances in cooling technology require new coolants, and for the nuclear industry one option for these come in the form of liquid metals. Liquid metals have potential to substantially improve cooling performance, however the behavior of such fluids has not been studied in depth due to the difficulties that lie in experimenting with these fluids. With computational advances, simulation is often the best option for predicting fluid flows. Due to the low Prandtl number (Pr) of liquid metals, modeling is somewhat challenging as traditional models do not accurately predict the turbulent heat transfer behavior of low Pr fluids. Although some research has been conducted for low Pr fluid simulation, the answer to which model to use for these fluids is not entirely clear. This document seeks to implement traditional eddy viscosity RANS models within a CFD simulation code and evaluate them based on their ability to accurately simulate simple heat transfer processes involving low Pr fluids. The study also seeks to quantify the potential improvement of Kays formulation, a turbulent thermal diffusivity modification, within those models. Computational simulations were performed for channel flow, backward facing step flow, and a simple rod bundle geometry to test the applicability and validity of these models. Simulations were run for values of Pr comparable to air like fluids and low Pr comparable to liquid metals, and all results were compared to DNS or experimental data available for the test cases selected. The results of this study show that typical unmodified k-ε models do not consistently provide accurate results for low Pr fluid flows. The addition of Kay's formulation shows a general improvement on the baseline models. More complex models may

benefit more than the simple models tested here and improve results by implementing Kay's

formulation.

ACKNOWLEDGEMENTS

TABLE OF CONTENTS

Page

LIST OF FIGURES

LIST OF TABLES

NOMENCLATURE

English Letters and Symbols

f_i user specified forcing term

g acceleration due to gravity

G_b buoyancy production

k turbulent kinetic energy

k_T thermal conductivity

p effective pressure

q_j turbulent heat transfer

S_{ij} rate-of-strain tensor

ske $S*k/\varepsilon$

T temperature

U_i mean velocity field

y location along the y-axis

Greek Letters and Symbols

β coefficient of thermal expansion

δ_{ij} Kronecker delta

ε turbulent dissipation rate

ρ density

υ kinematic viscosity

υ_T eddy viscosity

τ_{ij} turbulent stress tensor

INTRODUCTION

Liquid metals are of increasing engineering interest for their heat transfer capabilities. These fluids have been developed to create new kinds of cooling systems, especially in the energy industry regarding the so-called Gen-IV nuclear reactors (Abram and Ion, 2008). The thermal conductivities of such liquids offer an advantage to traditional coolants. These fluids also have substantially higher boiling points than traditional coolants such as water, thus maintaining a single phase while still offering relatively high heat transfer rates (Heinzel et al., 2017). Though the amount of energy required to pump these fluids reduces overall economy, the fluids still show excellent potential for improvements to fast reactor technology. Liquid metals have a high ratio of thermal-to-momentum diffusivity, i.e. they are low Prandtl number (Pr) fluids. Nuclear energy constitutes a significant portion of today's energy demands, and this reliance on reactors is pushing research in cooling technology. Experimentation on cooling configurations can quickly become costly, and efficient coolants, including liquid metals, can be expensive, toxic, and difficult to deal with in a laboratory environment. Computational methods provide a potential cost-effective alternative to experimentation, specifically the use of computational fluid dynamics (CFD) for reactor cooling system design is being used with increasing frequency and confidence.

Reactor cooling systems typically operate at Reynolds numbers (Re) high enough that the flow is turbulent. Accurate and efficient simulation of turbulent flow is a key challenge for CFD simulations. Computational methods that seek to resolve all or most of the fluctuating turbulent flow field, such as Direct Numerical Simulation (DNS) and Large Eddy Simulation (LES), are in theory highly accurate, but are generally considered too computationally expensive to be used effectively for large-scale analysis and design. An alternative approach is to simulate only the mean (time-averaged) flow field, and to include the effect of turbulence via statistical modeling.

The most common approach is to use Reynolds-averaged Navier-Stokes simulation, and to model the effect of turbulent mixing using an effective ("eddy") viscosity. Compared to DNS and LES, RANS models offer several advantages, chief among them computational cost. RANS models also are quite simple to implement without offering significant trade-offs in accuracy for most simple flows. RANS models have therefore become the most used turbulence modeling approach for CFD simulation of cooling systems.

Low-Pr fluids offer unique challenges for RANS models, which have been almost universally developed for use with fluids with Pr close to unity, such as water or air. The thermal diffusivity and thermal boundary layer of low Pr fluids are significantly larger than the viscosity and momentum boundary layer, respectively. In addition, the smallest scale fluctuations are much smaller in the momentum field when compared to the temperature field, because the small-scale thermal fluctuations are "smeared out" due to the thermal diffusivity being so high. These eccentricities of low Pr fluids pose clearly significant challenges to modeling these fluids using CFD. The Reynolds analogy forms the basis for most RANS models. The analogy considers that in typical fluid flow heat flux and momentum flux must be proportionally constant. This assumption, however, is only valid for Pr~1 and assumed for values close to 1 as well, for instance with Pr≈0.71 which is the value for air.

The objective of this paper is to implement traditional eddy viscosity RANS models within a CFD simulation code and evaluate them based on their ability to accurately simulate simple heat transfer processes involving low Pr fluids. Baseline RANS models will be compared to modified models which make use of a variable turbulent Prandtl number as a possible improvement to the accuracy of the heat transfer simulations. One method to do this is to modify the value of the turbulent ("eddy") thermal diffusivity using the effect of low Pr on the fluctuating temperature and

velocity fields to lower the modeled turbulent scalar transport. This method is known as Kays formulation (Kays, 1994), and it is compared and contrasted with traditional RANS models.

Literature Review

Data Comparison

Compared to fluids with Pr~1 such as air and water, a relatively small amount of work has been done to investigate low-Pr fluids, however, there has been some significant progress into understanding and modeling these fluids. Computationally, several simulations have been performed for channel flows at relatively low Reynolds numbers. These DNS results provide insight into key differences between low-Pr fluids and a Pr~1 fluid and provide a database for the validation of other turbulence modeling approaches, including RANS.

Kasagi and Ohtsubo (1993) ran DNS for a Re=150, equal and constant wall heat flux, plane channel flow case for a low-Pr fluid. The case matched that of Kasagi et al. (1992) by replicating the simulation, only with a low molecular Pr=0.025. Kasagi and Ohtsubo (1993) showed that the thermal streaks that are developed in low-Pr flows are not as elongated and have larger separation as opposed to those that develop in air. Kawamura et al. (1999) continued to build on available DNS data for low Pr fluids, simulating turbulent channel flows for Re=180 and Re=395 for both a standard air Pr, = 0.71, and a low Pr. Abe et al. (2004) investigated even higher Re, up to Re=1020 for the same boundary conditions.

Asymmetric heat flux boundary condition simulations with low-Pr fluid were conducted by Kasagi and Iida (1999). Simulations were carried out at Re=150 in three different configurations, the first being independent of buoyancy. The other two are horizontal geometries, including buoyancy effects, one with stable boundary conditions, the hot wall above the cool wall,

and the other unstable. Kasagi and Nishimura (1997) also conducted a simulation for a vertical asymmetric heat flux boundary channel.

More complicated geometries for flows utilizing low-Pr fluids were also tested both experimentally and numerically. Vogel and Eaton (1985) set up an experimental backward facing step with low Pr. Niemann and Frohlich (2016) ran DNS of a backward facing step with and without buoyancy.

Though all the previously mentioned work does not address the lack of research into turbulence modeling for low-Pr fluids, the data compiled from the aforementioned papers is used for comparison in this document to evaluate the performance of the turbulence models tested. All channel cases had data available from an online repository with the exception of the horizontally stable buoyancy case from Kasagi and Iida (1999). In that case the data used for comparison here was digitized from the published paper. Likewise, the data for the backward facing step cases was not available and therefore digitized from the respective documents.

Previous Studies

A few studies have been performed to address the lack of research for modeling low-Pr flows. Thiele and Anglart (2013) ran a simple annular geometry with one heated wall using the low-Pr fluid lead-bismuth eutectic. Turbulence models implemented include the Launder and Sharma k-ε model, Menter's k-ω-SST model (MKW), (Menter, 1994), and q-c, (Gibson and Dafa'Alla, 1995). For all models, however, the value of the turbulent Pr was carefully selected beforehand, rather than having a variable turbulent Pr based on flow characteristics. Based on the results, the k-ε and k-ω-SST simulations were more accurate than the q-c model. However, because of the sensitivity of these models to the molecular Pr, more research is required.

Maciocco (2002) shows that for heavy liquid metals with low Pr, typical wall-functions in commercial CFD codes are not suitable. Maciocco (2002) goes on to conclude, after a variety of tests, that k-ε is a promising model for low Pr flows, however still proposes that the model needs additional work, more specifically a variable turbulent Pr, which would more accurately address the discrepancy from the Reynolds analogy.

Kozelkov et al. (2015) ran simulations for a backward facing step, and implemented four models including k-ε, k-ω-SST, AKN (Abe and Kondoh, 1994) and (Abe and Kondoh, 1995), and S&S (Sommer et al., 1992) models. The AKN and S&S models are variations on the k-ε model, which include additional equations to compute turbulent heat fluxes and turbulent Pr as a function of thermodynamic parameters. Both Koazelkov et al. (2015) and Grötzbach (2013), which discusses the challenges involved with modeling low Pr fluids, mention that due to the difficulty of experimentation on liquid metals more work is required to develop RANS models for low-Pr fluids, however, hybrid LES-RANS models may be the best option in future of low Pr modeling.

Ge et al. (2017) compares the effects of six different turbulent Pr models on triangular and square lattice rod bundles. Of the six modifications, Aoki (1963) and Kays formulation stood out as the highest performing models, while the Weigand et al. (1997) and Cheng and Tak (2006) models were the lowest performing models from the group.

The information presented in the papers discussed above clearly indicates that there remains a need for further development of Reynolds-averaged Navier-Stokes (RANS) turbulence models for simulations of cooling systems involving fluids with low Pr. From the results of the documents discussed above, Kay's variable Pr_T formulation was one of the simplest to implement solutions to addressing the issues associated with low-Pr flow, and was consistently demonstrated to be more accurate than other models that have been previously tested.

METHODOLOGY

NEK5000

Simulations were run using the spectral solver Nek5000, an open source computational fluid dynamics (CFD) code developed by Argonne National Laboratory based on the spectral element code Nekton 2.0. (Fischer et al., 1988) Nek5000 is a time stepping solver capable of simulating two and three-dimensional, unsteady, incompressible flow on quadrilateral or hexilateral domains, or to simulate axisymmetric fluid flow. Nek5000 uses a spatial discretization based on the spectral element method introduced by Patera (1984).

Spectral simulation offers increased accuracy over traditional finite-volume solvers by using basis functions, much like Fourier series. Since spectral codes use basis functions over the entire domain, as opposed to only locally, as in finite element methods, they offer advantages such as better error properties and exponential convergence. As a result of using basis functions globally, spectral solvers are limited to smooth flows, e.g. no shock waves. The spectral method used by Nek5000 is a Galerkin, or weighted residual method, and uses Gauss-Legendre quadrature to achieve spectral accuracy when discretizing in space.

Nek5000 has been, in the past, limited to DNS and LES simulations. This project sought to take advantage of the spectral accuracy of the software while implementing RANS models, specifically a k-ε model and realizable k-ε model both with and without turbulent Pr modification. The Nek5000 core code was modified to allow linearization of the source terms for additional scalar equations for turbulence model variables, and the rest of the RANS model was simply implemented as subroutine modules in the test case files, specifically the .usr file, of Nek5000. All remaining input files were identical to those used in standard Nek5000 simulations.

It would be helpful to provide some technical information that will help clarify simulation set up later in the document. Nek5000 has a geometry with cells just like a standard finite element code, however, since it is a spectral code, it breaks down a cell into other discretization points for the Gauss-Legendre polynomials. The numbers of points are defined by, lx1, ly1, and lz1, in each respective direction. All directions have the same number of points for simulations run in this study, or lx1=ly1=lz1. In discussion of the grid size, the size of the grid is calculated by the number of elements multiplied by lx1^3, since lx1=ly1=lz1, or the volume of discretized points within each element. Also, an important point to make is the kind of time stepper used in each simulation. For all cases other than the rod bundle cases, simulations were run with bdf2 time stepper, this means, in time, a two-point backward difference formula is used to step forward. In the rod bundle cases, instabilities occurred with using two points for the backward difference as the differences were small in some areas causing error in the next value. Therefore, bdf1 was used as the time stepper for these cases, which uses a single point backward difference.

Governing Equations

The governing equations for constant property channel flow are as follows:

$$\frac{\partial U_i}{\partial x_j} = 0 \tag{1}$$

$$\frac{\partial U_i}{\partial t} + U_j \frac{\partial U_i}{\partial x_j} = -\frac{1}{\rho} \frac{\partial p}{\partial x_i} + v \frac{\partial^2 U_i}{\partial x_j \partial x_j} - \frac{\partial \tau_{ij}}{\partial x_j} + f_i + g_i \beta \Delta T \tag{2}$$

$$\frac{\partial T}{\partial t} + U_j \frac{\partial T}{\partial x_j} = k_T \frac{\partial^2 T}{\partial x_j \partial x_j} - \frac{\partial q_j}{\partial x_j} \tag{3}$$

Here U_i is the mean velocity field, ρ is the density, p is the pressure, v is the kinematic viscosity, f_i is a forcing term defined by the user to drive flow, g is the gravitational acceleration vector, β is the coefficient of thermal expansion, ΔT is the difference between the user defined reference temperature used to implement the Boussinesq hypothesis for buoyancy considerations,

T is the temperature, and k_T is the thermal diffusivity. τ_{ij} and q_i, are the unknown components of the turbulent stress tensor and the turbulent heat flux, respectively. For RANS models these values are the Reynolds stress and flux terms, which are modeled using an eddy-viscosity approach. This approach is further discussed in the modeling section.

Turbulence Models

This section provides a brief description and relevant equations for the RANS models used in this study. The models chosen for this study are the standard k-ε model and a realizable form of the k-ε model. These RANS models offer significant reduction in complexity and computational cost when compared to DNS or LES. Direct numerical simulation (DNS) seeks to numerically solve the Navier-Stokes equations for all scales of turbulence down to the smallest, Kolmogorov microscales. This is extremely expensive, but because every scale is resolved it is also highly accurate. LES, or Large Eddy Simulation, compromises accuracy versus DNS for simplifying computations. LES assigns weight to certain sized length scales giving more computational attention to the larger more influential fluctuations and filtering out the small fluctuations since they are the most expensive to resolve, and thus producing a resulting model that is cheaper, computationally, than DNS.

k-ε

The most common two equation model, originally developed by Jones and Launder (1972), is the k-ε model. The standard k-ε model implements two additional transport equations, one corresponding to turbulence kinetic energy (k), and the other corresponding to turbulence dissipation rate (ε). The standard model is only valid outside of the near wall region where the flow is not dominated by viscous effects, however, by using a version of the model that blends a

one-equation model (Wolfshtein, 1969) for the near-wall region and the standard model outside of the near-wall region avoids this problem. This is done specifically by using a wall-limiting value for the dissipation rate. The model equations are as follows:

$$\frac{\partial k}{\partial t} + \underbrace{U_j \frac{\partial k}{\partial x_j}}_{Convection} = \underbrace{P}_{Production} - \underbrace{\varepsilon_{eff}}_{Dissipation} + \underbrace{\frac{\partial}{\partial x_j}\left[\left(\frac{\nu_T}{\sigma_k} + \nu\right)\frac{\partial k}{\partial x_j}\right]}_{Diffusion} + G_b \qquad 4$$

$$\frac{\partial \varepsilon}{\partial t} + \underbrace{U_j \frac{\partial \varepsilon}{\partial x_j}}_{Convection} = \underbrace{C_{1\varepsilon}\frac{\varepsilon^*}{k}P}_{Production} - \underbrace{C_{2\varepsilon}\frac{\varepsilon}{k}\varepsilon_{eff}}_{Destruction} + \underbrace{\frac{\partial}{\partial x_j}\left[\left(\frac{\nu_T}{\sigma_\varepsilon} + \nu\right)\frac{\partial \varepsilon}{\partial x_j}\right]}_{Diffusion} + C_{3\varepsilon}\frac{\varepsilon}{k}G_b \qquad 5$$

where:

$$\varepsilon_{eff} = \frac{\varepsilon^*}{\left[1 - \exp\left(-\frac{Re_y}{A_\varepsilon}\right)\right]} \qquad 6$$

$$\varepsilon^* = \max\left(\varepsilon, \frac{k^{\frac{3}{2}}}{c_W d}\right) \qquad 7$$

$$Re_y = \frac{\sqrt{k}d}{\nu} \qquad 8$$

In Eq. 7 "d" represents the distance to the nearest wall. The turbulent stresses for RANS are:

$$\tau_{ij} = \frac{2}{3}k\delta_{ij} - 2\nu_T S_{ij} \qquad 9$$

$$\nu_T = C_\mu \frac{k^2}{\varepsilon^*}\left[1 - \exp\left(-\frac{Re_y}{A_\mu}\right)\right] \qquad 10$$

$$S_{ij} = \frac{1}{2}\left(\frac{\partial u_j}{\partial x_i} + \frac{\partial u_i}{\partial x_j}\right) \qquad 11$$

This ν_T in Eq. 10 is referred to as the eddy-viscosity, as previously mentioned with the governing equations. The turbulent heat flux is then calculated based on the turbulent Prandtl number,

$$q_i = \nu_\theta \frac{\partial \theta}{\partial x_i} \qquad 12$$

$$v_\theta = \frac{v_T}{Pr_T} \tag{13}$$

$$Pr_T = 0.85 \tag{14}$$

As indicated in Eq. (14), the turbulent Prandtl number, Pr_T, is typically assumed to be a constant value for Pr~1 fluids such as air with the standard value taken to be 0.85. This study will investigate the use of both the standard value and an alternative formulation for variable Pr_T (Kays, 1994).

Turbulence due to buoyancy is accounted for in both the k and ε equations through the buoyancy production term G_b.

$$G_b = \beta \frac{v_T}{Pr_T} g_i \frac{\partial T}{\partial x_i} \tag{15}$$

$$C_{3\varepsilon} = \tanh\left(\frac{v}{u}\right) \tag{16}$$

The remaining model constants not indicated here are specified according to Launder and Spalding (1974) and Wolfshtein (1969): $\sigma_k = 1$, $\sigma = 1.3$, $C_1 = 1.44$, $C_2 = 1.92$, $C_W = 2.495$, $A_\varepsilon = 4.99$, $A_\mu = 70$, $C_\mu = 0.09$.

Realizable k-ε

The realizable model used in this study is a modification to the standard k-ε model discussed previously. This two-equation model differs slightly both in the formulation of turbulent viscosity, and by changing a model constant. Instead of using a constant value for C_μ, the realizable method makes this value variable. It is computed from:

$$C_\mu^* = \frac{1}{(4.04 + 2.12 * max(ske, 3.33))} \tag{17}$$

where

$$ske = Sk/\varepsilon \tag{18}$$

$$S = \sqrt{2S_{ij}S_{ij}}$$

<div align="right">19</div>

The implementation of the variable C_μ is what maintains realizability or maintains physically realistic values for the turbulent stress. In other words, without the modification, the normal stress term can become negative and/or the shear stress term can violate the Cauchy-Schwarz inequality. If S becomes large relative to $\frac{k}{\varepsilon}$, then ν_T may become small leading to the violation of realizability. The additional change is to the constant $A_\mu=30$.

Kay's formulation

Kays formulation is a relatively straightforward modification, (Kays , 1994), that can be implemented to help predict flows where the Pr is low relative to air. This method does not assume that turbulent Pr is constant as is done for the Reynolds analogy, rather a function of the turbulent viscosity, the molecular Pr, and the kinematic viscosity of the fluid. This function is defined as:

$$Pr_T = 0.85 + \frac{0.7}{\frac{\nu_T}{\nu}Pr}$$

<div align="right">20</div>

From which turbulent heat flux is calculated:

$$\tau_{\theta,i} = \nu_\theta \frac{\partial \theta}{\partial x_i}; \; \nu_\theta = \frac{\nu_T}{Pr_T}$$

<div align="right">21</div>

The implementation of Kay's formulation should in theory increase accuracy in current models because it reduces the turbulent thermal diffusivity relative to the turbulent viscosity in areas of low-Pr. Previous studies have shown that Kay's formulation can potentially improve predictive capability for RANS modeling of low-Pr flows.

Test Cases

For completeness, in validation, it is important to evaluate turbulence models for various flow geometries, boundary conditions, and flow characteristics. To evaluate the various models for solving low Pr fluid flow, a progression of test cases was followed. Simulations were run for pressure driven plane channel flow cases with constant, equivalent wall boundary temperatures for a range of flow speeds at different values of molecular Pr. Asymmetric wall temperature boundary conditions were next evaluated, including buoyancy effects. These cases were evaluated in order to examine the validity of the models before graduating to more complex geometries. Simulations were also run for backward facing step geometries, with and without buoyancy effects, and finally a simplified square-lattice rod bundle geometry was tested. The final test case represents a flow configuration commonly found in actual nuclear reactor cooling systems.

Channel Cases

One fundamental benchmark of a turbulence model is the accurate prediction of pressure driven turbulent flow in a plane channel. These cases were selected to investigate different values of Pr at each selected Reynolds number, corresponding to available comparison data, specified in table 1 below. Cases are characterized solely by the values of Re and Pr for cases without buoyancy. For cases with buoyancy effects, cases were further characterized by the value of the Grashof number (Gr). The channel cases vary in their boundary conditions and flow characteristics however the geometry of the channel remained constant for all cases; this geometry is shown in Figure 1.
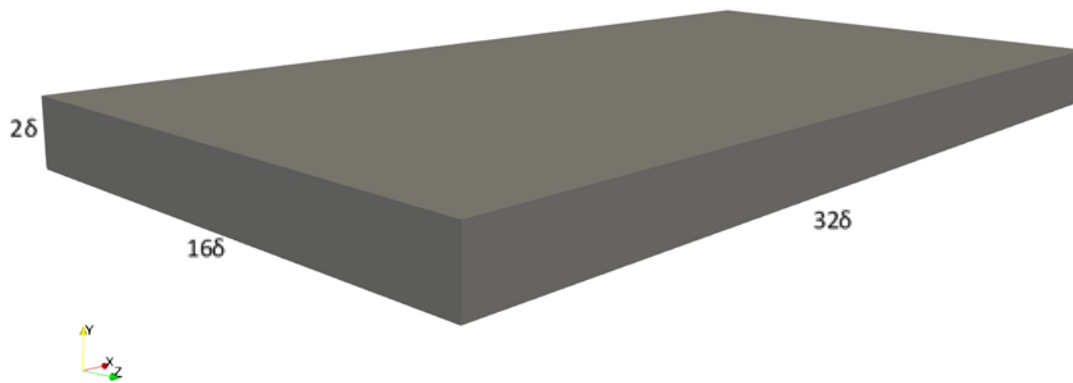
Figure 1: Geometry for all channel flow cases

Due to the nature of RANS models, a cubic grid is not required for good results, unlike DNS and LES. Elements with high aspect ratios, or skewed cells, with large proportions of height, length, and width, can be used. To verify that the models implemented reflect this property of RANS models, the geometry was created with high aspect ratio cells as opposed to more cubic (i.e. aspect ratio equal to one) elements.

Table 1 shows all plane channel cases that were simulated and their respective parameters. It is important to note that several of the indicated parameters are used in Nek5000 and do not define the case.

Table 1: Channel case identification

Case Identification						Simulation parameters		
Case ID	Re_τ	Pr	Gr	Orientation	Wall Temp BCs	Grid points (# elements*lx1^3)	time Stepper	Run Time (s)
1	150	0.7	0	NA	Equal	131,072	bdf2	50
2	150	0.025	0	NA	Equal	131,072	bdf2	50
3	180	0.71	0	NA	Equal	131,072	bdf2	50
4	180	0.2	0	NA	Equal	131,072	bdf2	50
5	180	0.025	0	NA	Equal	131,072	bdf2	50
6	395	0.71	0	NA	Equal	131,072	bdf2	50
7	395	0.025	0	NA	Equal	131,072	bdf2	50
8	640	0.71	0	NA	Equal	131,072	bdf2	50
9	640	0.025	0	NA	Equal	131,072	bdf2	50
10	150	0.7	0	NA	Different	131,072	bdf2	50
11	150	0.7	1.3×10^6	Horizontal (unstable)	Different	131,072	bdf2	400 avg
12	150	0.7	4.4×10^6	Horizontal (stable)	Different	131,072	bdf2	50
13	150	0.7	9.6×10^6	Vertical	Different	131,072	bdf2	1000

In Table 1, equal boundary conditions are defined as constant wall temperature boundaries of 0°C. Different boundary conditions are defined as one hot wall at 40°C and a cool wall at 0°C. All cases have fluid entering the domain at 20°C.

Backward Facing Step Cases

Backward facing step cases were simulated to test model behavior for separated flow, where the flow detaches from the wall then reattaches further in the flow, where eddies and vortices often form in the area of separation. To investigate capability of predicting separated flows, backward facing step test cases were chosen that had available DNS or experimental data to compare against in order to evaluate each model.

Vogel and Eaton (1985) ran the original backward facing step experiments with air, therefore, the non-dimensional quantities important to define the flow were derived based on the

assumption of air at atmospheric pressure and a temperature of 7.5⁰C above ambient, the average

temperature of the air in the flow. Niemann and Frohlich (2016), ran DNS simulations on backward

facing steps with a Pr=0.0088, and all non-dimensional quantities associated with this flow were

matched accordingly.

Geometry was adopted from Niemann and Frohlich (2016) as depicted in Figure 2,
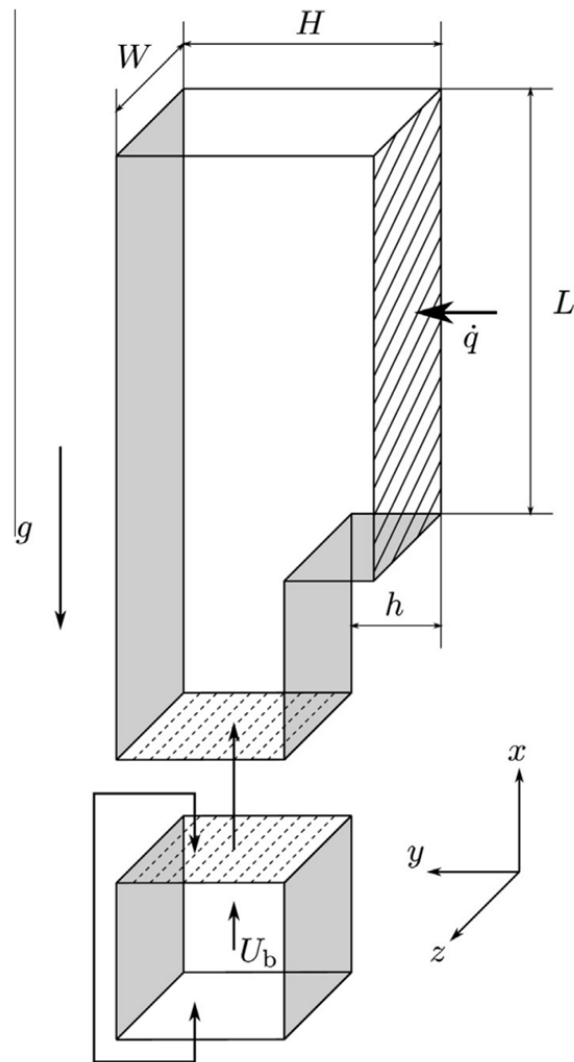
Fig. 1. Sketch of the vertical backward-facing step configuration investigated (not to scale). The bottom block represents the generator for turbulent inflow data.

Figure 2: Backward facing step geometry Niemann and Frohlich (2016)

The step height in the original Vogel and Eaton experiment was given to be a physical length in the published document, however, for convenience, all step heights were set to unity and the rest of the geometry was scaled appropriately. It is important to note that the channel expansion ratio, the difference in height of the inlet channel and the main flow channel, or the ratio of H to h is different for the Vogel and Eaton case as opposed to the Niemann and Frohlich cases. The expansion ratio for Vogel and Eaton is 1.25 and the ratio for Niemann and Frohlich is 1.5, otherwise all physical parameters are based on a unit step height.

An inlet flow velocity profile was not available for any of the cases. A 1/7 power law profile was assumed for the Vogel and Eaton case based on the centerline velocity at the entrance indicated in the paper. Niemann and Frohlich discuss that the entrance channel was fully developed, thus a fully developed channel flow profile was used as the inlet condition for both Niemann and Frohlich cases. Additional simulation information is provided in table 2.

Table 2: Backward facing step case identification

Case Identification						Simulation parameters		
Case ID	Reynolds No.	Pr	Experiment or DNS	Wall Temp BC	Buoyant	Grid Points (Elements *lx1^3)	time Stepper	Run Time (s)
VE	Re_H = 28000	0.7	Experiment	Const heat flux	Yes	854,016	bdf2	10
NF	Re_τ = 300	0.0088	DNS	Const heat flux	No	743,424	bdf2	10
NF_B	Re_τ = 300	0.0088	DNS	Const heat flux	Yes	743,424	bdf2	10

Benchmark Rod Bundle Case

The benchmark case examined in this document represents a sample section of a rod bundle present in a typical nuclear reactor. Because this case is more complex than the other test cases

evaluated and much closer to a reactor's physical reality, it more fully reveals the applicability of the models presented in this paper to low Pr fluid flow scenarios in actual practice.

The rod bundle geometry was selected based on Hooper and Wood (1984) and nondimensionalized by setting the diameter of the rod to be unit. The flow field is a section from a square lattice rod bundle, two rods by three rods in size and one rod diameter in the flow direction as depicted below in Figure 3:
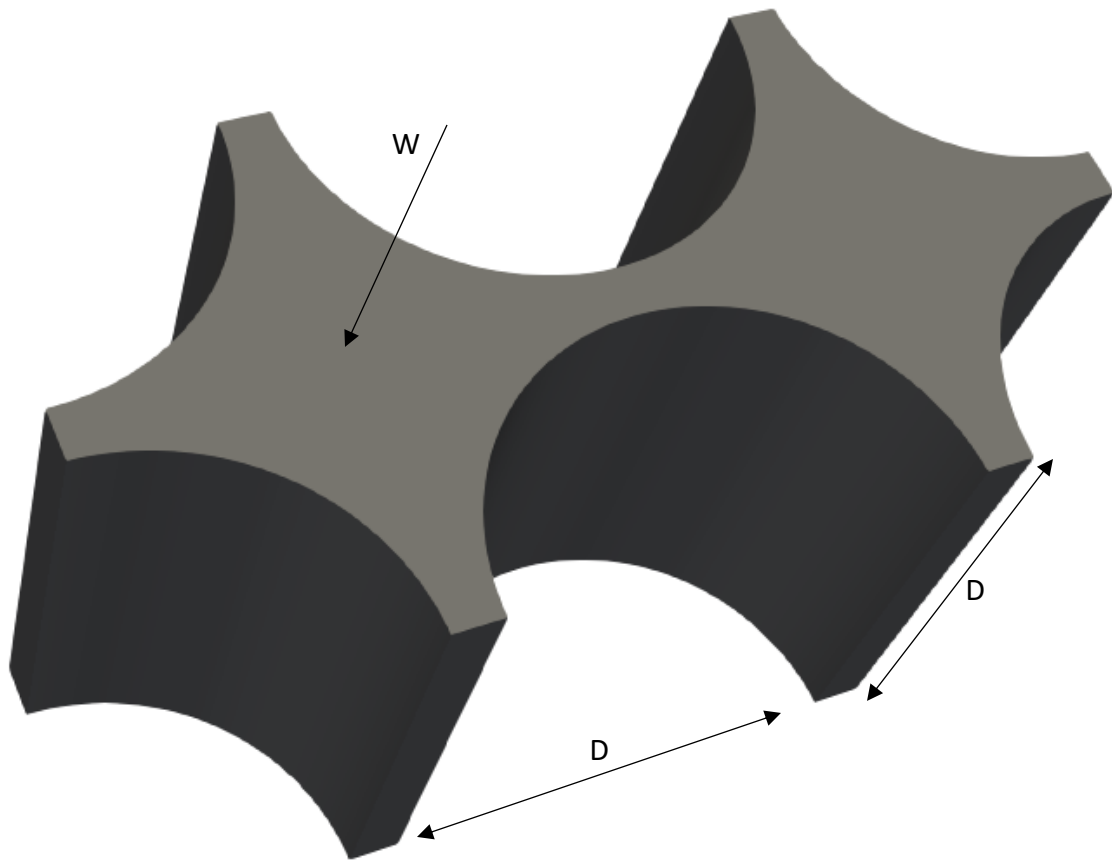

Figure 3: Geometry for the benchmark rod bundle case

Data was plotted for values of θ=0, 30, and 45 degrees as represented in Figure 46. Values were plotted with respect to the variable r, the distance measured from the nearest rod surface, along the lines defined by θ. Data was nondimensionalized using the maximum distance from the

wall (r_{max}) on the respective line θ. Variables r and θ are depicted in Figure 4 from Hooper and Wood (1984).
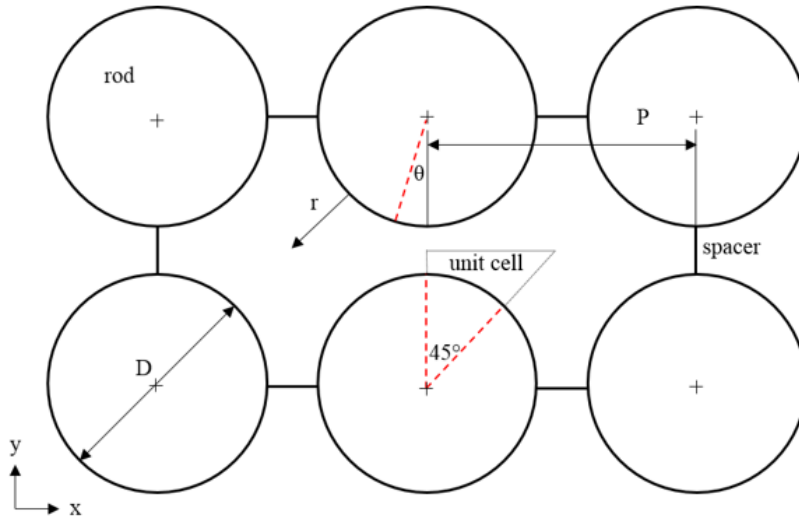

Figure 1: Schematic of geometry, where all lines at θ are measured from the gap center (origin) and goes normal from the rod.

Figure 4: Cross section of rod bundle geometry with helpful coordinate information from Hooper and Wood (1984)

For discussion of boundary conditions and setup for the rod bundle case, it should be noted that the areas between rods but on the boundary of the domain are referred to as "gaps" however there are, in actuality, separators located in the spaces between rods. The simulation was set up with an initial temperature of 100⁰C and bulk volumetric flowrate of 1m/s in the z-direction. Boundary conditions for momentum were all treated as no-slip boundaries. All boundaries were treated as wall conditions for passive scalars, k and ε, where the values are forced to zero at these locations. The thermal boundary conditions are adiabatic for the gaps and flux boundaries for the rod wall itself, where the value of the flux is 0.1 W/m^2 and was held constant for all simulations regardless of Pr. Viscosity was also held constant for all values of Pr, and the thermal conductivity was adjusted accordingly. Additional information involving each rod bundle case is in Table 3.

Table 3: Rod bundle case identification

Case Identification						Simulation parameters		
Case ID	Re	Pr	Viscosity	Conductivity	Wall flux	Grid Points (elements * lx1^3)	time Stepper	Run Time (s)
6	Re_h = 22,600	2	0.00002478 867	0.00001239434	0.1	476,928	bdf1	100
5	Re_h = 22,600	0.71	0.00002478 867	0.0000349136	0.1	476,928	bdf1	100
4	Re_h = 22,600	0.1	0.00002478 867	0.0002478867	0.1	476,928	bdf1	100
3	Re_h = 22,600	0.02	0.00002478 867	0.0001239435	0.1	476,928	bdf1	100
2	Re_h = 22,600	0.01	0.00002478 867	0.002478867	0.1	476,928	bdf1	100
1	Re_h = 22,600	0.002	0.00002478 867	0.01239434	0.1	476,928	bdf1	100

RESULTS AND DISCUSSION

Mesh Independence Study

To evaluate the solution dependence on mesh resolution, coarse and fine grids were implemented for all channel cases. The coarse grid was evaluated with a grid size (number of elements*lx1^3) of 131,072 and a fine grid that had twice the resolution in the direction normal to the wall resulting in 262,144 points. The amount of variation between the two grids was small. The percent differences in both velocity and temperature were plotted between the two different mesh resolutions to evaluate grid independence. For cases with equivalent momentum and thermal boundary conditions the maximum deviation between the simulation results increases with Re, where Re=640 causes the maximum difference between the two grids.
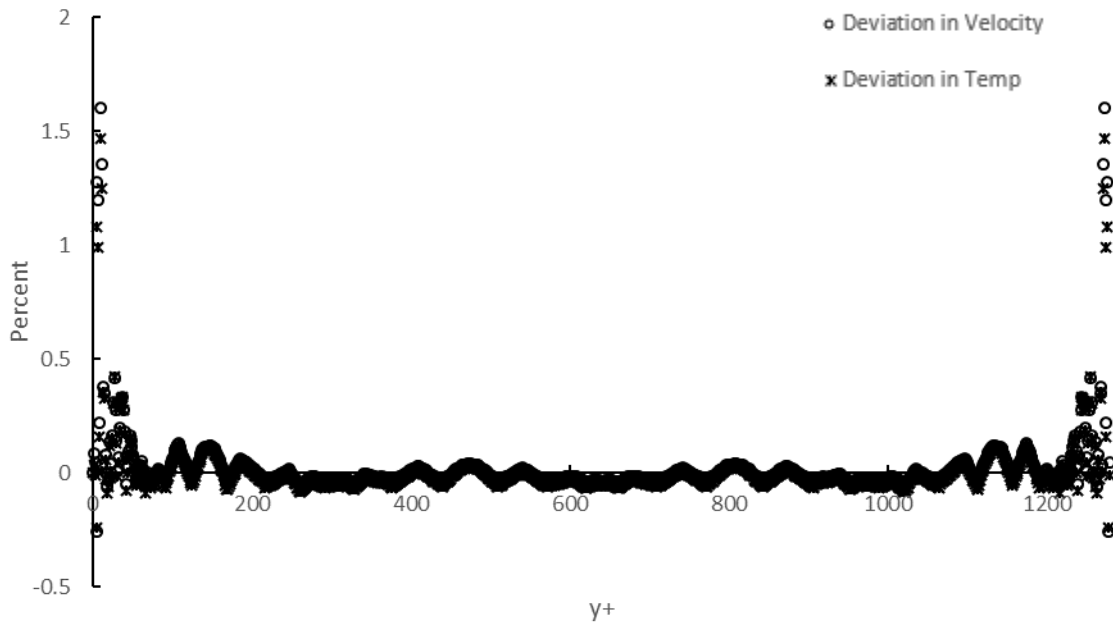
Figure 5: Percent difference between fine and coarse grid channel solutions for velocity and temperature at Re=640

Figure 5 shows the maximum deviation in velocity is about 1.6% and the maximum for temperature is around 1.5%. The amount that the results from the two grids vary for the cases with uneven boundaries is even less than the difference in the Re=640 channel case except for the vertical buoyant case in which the results still varied only slightly.
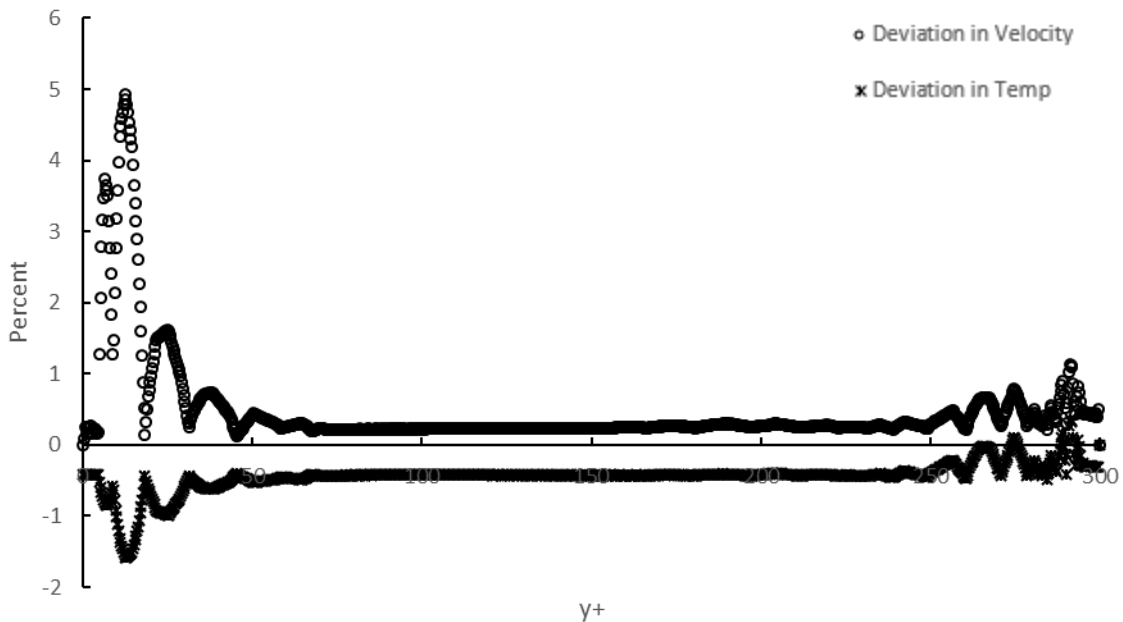
Figure 6: Percent difference between fine and coarse grid channel solutions for vertical, asymmetric thermal boundary channel flow for Re=150

Figure 6 shows that the maximum variation for velocity is about 5% and the maximum for temperature is around 1.5%. The low difference in the two grids weighed against the computational cost associated with the increased number of cells leads to selecting the coarse grid over the fine grid for simulations. One important note is that the grid analysis conducted for the channel cases was considered for the other test cases.

Though the results of the grid study on the channel cases indicate low differences in the solution when the grid resolution is doubled, tests were also run for the rod bundle geometry in order to further validate grid independence.
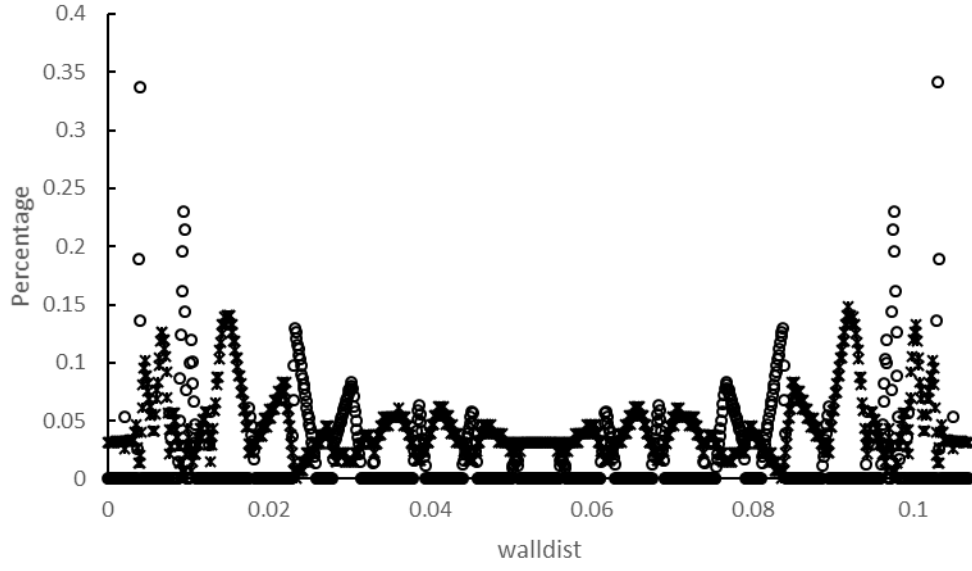
Figure 7: Percent difference between fine and coarse grid rod bundle cases at $\theta=0^{\circ}$ for Pr=0.71
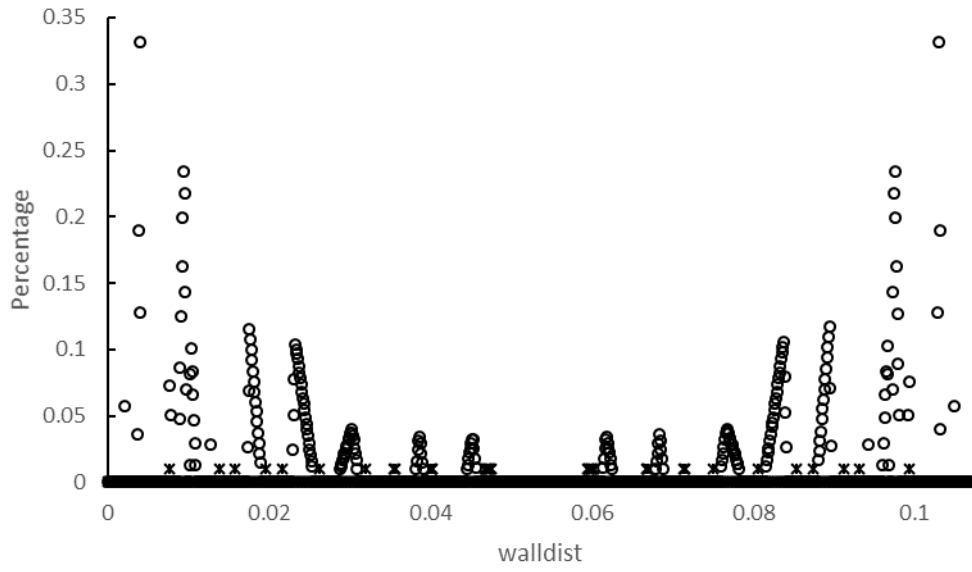

Figure 8: Percent difference between fine and coarse grid rod bundle solutions at $\theta=0^{\circ}$ for Pr=0.002
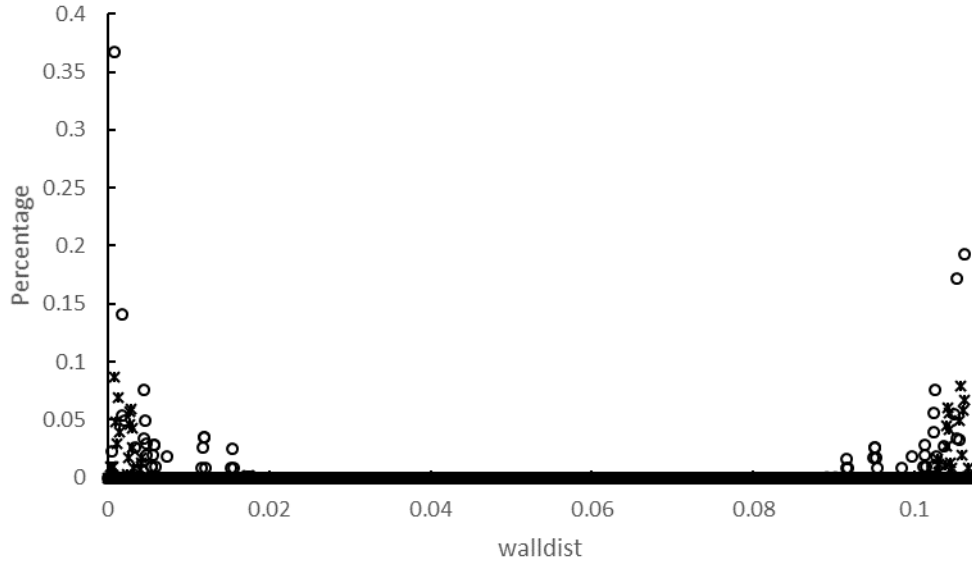
Figure 9: Percent difference between fine and coarse grid rod bundle cases at $\theta=45^{\circ}$ for Pr=0.71
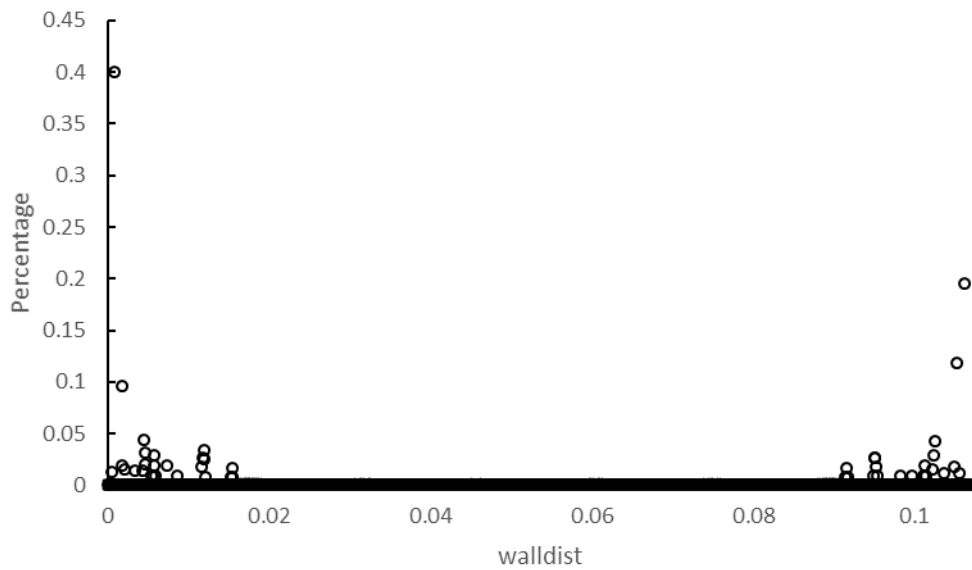

Figure 10: Percent difference between fine and coarse grid rod bundle cases at $\theta=45^{\circ}$ for Pr=0.002

Two grids were generated for the rod bundle, a coarse and refined grid. These grids had 476,928 and 1,492,992 effective elements. Simulations were run both at Pr=0.71 and Pr=0.002.

Figures 7, 8, 9, and 10, show the maximum percent difference between the coarse and fine grid for

θ=0 and θ=45 are 0.35% and 0.4% for velocity respectively, similarly, for temperature, the

maximum deviation was 0.15% and 0.089% respectively.

With less difference in simulation results between grids than the channel cases, and

significant reduction in run time, the lower of the two resolution grids was used for all rod bundle

simulations. This further verifies the independence of the solution from the grid for these models.

Channel Case Results

Channel case plots are mostly presented in this document in U^+ versus y^+ for velocity data

and θ^+ versus y^+ for temperature data. These are values non-dimensionalized by wall shear stress
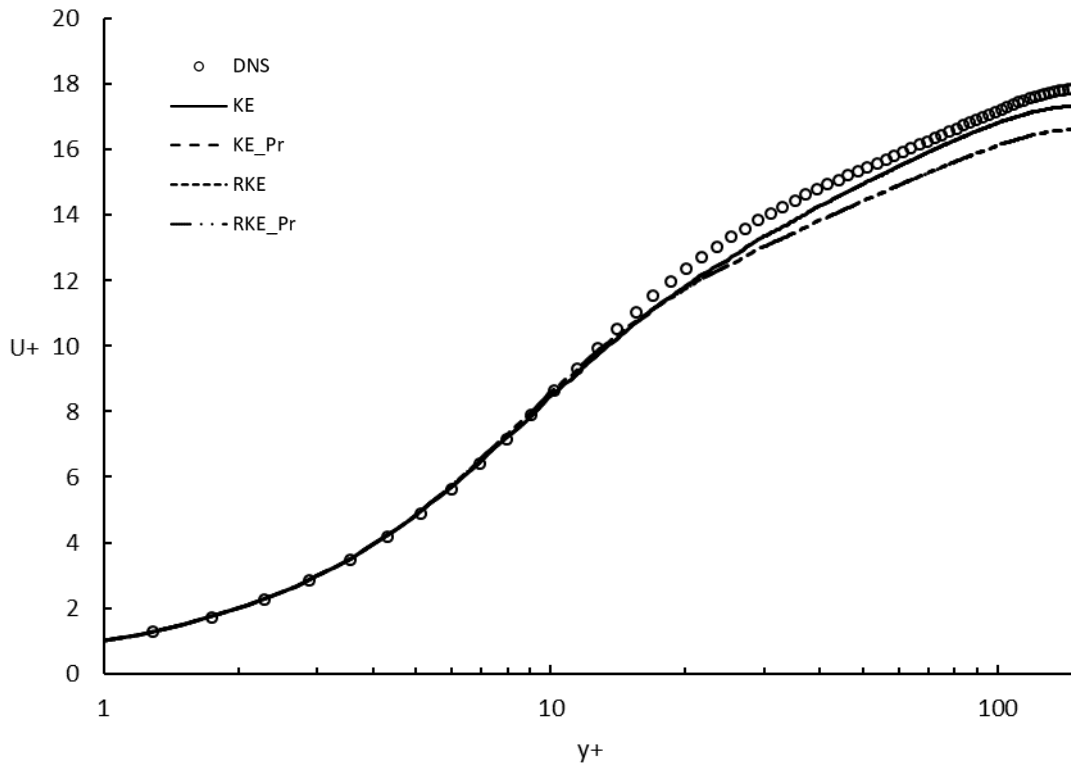
and where θ=T-T$_w$.

Figure 11: Non-dimensional velocity profiles for all models compared to DNS at Re=150

The first channel case results shown in Figure 11 indicate that the models agree closely with the DNS data throughout the channel, however, under-predict midway through the buffer layer. The near wall behavior is consistent across all models, however, there seems to be better prediction for the standard k-ε model. For velocity data, k-ε and its respective Kay's formulation model lie on top of each other on the plot. This is likewise true for the realizable k-ε model. This result is expected since Kay's formulation does not modify any parameters that contribute to the momentum flow field, only the thermal results should vary.
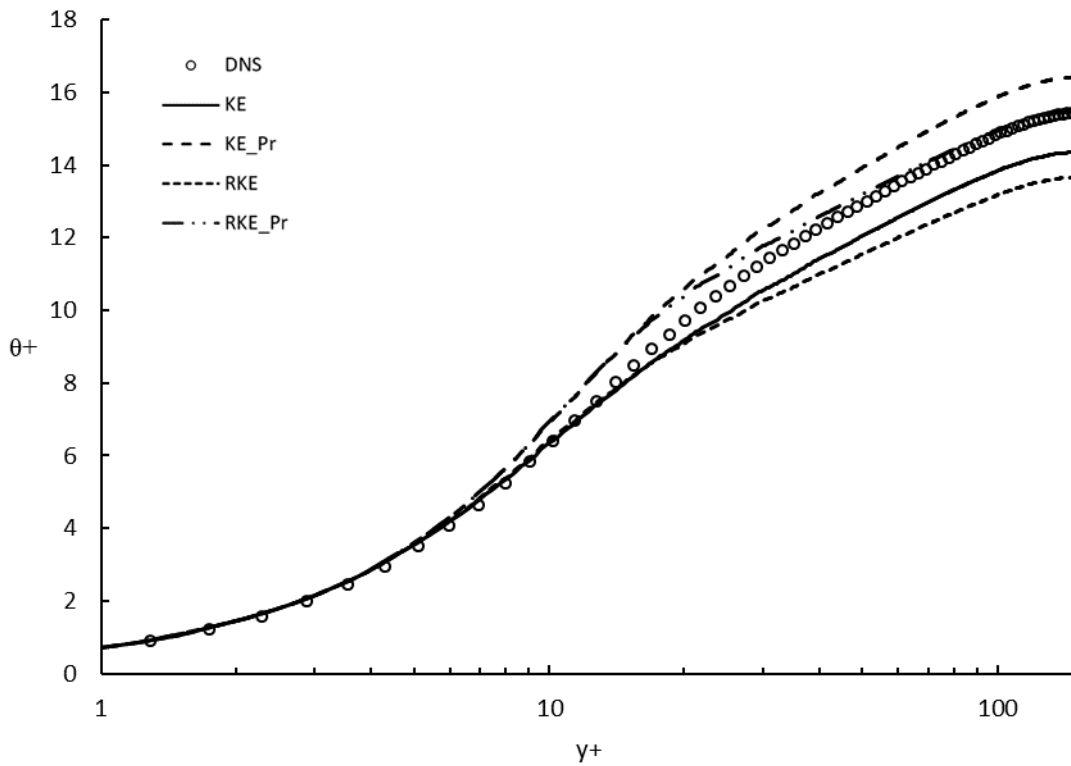

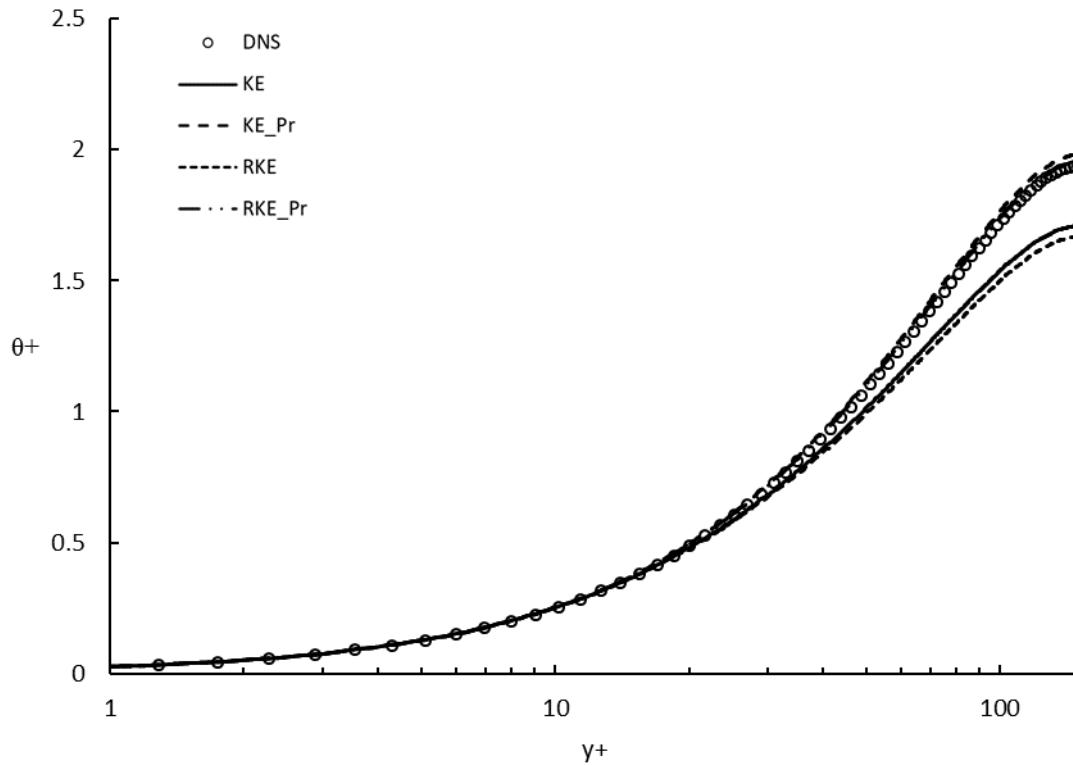Figure 12: Non-dimensional temperature profiles for all models compared to DNS at Re=150 and Pr=0.71

Figure 13: Non-dimensional temperature profiles for all models compared to DNS at Re=150 and Pr=0.025

Figures 12 and 13 show the temperature is much lower in the low Pr case due to the increased thermal diffusivity. The models agree for the air Pr case, though the models with and without the modification to turbulent Pr tend to agree much more closely than the others. Looking at the low Pr case the models with Kay's formulation better predict the flow as opposed to those models without the variable turbulent Pr.
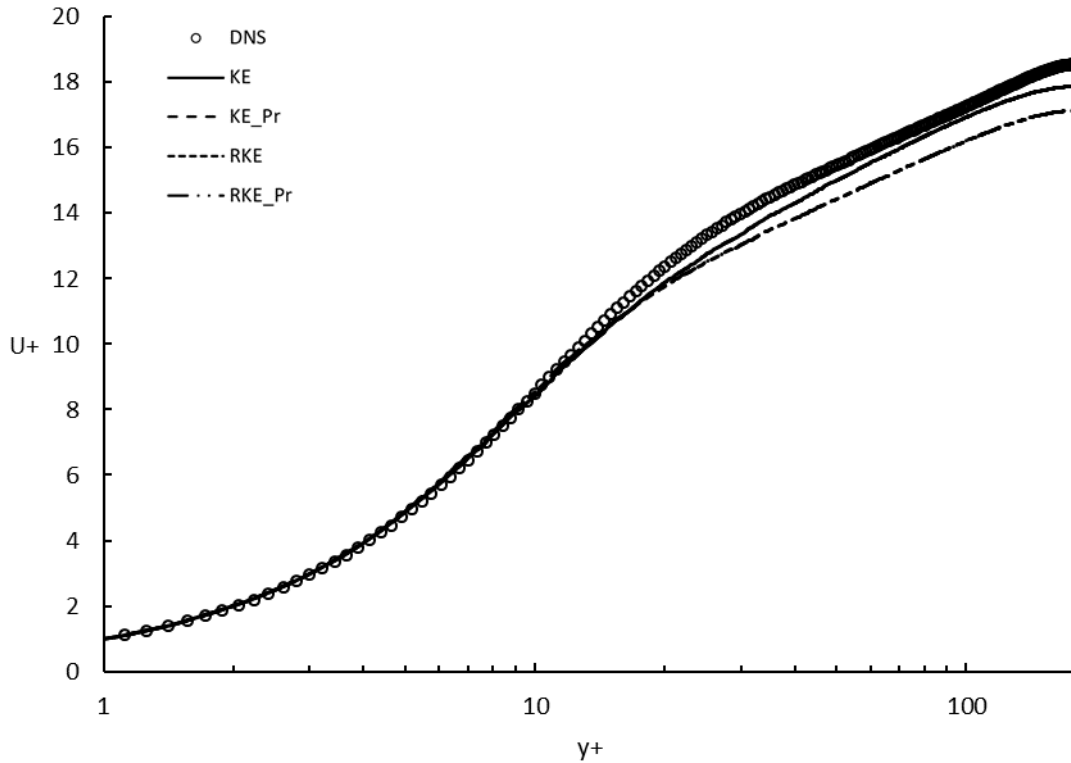
Figure 14: Non-dimensional velocity profiles for all models compared to DNS at Re=180

Again, from Figure 14, one can see that the models with the turbulent Pr modification lie on top of their respective parent model. The results are much the same as with the lower Re case, agreement across all models where the two k-ε models more accurately predict the flow as opposed to the realizable models. However, at this Re, it seems that the models start to under-predict midway through the buffer layer, however, still show reasonable agreement throughout.
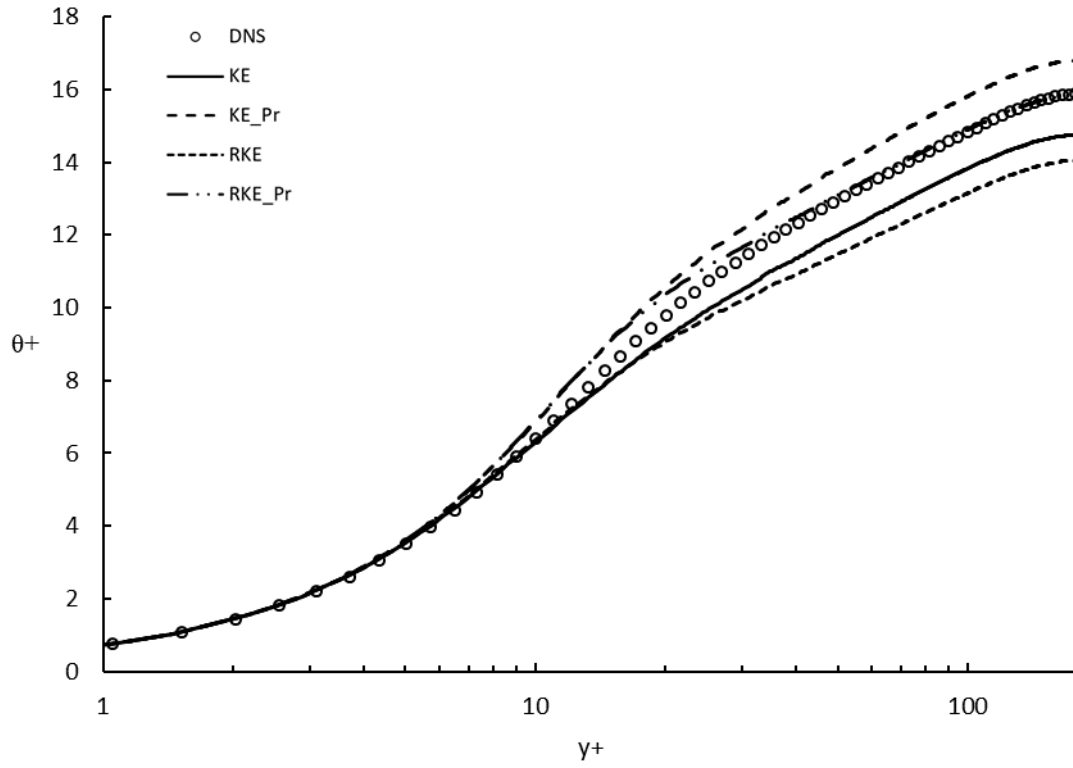
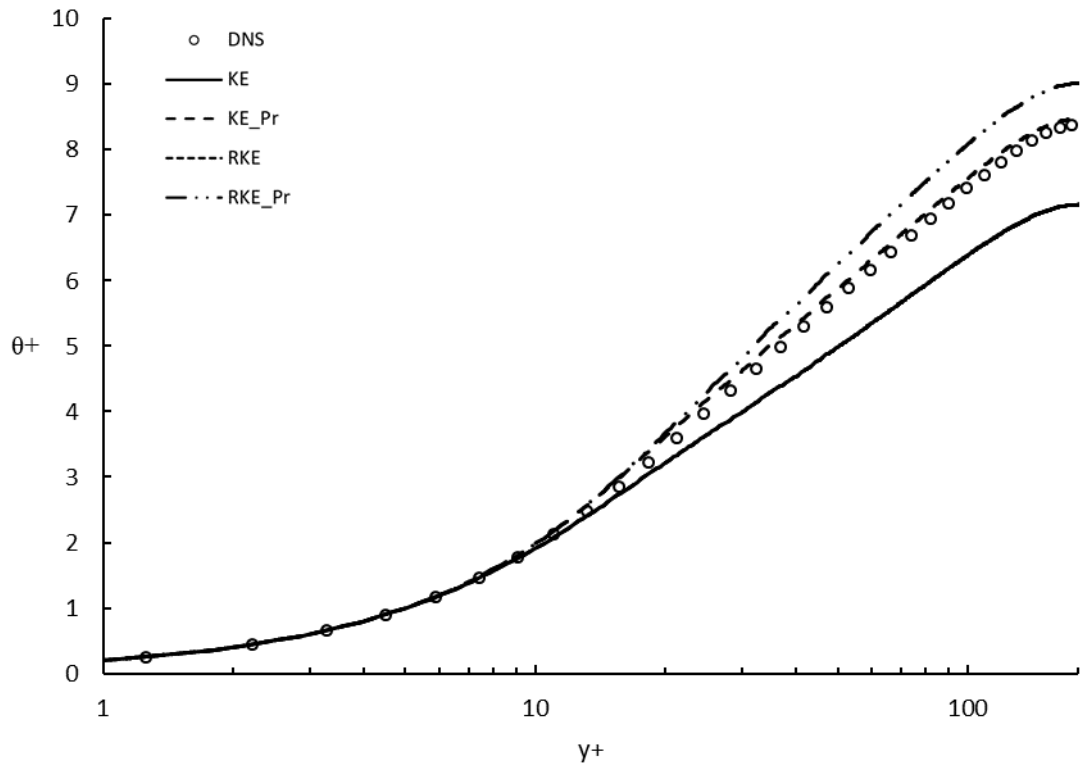Figure 15: Non-dimensional temperature profiles for all models compared to DNS at Re=180 and Pr=0.71

Figure 16: Non-dimensional temperature profiles for all models compared to DNS at Re=180 and Pr=0.2

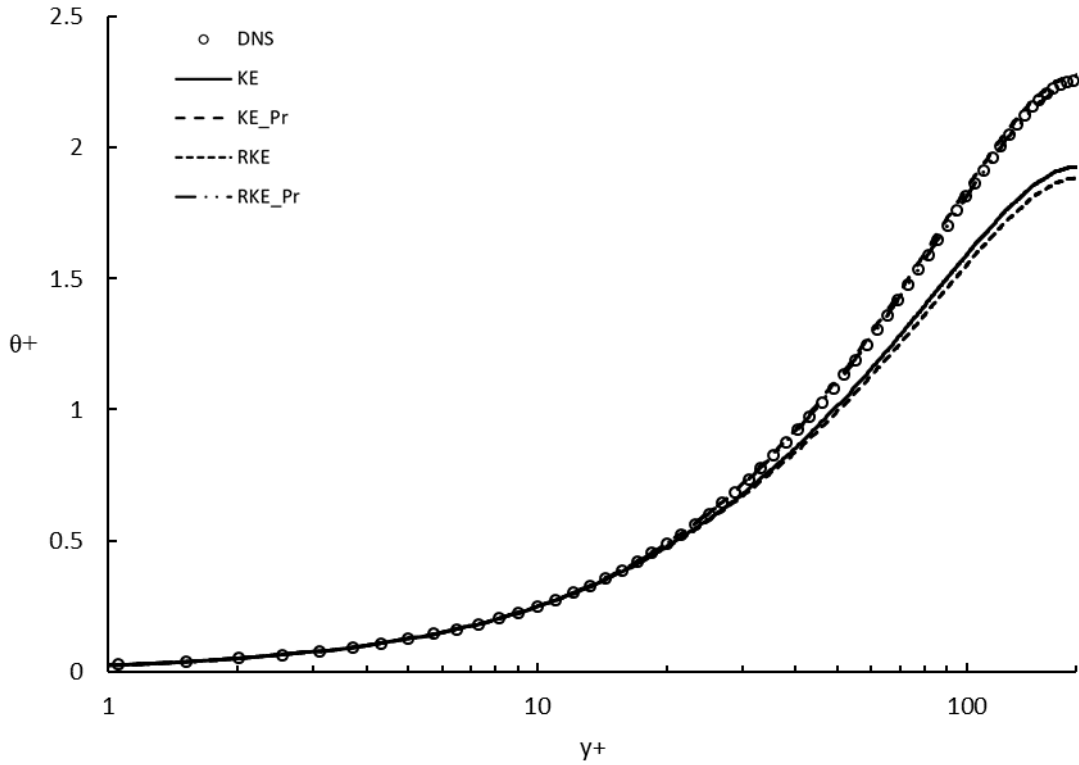Figure 17: Non-dimensional temperature profiles for all models compared to DNS at Re=180 and Pr=0.025

At a Pr similar to air, the behavior of all models is consistent, however as the Pr is lowered the separation between the models with Kay's formulation and those without start to approximate the DNS solution more closely. Note that the k-ε model and realizable k-ε model result in the same curve when Pr=.2.
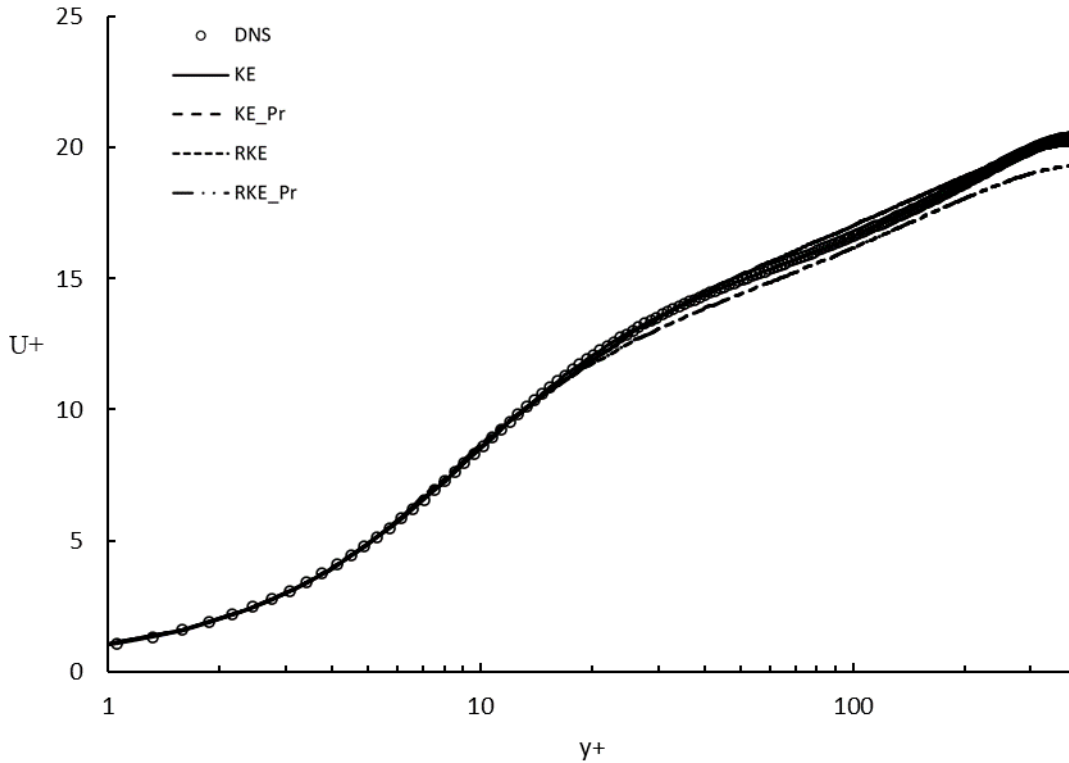
Figure 18: Non-dimensional velocity profiles for all models compared to DNS at Re=395

Velocity trends tend to show that as Re increases, the models better predict the DNS behavior. This is likely due to the fact that the models were originally developed for high-Re boundary layer flow and may not properly respond when applied to flows with relatively low Reynolds number. The velocity data for Re=395 is also unlike the two previous Reynolds numbers in that the two k-ε models, both with and without Kay's modification, start to over-predict the DNS data around y+=50 whereas the two models without Kay's formulation underpredict by around 15% outside the buffer layer.

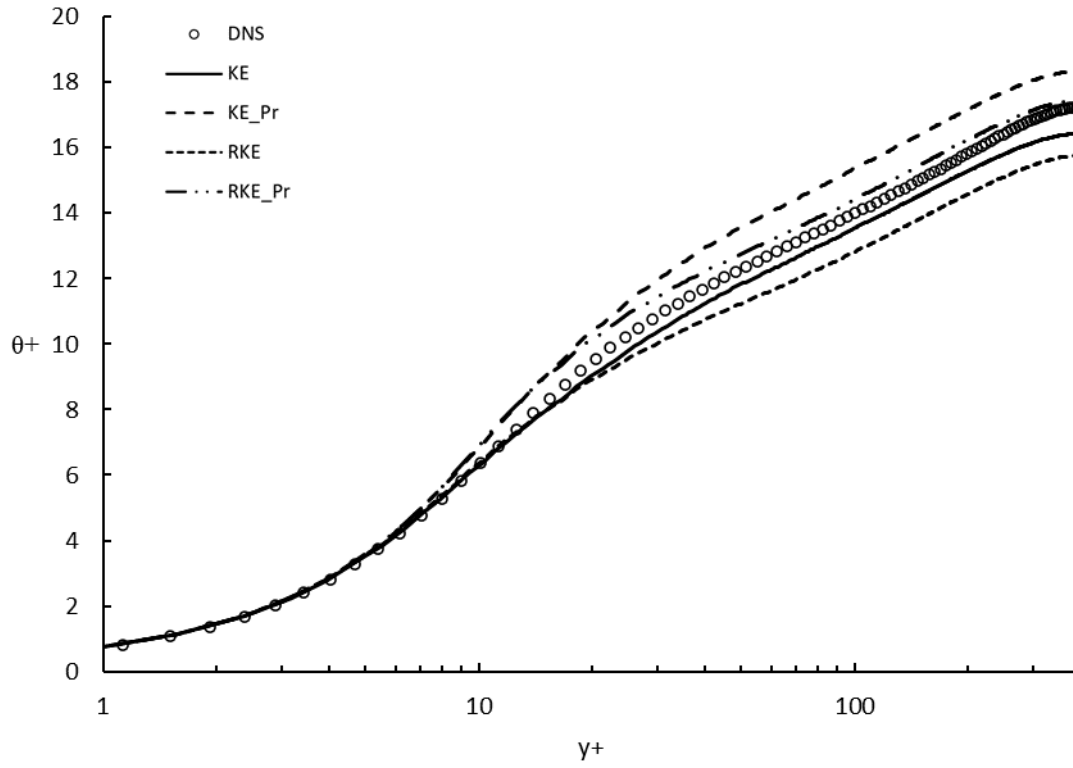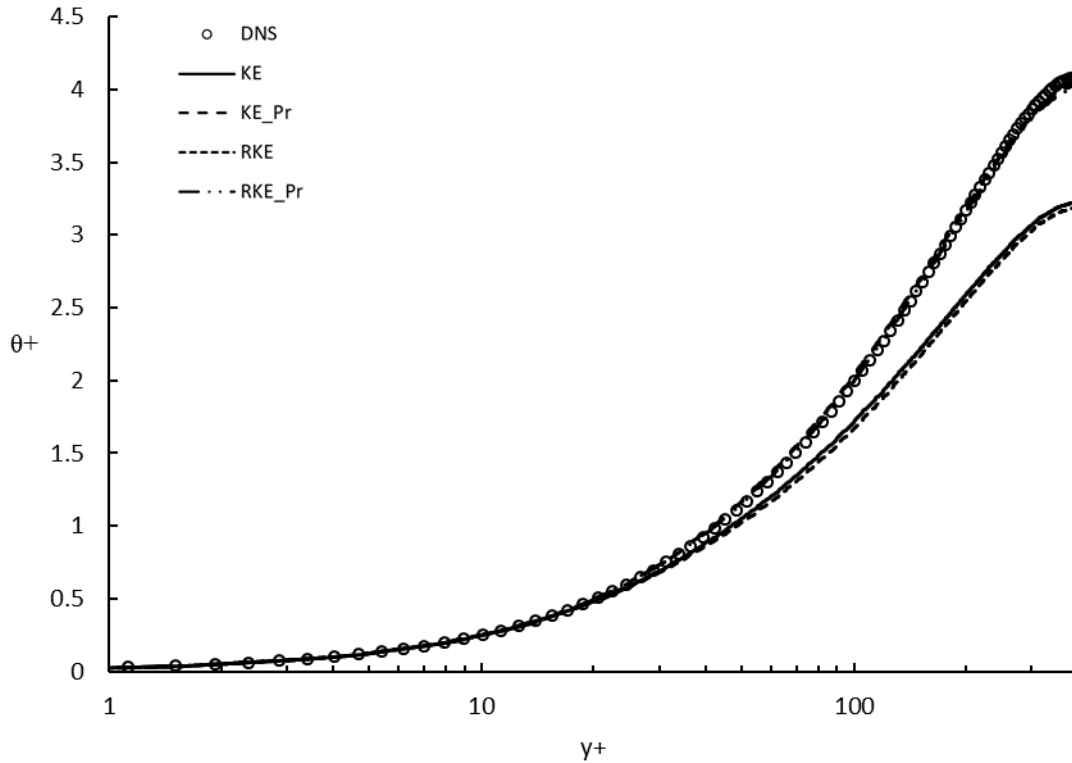Figure 19: Non-dimensional temperature profiles for all models compared to DNS at Re=395 and Pr=0.71

Figure 20: Non-dimensional temperature profiles for all models compared to DNS at Re=395 and Pr=0.025

Figures 19 and 20 show results that echo the previous channel simulations. All models follow the DNS, however the two models with Kay's formulation start to diverge from the DNS outside the viscous sublayer then recover to some extent and predict the trend of the DNS for Pr=.71. Though the models for the air-like Pr do not predict the temperature of the DNS simulation accurately, for the low Pr, the models with Kay's formulation indicate that the implementation of a variable turbulent Pr are better suited to model low Pr fluid thermal behavior. At the very least, the data shows that a RANS model, without any modification, is not able to capture the thermal behavior, given its significant underprediction, around 22%.
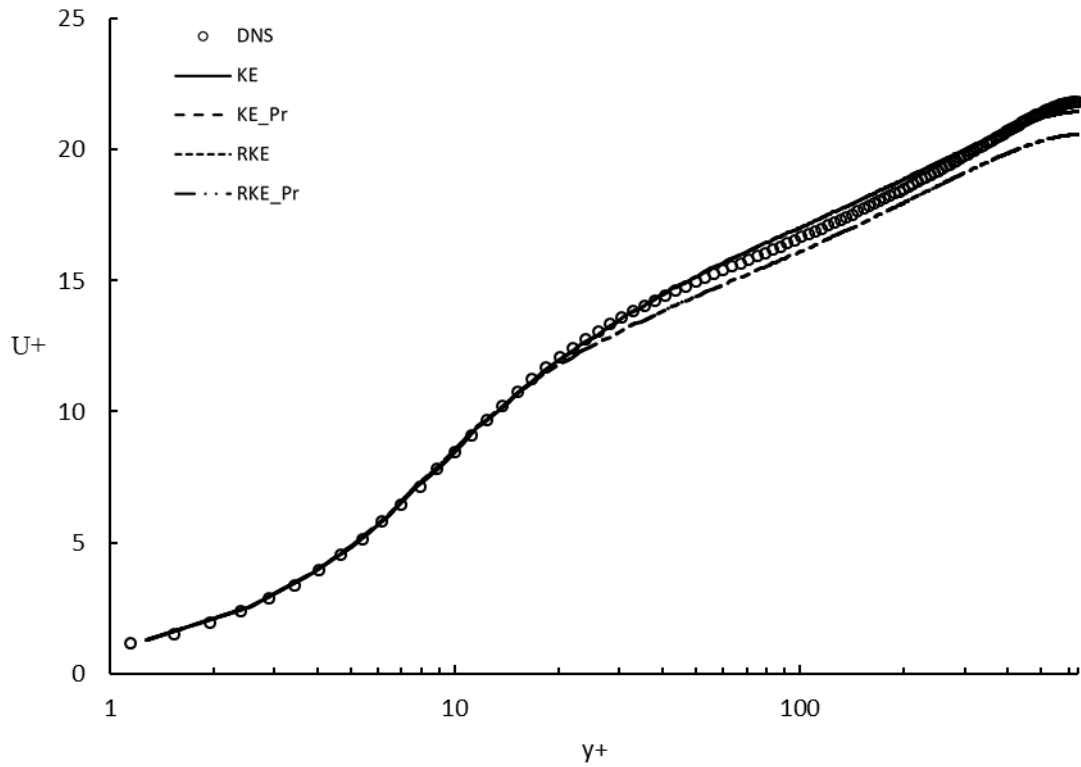
Figure 21: Non-dimensional velocity profiles for all models compared to DNS at Re=640

Figure 21 shows similar results as before. Plots for the standard k-ε model and its Kay's

formulation counterpart lie on top of one another as well as those of the realizable k-ε models.
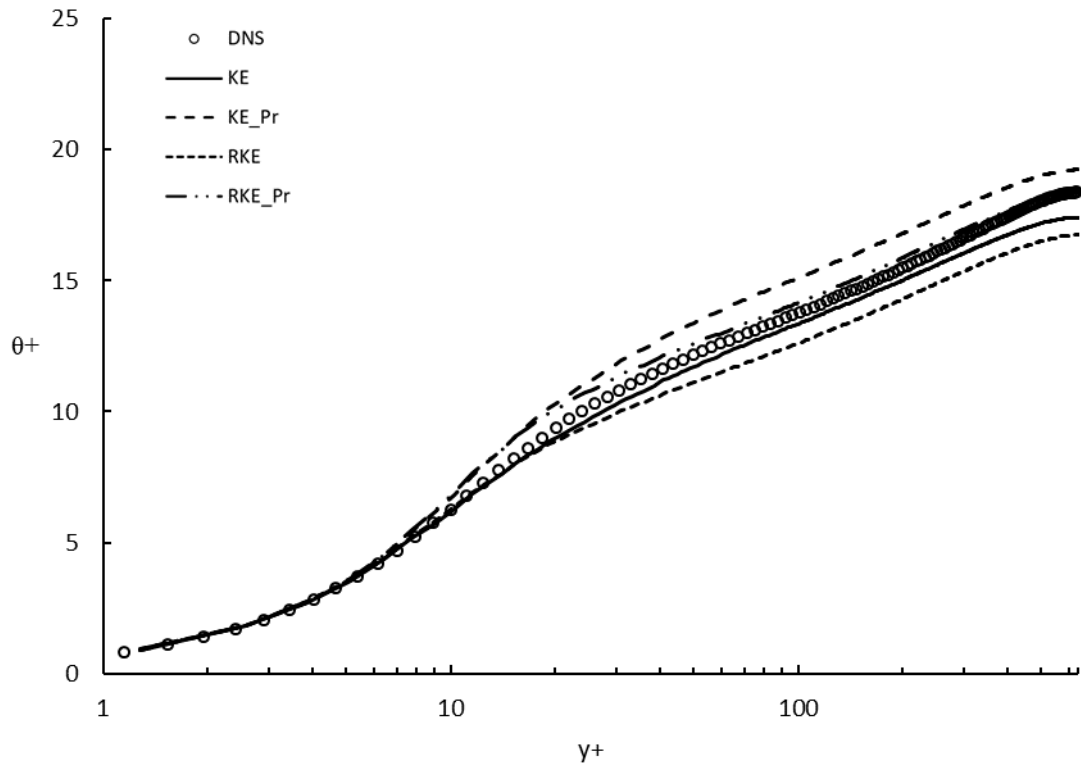
Figure 22: Non-dimensional temperature profiles for all models compared to DNS at Re=640 and Pr=0.71
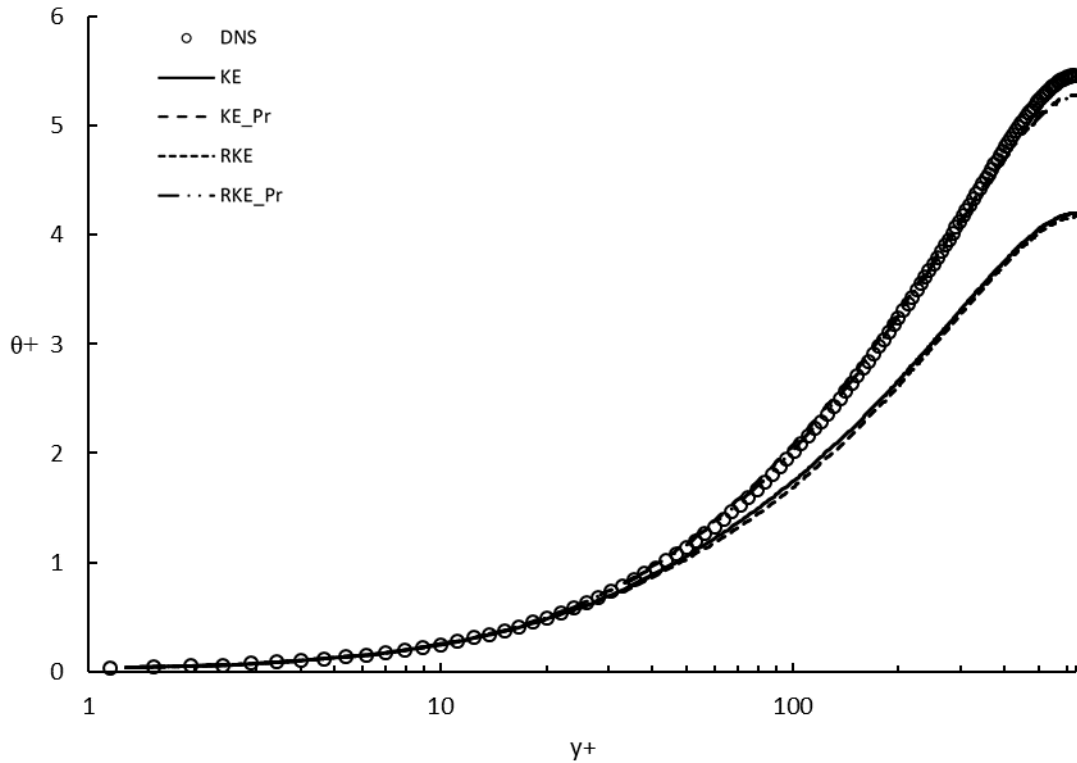
Figure 23: Non-dimensional temperature profiles for all models compared to DNS at Re=640 and Pr=0.025

Temperature plots shown in Figure 22 for the air-like Pr are very similar to that of Re=395. For low Pr the models behave as expected, the models without Kay's formulation start to deviate from the DNS data significantly outside the buffer layer, and the models with Kay's predict the flow very closely until near the centerline of the channel. The under prediction here is expected due to the nature of RANS.

Figure 24: Non-dimensional velocity profiles for all models in a horizontal channel without buoyancy and asymmetric boundary temperatures at Re=150

The velocity data for a horizontal channel case with asymmetric boundary temperatures is shown in Figure 24. Velocity data has no change due to temperature boundaries thus the plots are the same as the Re=150 channel cases shown previously.

Figure 25: Non-dimensional temperature profiles for all models in a horizontal channel without buoyancy and asymmetric boundary temperatures at Re=150, Pr=0.7

The temperature profiles for each model match the behavior of the digitized DNS data reasonably. Interestingly, there is nearly no distinction between any of the models for this case.
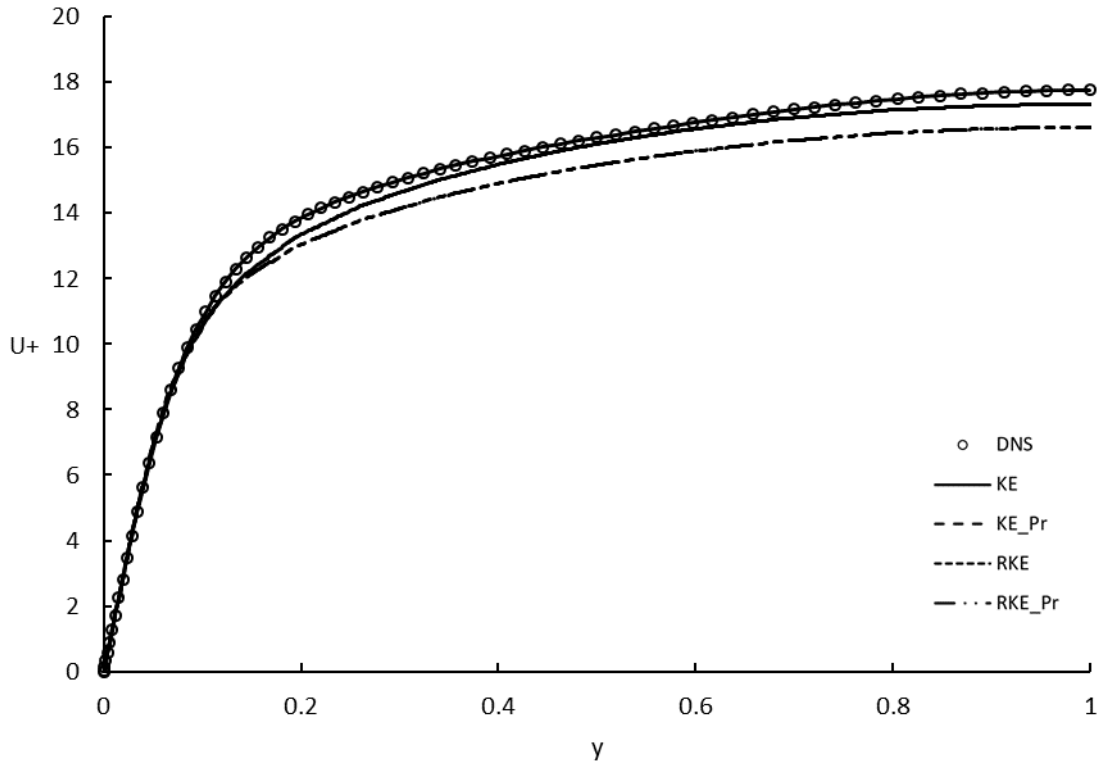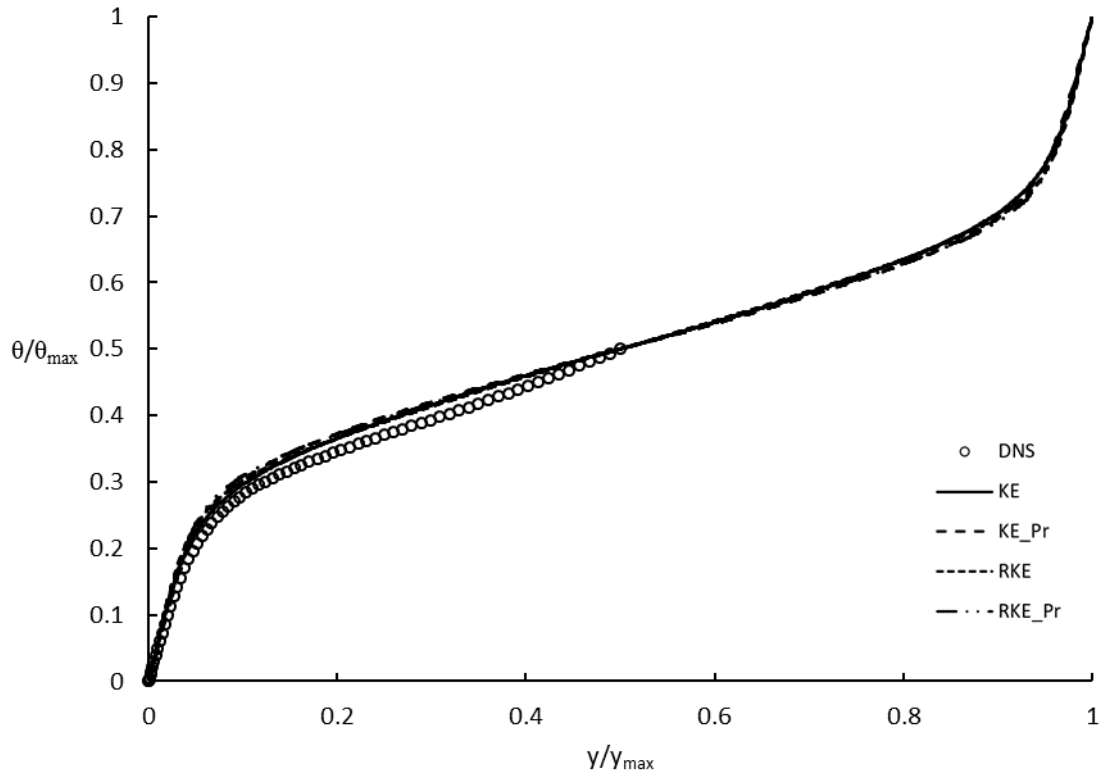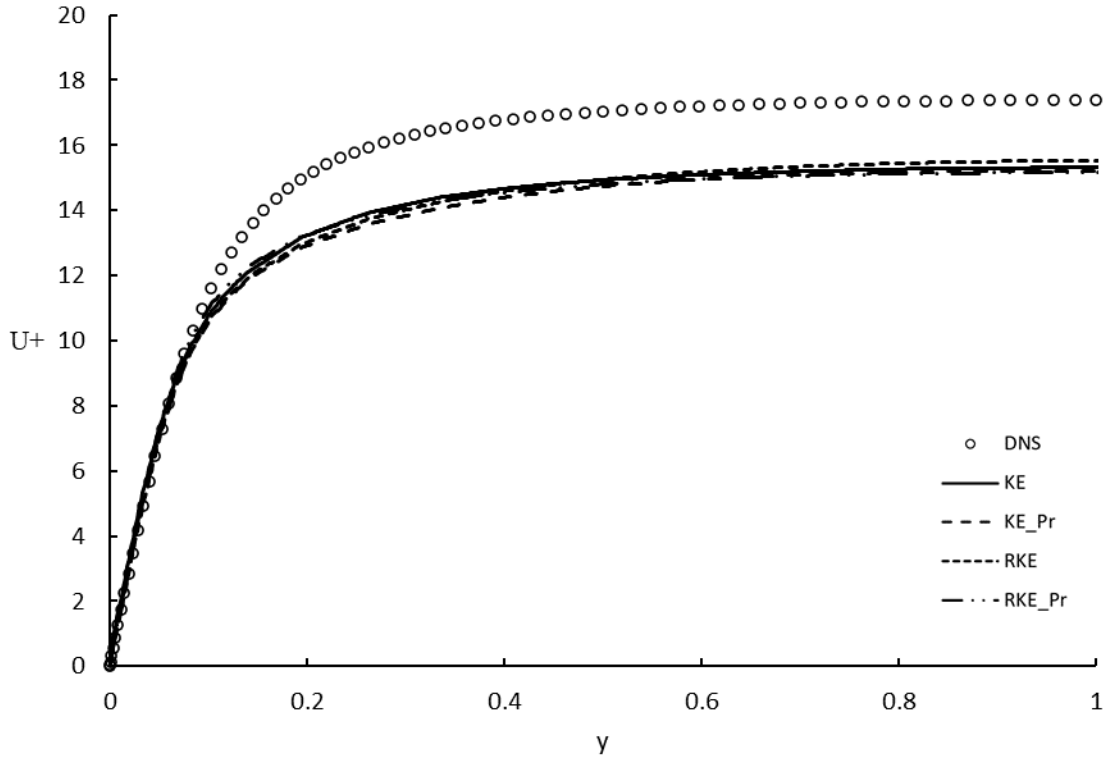
Figure 26: Non-dimensional velocity profiles for all models in an unstable horizontal channel with buoyancy and asymmetric boundary temperatures at Re=150, Gr=1.3e6

For the unstable horizontal channel flow case, pictured in Figure 26, the high temperature boundary is located on the lower wall of the channel. As the fluid on the bottom wall heats, the buoyant force increases causing the fluid to rise in the channel. This rise of fluid along with the horizontal bulk movement of the flow encourages turbulent mixing within the channel. Simulation results indicate that the flow is not stable. Due to the instability, flow results were averaged for 28 data outputs between 16,000-time steps and 160,000-time steps. In the near wall region, all models behave identically while also predicting the DNS data accurately. Outside the near wall region however, the models remain consistent with each other, but do not closely agree with the DNS, underpredicting the momentum field by around 12.5%. This suggests that the models may have an underlying weakness when predicting unstable flow that is not related to the formulation of turbulent Prandtl number, and that Kay's formulation will likely not lead to any significant

improvement. Future research could investigate improved models for prediction of buoyancy effects on turbulence.
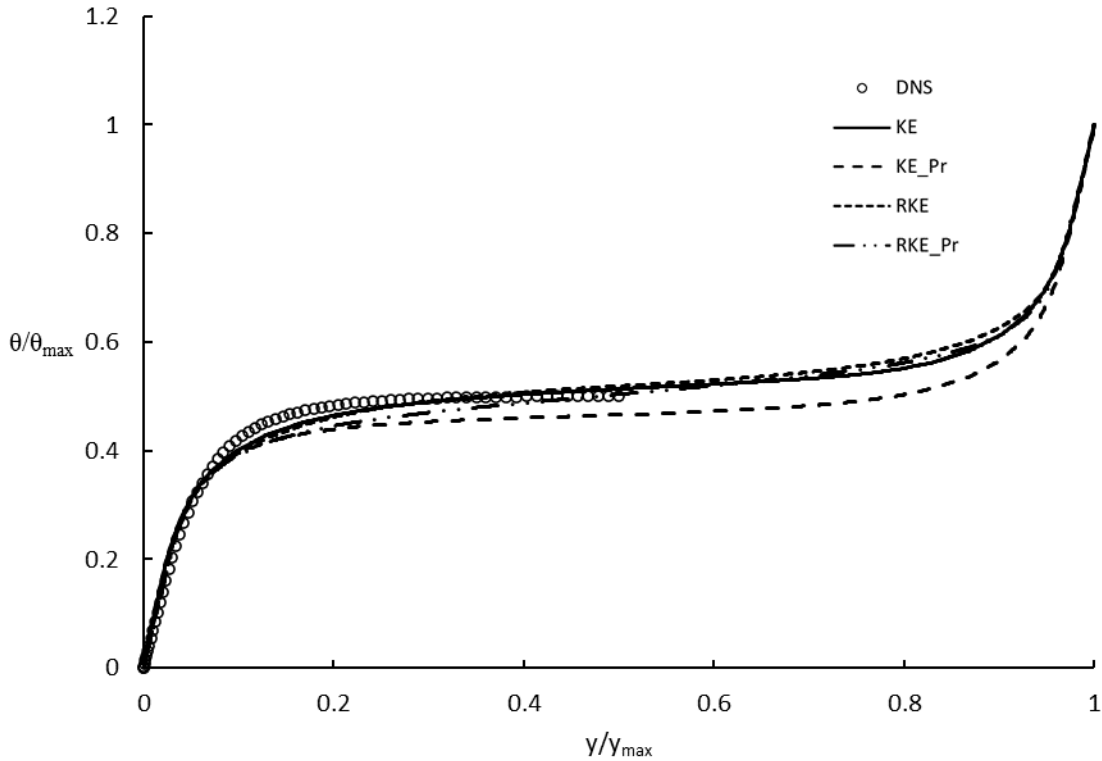

Figure 27: Non-dimensional temperature profiles for all models in an unstable horizontal channel with buoyancy and asymmetric boundary temperatures at Re=150, Pr=0.7, Gr=1.3e6

The temperature data shown in Figure 27 shows relative agreement between the models and DNS results. Though no model predicts the temperature as reported in DNS results, the models do follow the same behavior. Results show agreement in the near wall region of the flow but begin to differ in the buffer region. The thermal simulation data across all models is relatively consistent, apart from the k-ε model with Kay's formulation. This model more accurately predicts the flattened behavior of the DNS toward the middle of the channel, but slightly underpredicts the solution, much more than the other models. There is no clear reason why this difference occurs, though the unstable nature of this case could be a cause.

Figure 28: Non-dimensional velocity profiles for all models in a stable horizontal channel with buoyancy and asymmetric boundary temperatures at Re=150, Gr=4.4e6

For the velocity data for the stable horizontal channel, shown in Figure 28, everything inside the log-law region of the flow agrees well between all models and the DNS. The models do not, however, agree with the digitized data in the center of the channel. The k-ε models accurately predict the flow farther from the wall than the realizable models do, however, this difference is small. As mentioned above for the unstable case, further improvement of the velocity prediction may be possible by focusing on the details of the buoyancy model form.
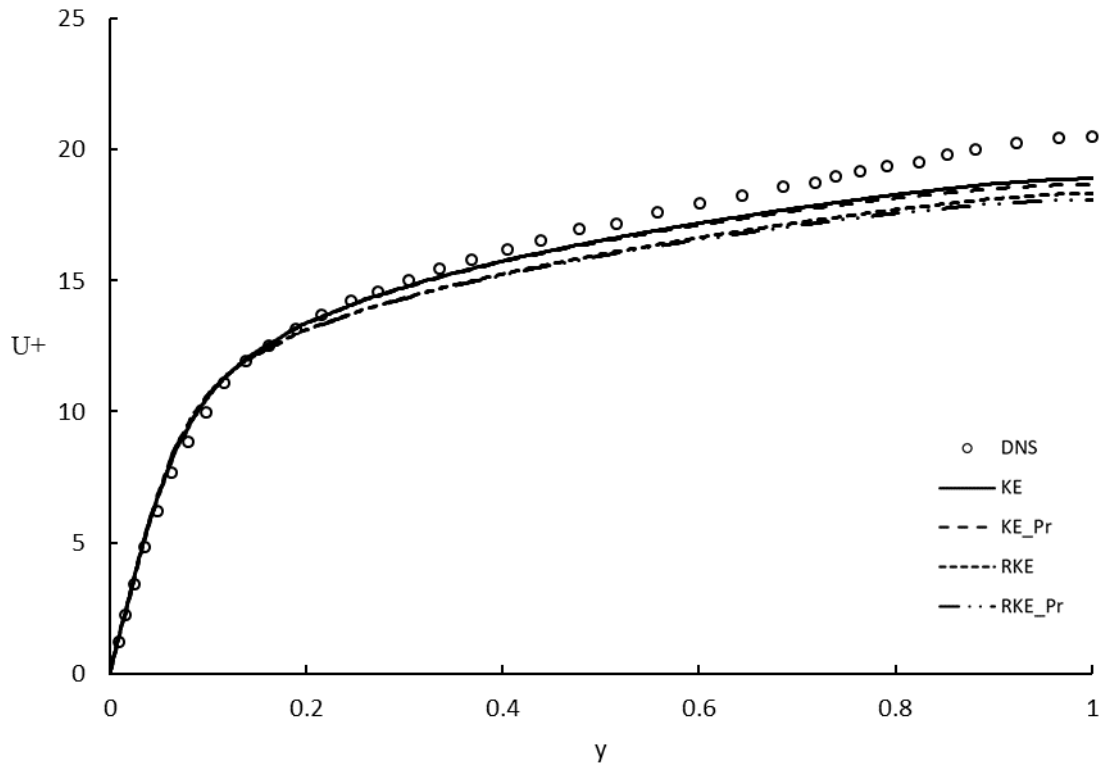
Figure 29: Non-dimensional temperature profiles for all models in a stable horizontal channel with buoyancy and asymmetric boundary temperatures at Re=150, Pr=0.7, Gr=4.4e6

The thermal data matches DNS closely in Figure 29. In the buffer layer there is some separation however all models come back to the same profile and continue to agree overall. Though the difference is small, the standard k-ε models are in closer agreement to the digitized data than the realizable models are.

Figure 30: Non-dimensional velocity profiles for all models in a vertical channel with buoyancy and asymmetric boundary temperatures at Re=150, Gr=9.6e6

Figure 30 shows predicted velocity profiles for the case of a vertical channel with buoyancy effects. The concept of an aiding side (y<1) and opposing side (y>1) is evident. On the aiding side, the hot wall produces a buoyancy force in the upward direction, while the opposite occurs on the opposing side. All models follow the same profile as DNS data, however, k-ε slightly underpredicts just outside the buffer layer, yet overpredicts slightly closer to the center of the channel where realizable k-ε underpredicts slightly. The models all underpredict the flow where the buoyant force is greater.
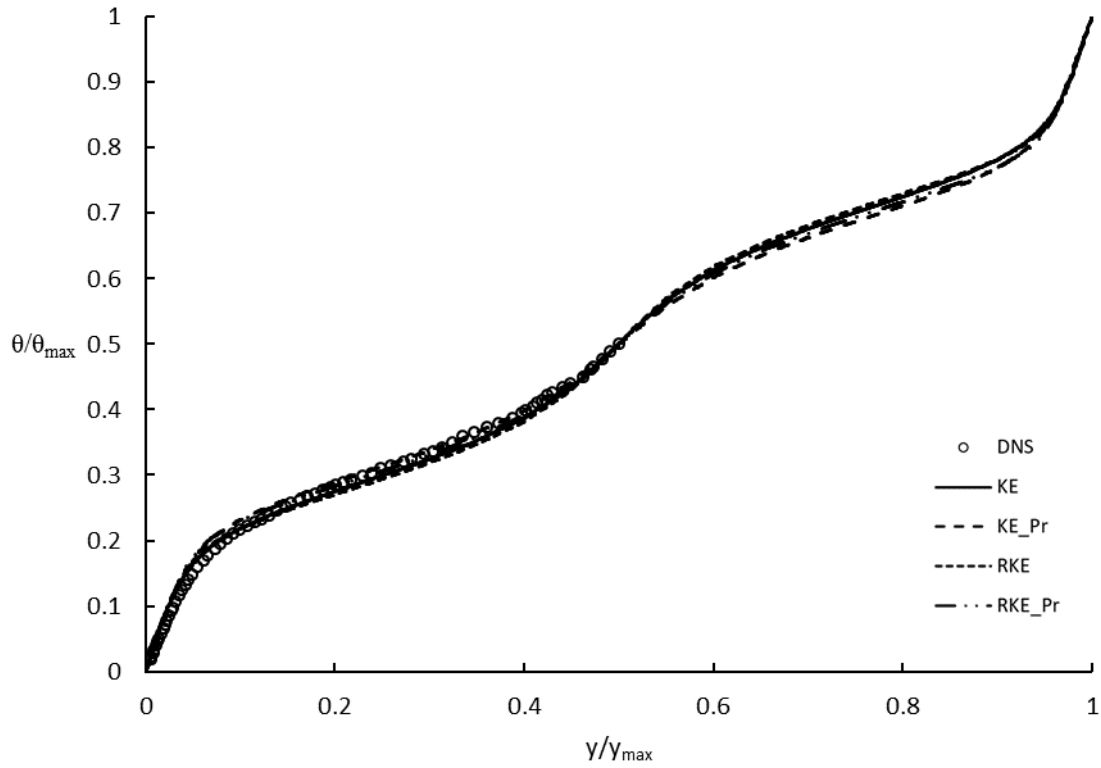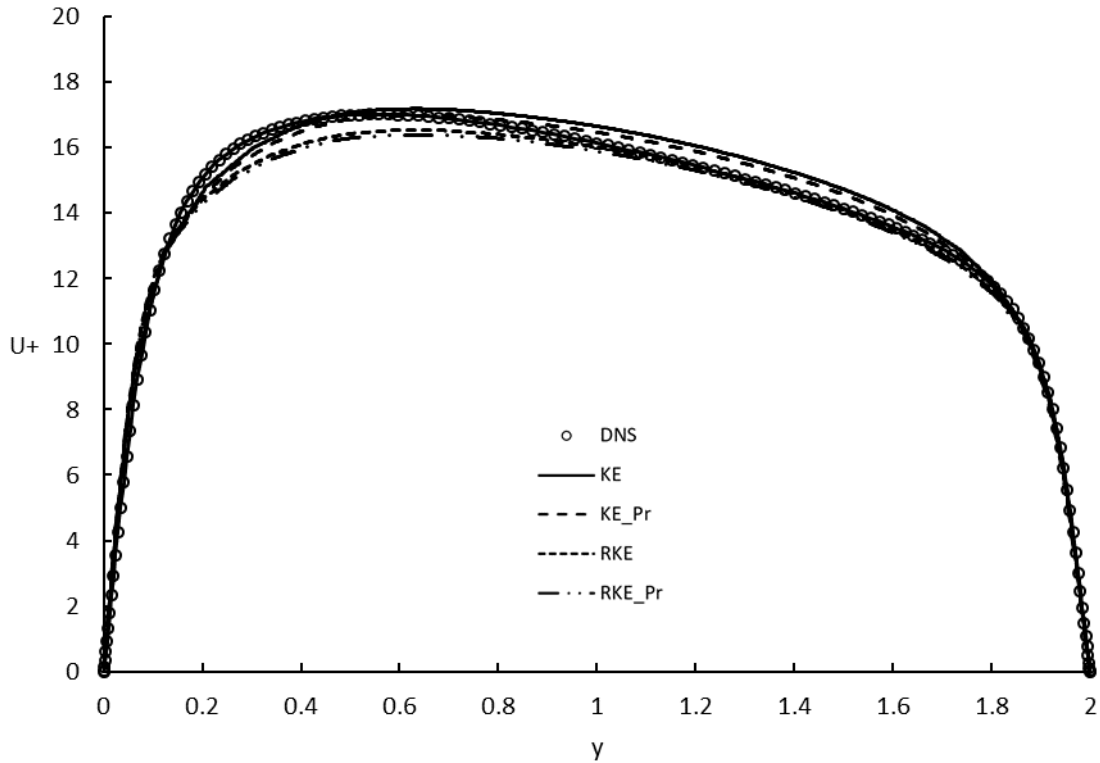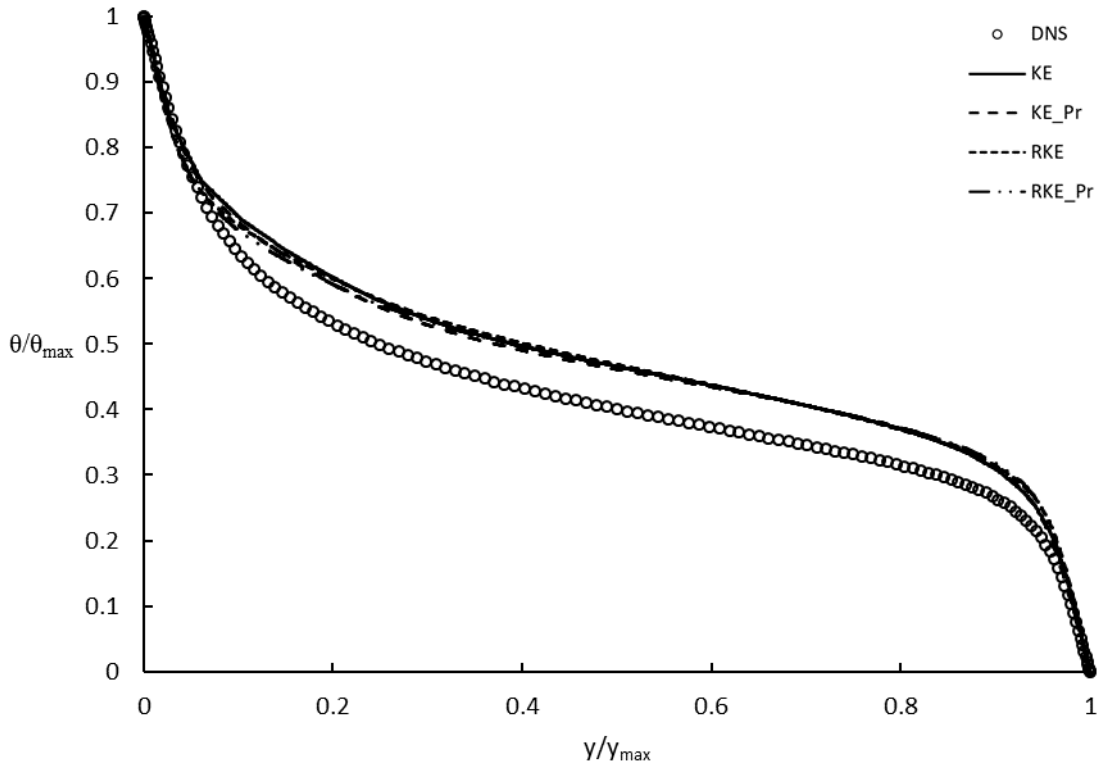
Figure 31: Non-dimensional temperature profiles for all models in a stable horizontal channel with buoyancy and asymmetric boundary temperatures at Re=150, Pr=0.7, Gr=9.6e6

Figure 31 shows that the temperature distribution for this case is not accurately modeled when compared to the DNS. All models predict the near wall behavior as expected, however, outside of the viscous sublayer all models significantly overpredict, around 18%, the DNS results.

For the channel flow test cases, thermal results all show improvement from the implementation of Kay's formulation, other than the vertical channel case. Considering all models performed similarly regarding momentum, the models with Kay's formulation have an advantage to be viable for reducing error in modeling flows, especially when Pr is low. No apparent advantage, or disadvantage, seems to appear for Pr numbers comparable to air. Further, looking at the data from cases with Re=180, it seems the accuracy of Kay's formulation increases inversely with Pr number, making this a possible solution for simple flow geometries when solving for low Pr number fluids.

Backward Facing Step Case Results
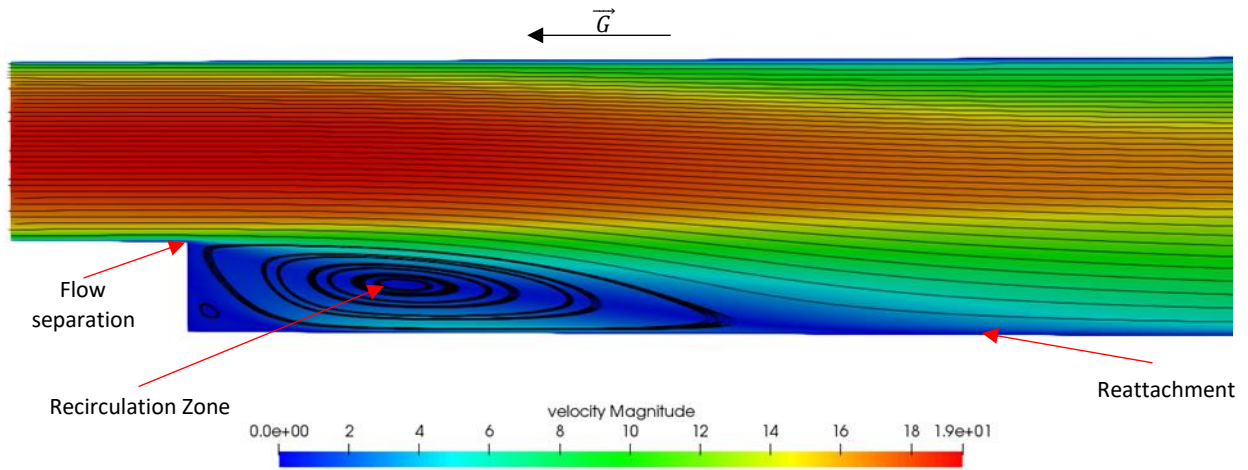
Figure 32: Diagram illustrating a typical backward facing step flow field and important regions

Figure 32 shows a velocity magnitude contour with a streamline overlay for the Niemann and Frohlich, non-buoyant case. This image helps to visualize the flow field and the locations in the flow where separation, reattachment, and recirculation zones occur.

Figure 33: Velocity flow field for a non-buoyant backward facing step with interposed streamlines

Figure 34: Thermal flow field for a non-buoyant backward facing step with interposed streamlines

Figure 35: Turbulence kinetic energy flow field for a non-buoyant backward facing step with interposed streamlines

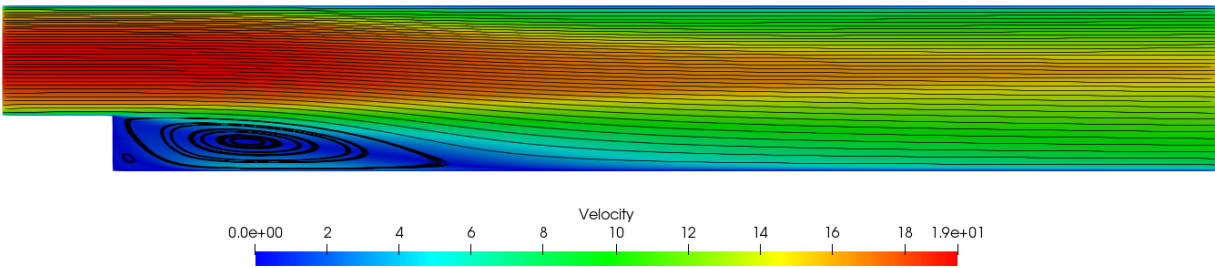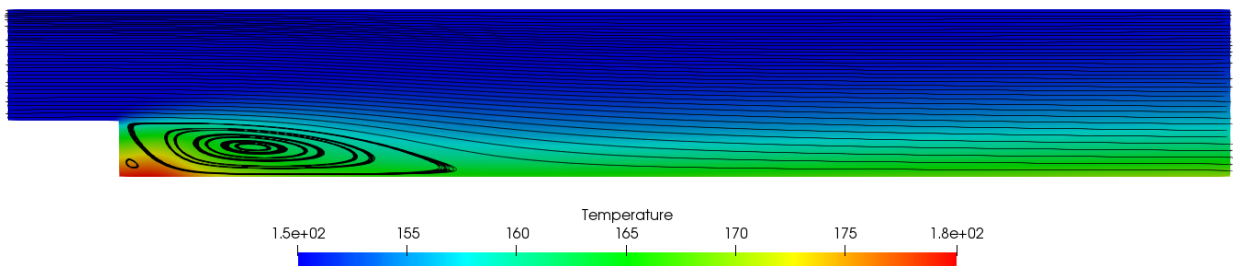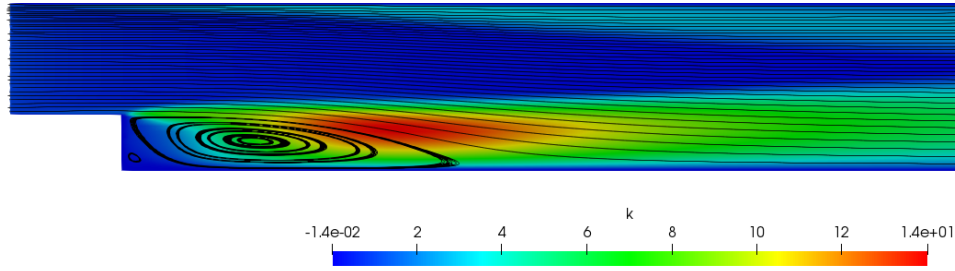The velocity contour for the Niemann and Frohlich case without buoyancy is shown in Figure 33. The thermal heat map and streamline overlay are also included to visualize the effect the recirculation zone has on the heating of the fluid in Figure 34. It shows that in the recirculation zone where the fluid velocity is much lower, the hot wall heats the fluid substantially more than where the velocity is higher. The effect this recirculation zone has on cases with buoyancy is significant. Figure 35 shows turbulence kinetic energy (k) for a non-buoyant backward facing step. From the contour, the effect of the recirculation zone has on the turbulence in the flow field is apparent. In particular, high turbulence production is apparent in the shear layer between the freestream flow and the recirculation region.
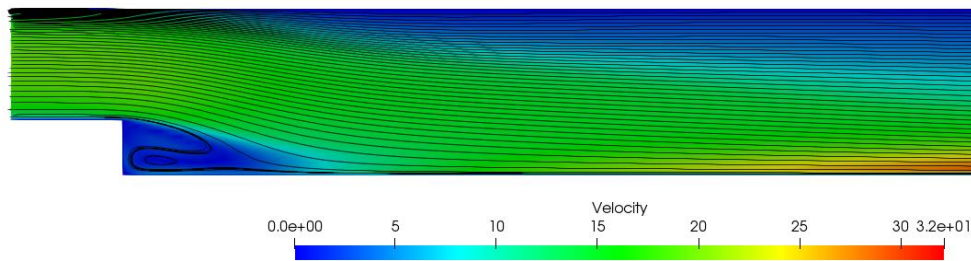

Figure 36: Velocity flow field for a buoyant backward facing step with interposed streamlines
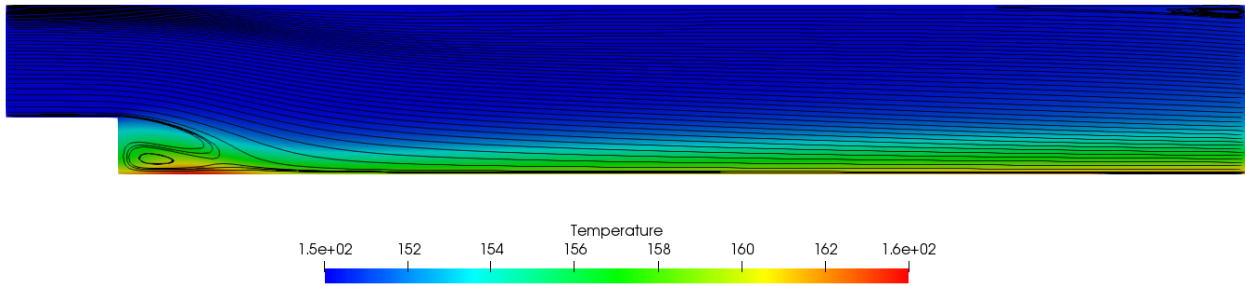
Figure 37: Thermal flow field for a buoyant backward facing step with interposed streamlines
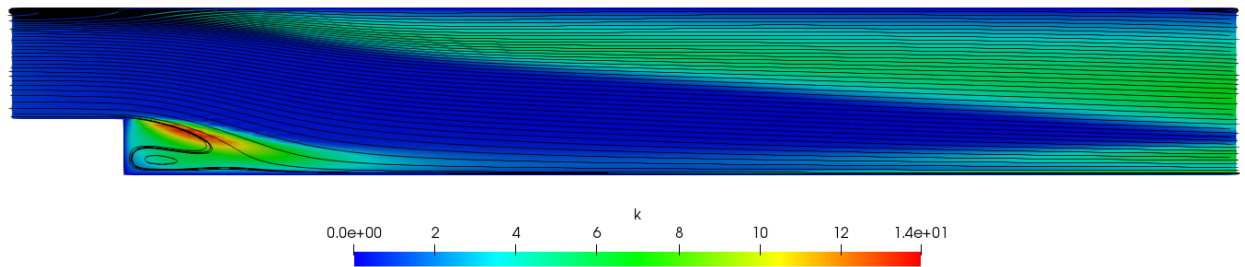

Figure 38: Turbulence kinetic energy flow field for a buoyant backward facing step with interposed streamlines

Figures 36, 37, and 38 are contours of variables with streamline overlays for the buoyant case of Niemann and Frohlich. From the velocity contour, Figure 36, it is apparent how the buoyancy is affecting the flow. Referencing the non-buoyant velocity contour, Figure 33, introducing buoyancy into the flow heavily influences the velocity near the hot wall. Due to the temperature causing the fluid to rise, the recirculation zone is not necessarily recirculating fluid as it did without buoyancy. Finally, Figure 38 shows the turbulence kinetic energy. From the contour the difference in the distribution of turbulence between the buoyant and non-buoyant cases is clear.

Data for the Niemann Frohlich cases are plotted according to x/H, their position with respect to the overall channel height. For reference, the main channel is pictured in the methodology section, Figure 2. Data in this section is presented in pairs of plots. The vertical axis on the left of each plot indicates the value of x/H along the channel and the right axis represents the spacing between each x/H plot to indicate the magnitude of velocity and or temperature. The

left plot pictures the standard k-ε model, with and without Kay's formulation, and the right-hand plot corresponds to strictly realizable k-ε model data. This description is for Figures 39-44.

Niemann and Frohlich Backward Facing Step Cases

Non-Buoyant

(a)   (b)

Figure 39: Velocity buoyant Niemann Frohlich backward facing step, plotted with respect to x/H for (a) Standard k-eps and (b) Realizable k-eps

Overall velocity data for the non-buoyant Niemann Frohlich case in is close agreement with the DNS results. Though the models seem to generally have the same behavior and very similar values in the near wall region, they do seem to all under-predict DNS moving toward the

center of the channel. Though the effect is slight, the models increasingly overpredict centerline

flow as x/H becomes larger.

Figure 40: Temperature data for non-buoyant Niemann Frohlich backward facing step, plotted
with respect to x/H for (a) Standard k-eps (b) Realizable k-eps

The thermal data for the non-buoyant Niemann Frohlich case in Figure 40 shows good

agreement with the DNS. The models with Kays formulation seem to do a better job predicting

throughout the channel. For both velocity and temperature data k-ε and realizable k-ε seem to

perform quite closely with a slight advantage to the realizable models. This advantage can be seen

in the plots looking at x/H=3, shortly after the step. At this location, there is a slight advantage,

more so close to the heated wall, for the realizable models. From indications in this case, the results

would suggest Kay's formulation models perform better than their constant turbulent heat flux counterpart, in addition to realizable k-ε being the more accurate of the two.
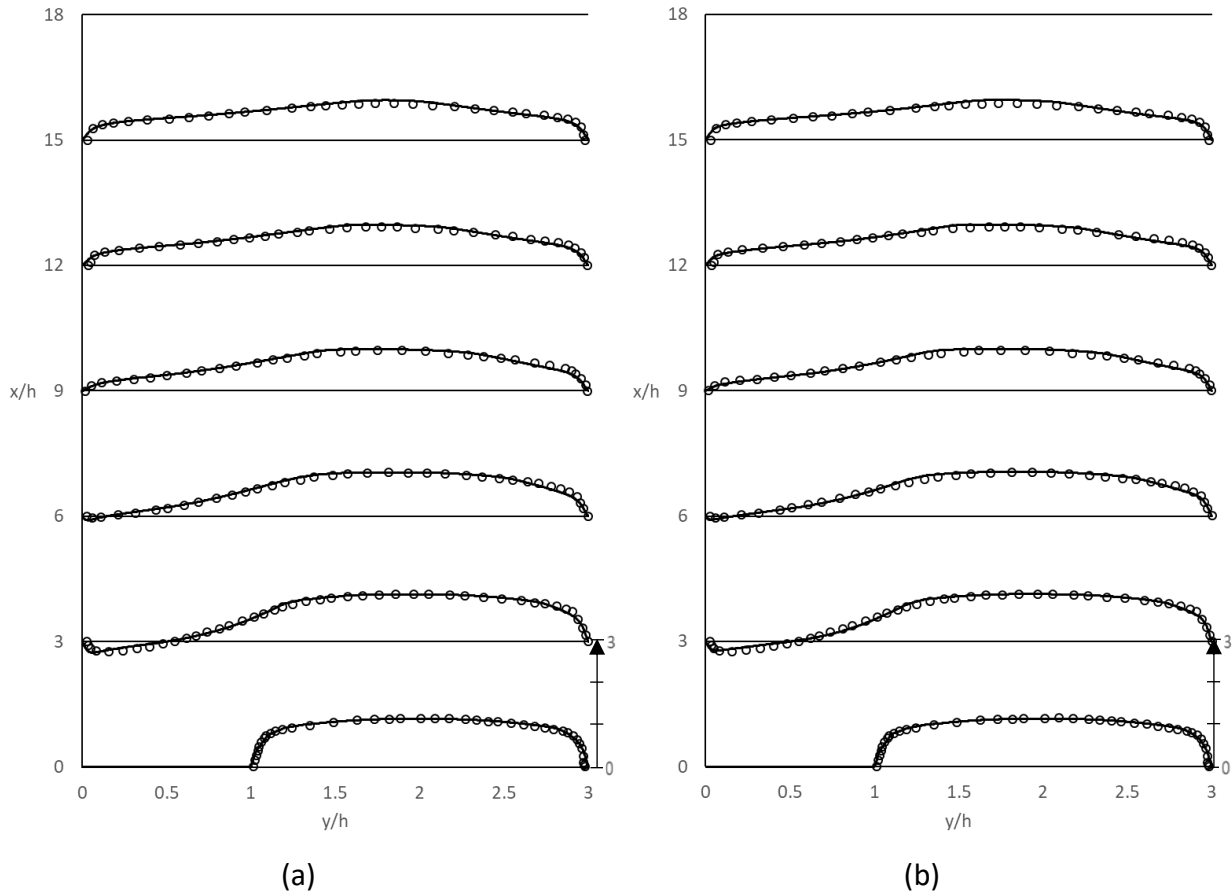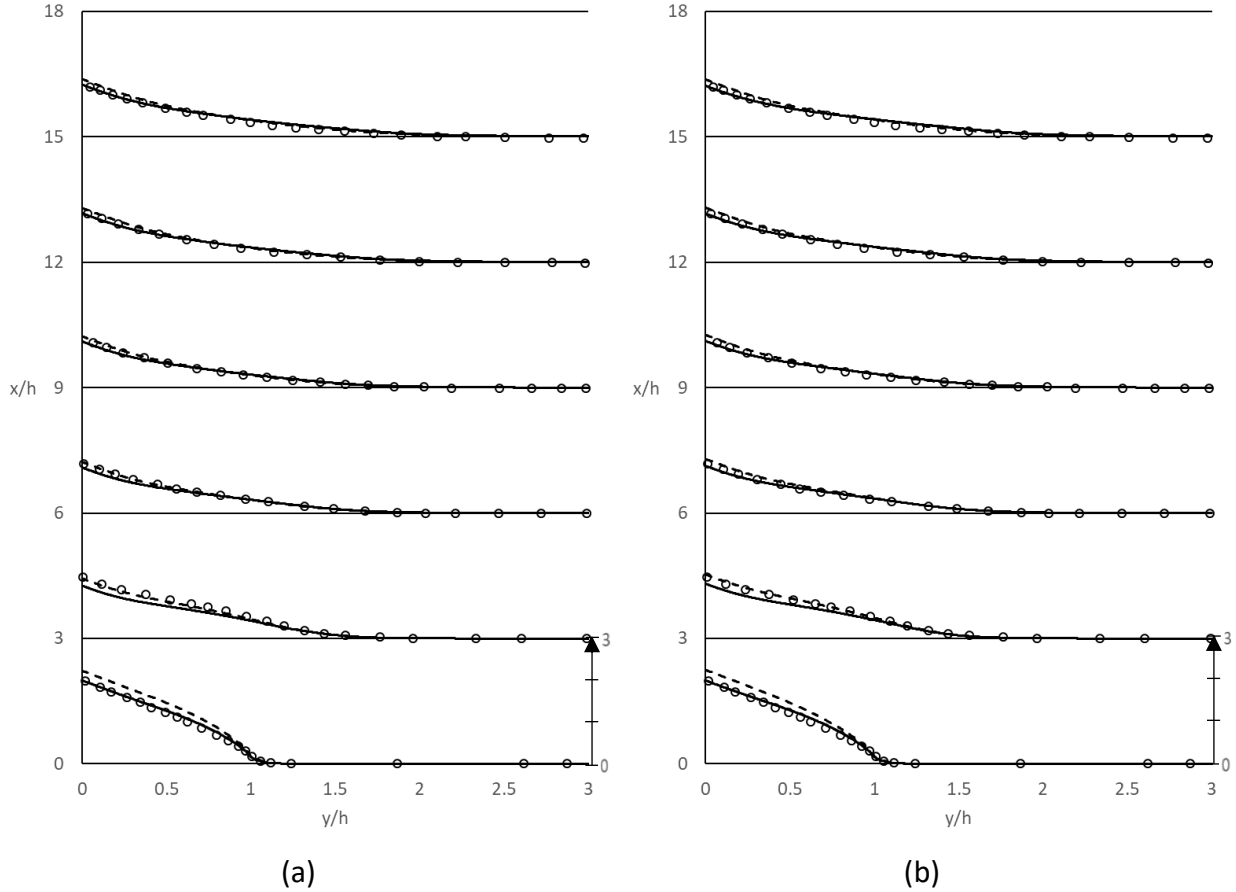
Buoyant

Figure 41: Velocity data for buoyant Niemann Frohlich backward facing step, plotted with respect to x/H for (a) Standard k-eps (b) Realizable k-eps

Velocity data shown in Figure 41 from the buoyant Niemann Frohlich case shows different behavior than the non-buoyant case. The models start to underpredict between the buffer layer and centerline, then moving to the center the models start to overpredict. Based on these results, it appears that the models start off in good agreement before the step, however, the step seems to throw them slightly askew. The models seem to recover after the region with the recirculation

zone, first near the heated wall where buoyant forces are relatively high, then at the far wall for increasing values of x/H.
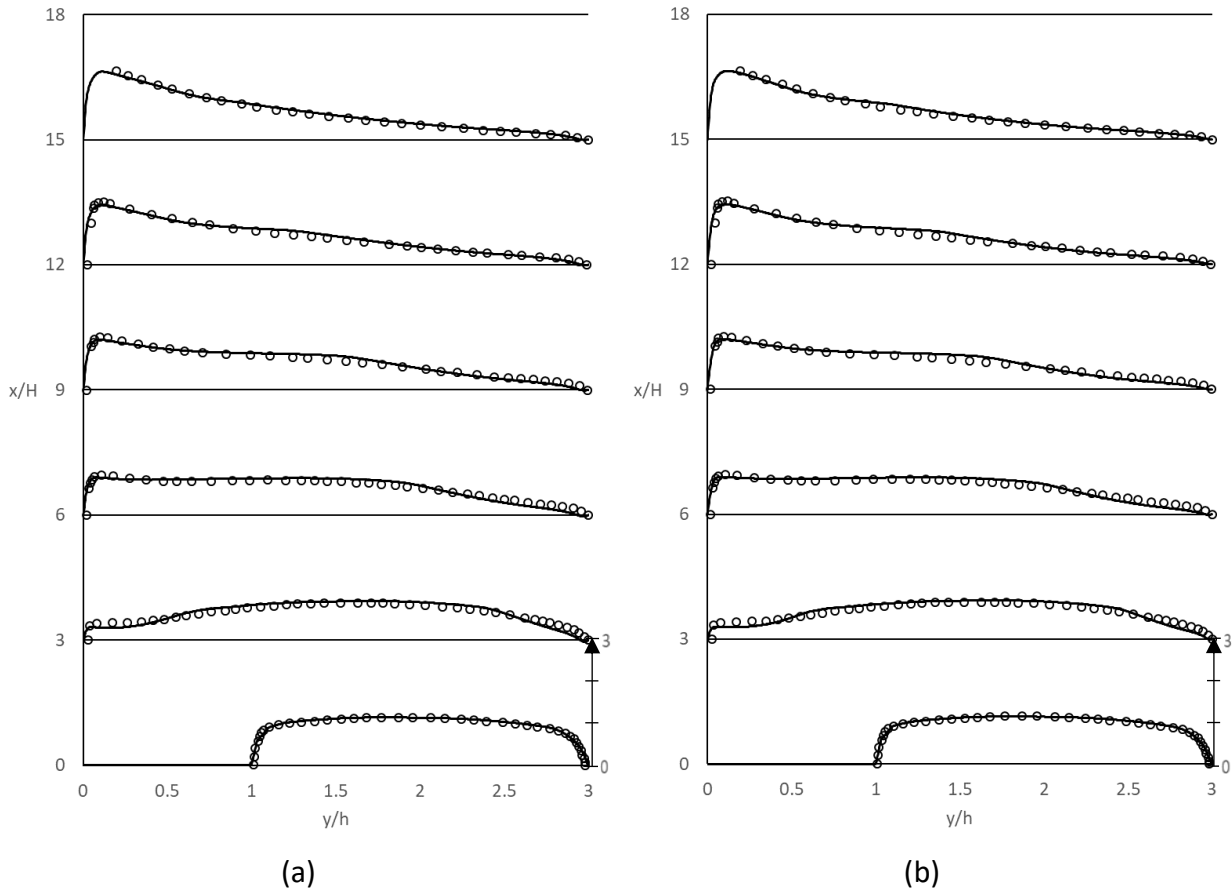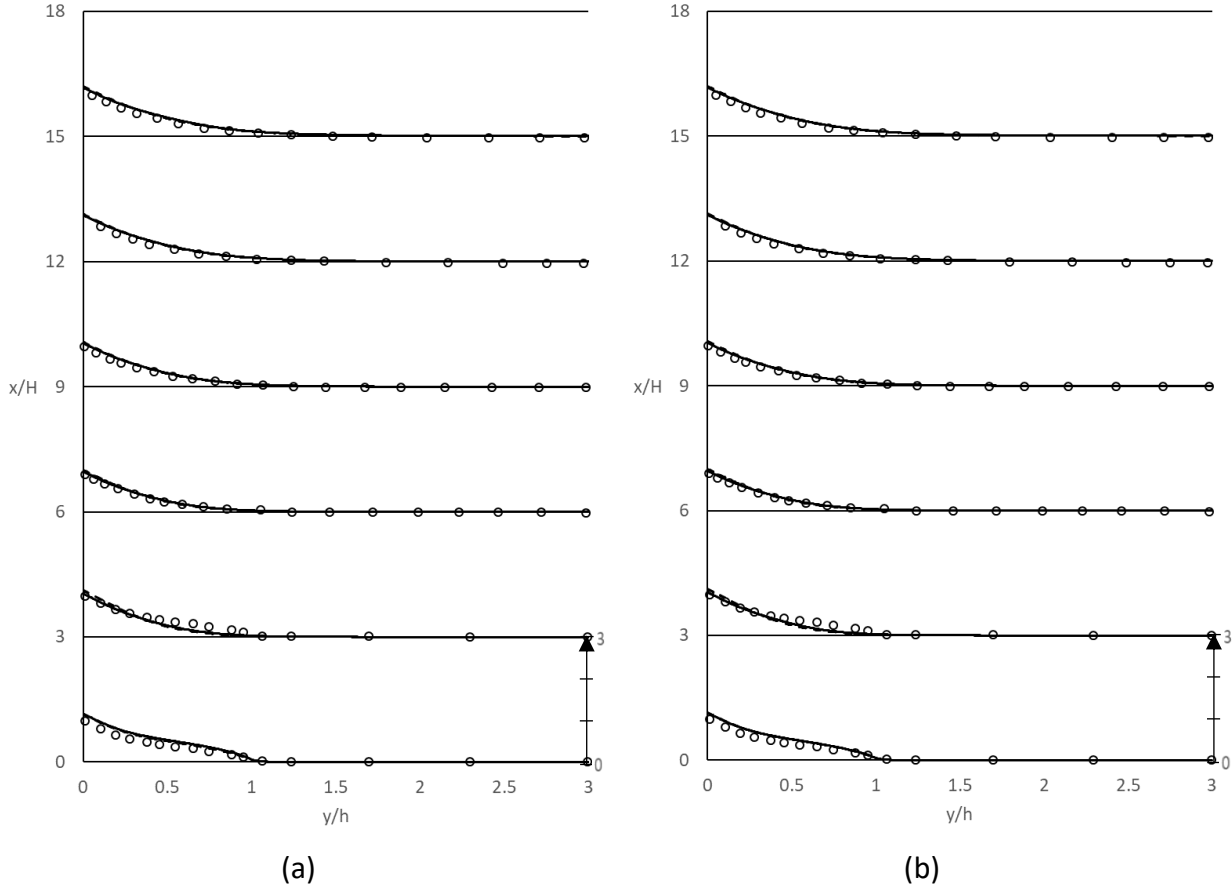

Figure 42: Temperature data for buoyant Niemann Frohlich backward facing step, plotted with respect to x/H for (a) Standard k-eps (b) Realizable k-eps

The temperature results for the buoyant case of Niemann and Frohlich agree with DNS. The two models have significantly closer agreement here than in the non-buoyant case, in addition the Kay's formulation models are also in closer agreement. All models seem to predict the temperature well, overall, with some slight deviation in the buffer layer shortly after the backward facing step, at x/H=3.

Vogel and Eaton Backward Facing Step Case

Figure 43: Velocity data for Vogel Eaton backward facing step, plotted with respect to x/H for (a) Standard k-eps (b) Realizable k-eps

Figure 43 shows that both sets of models behave nearly identically to one another. The only difference perceptible is in the reattachment length. The values show less agreement near the wall for the standard models than for the realizable. All models seem to underpredict slightly in the buffer layer and log-law region and near the heated wall.
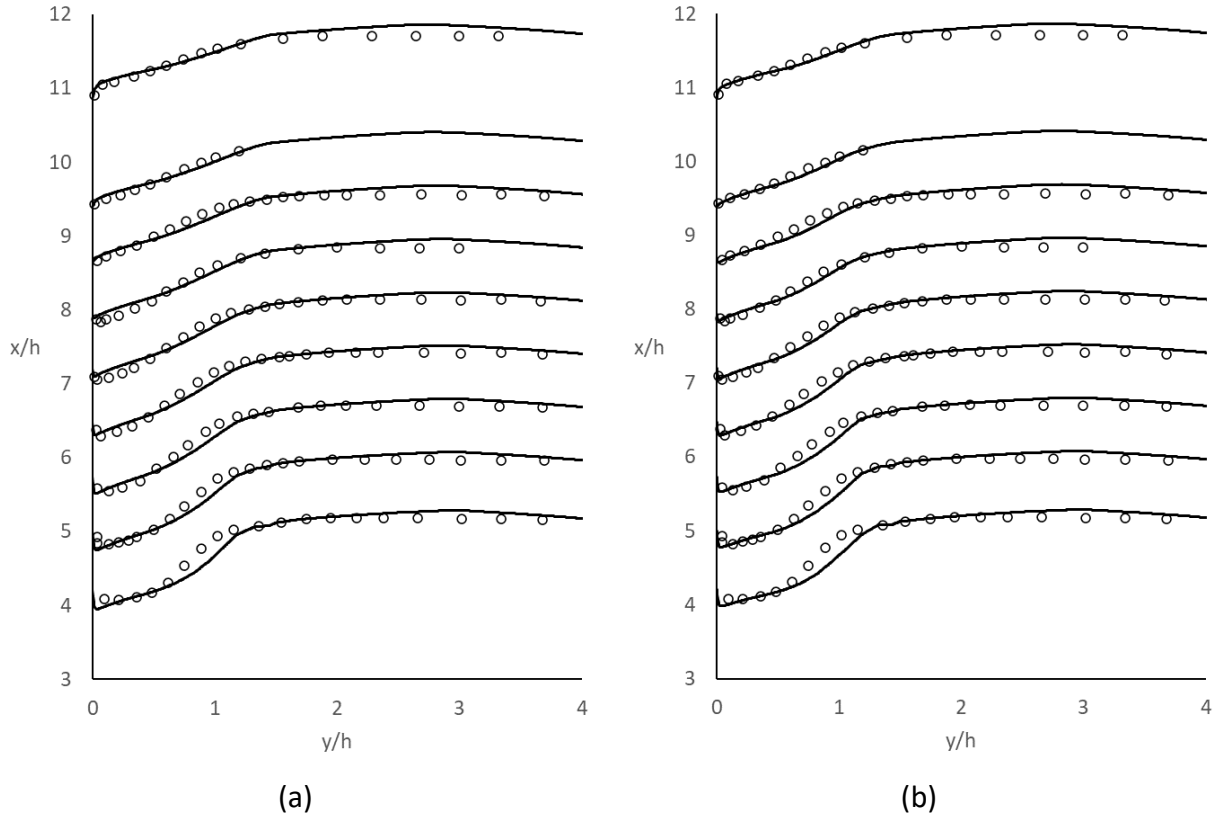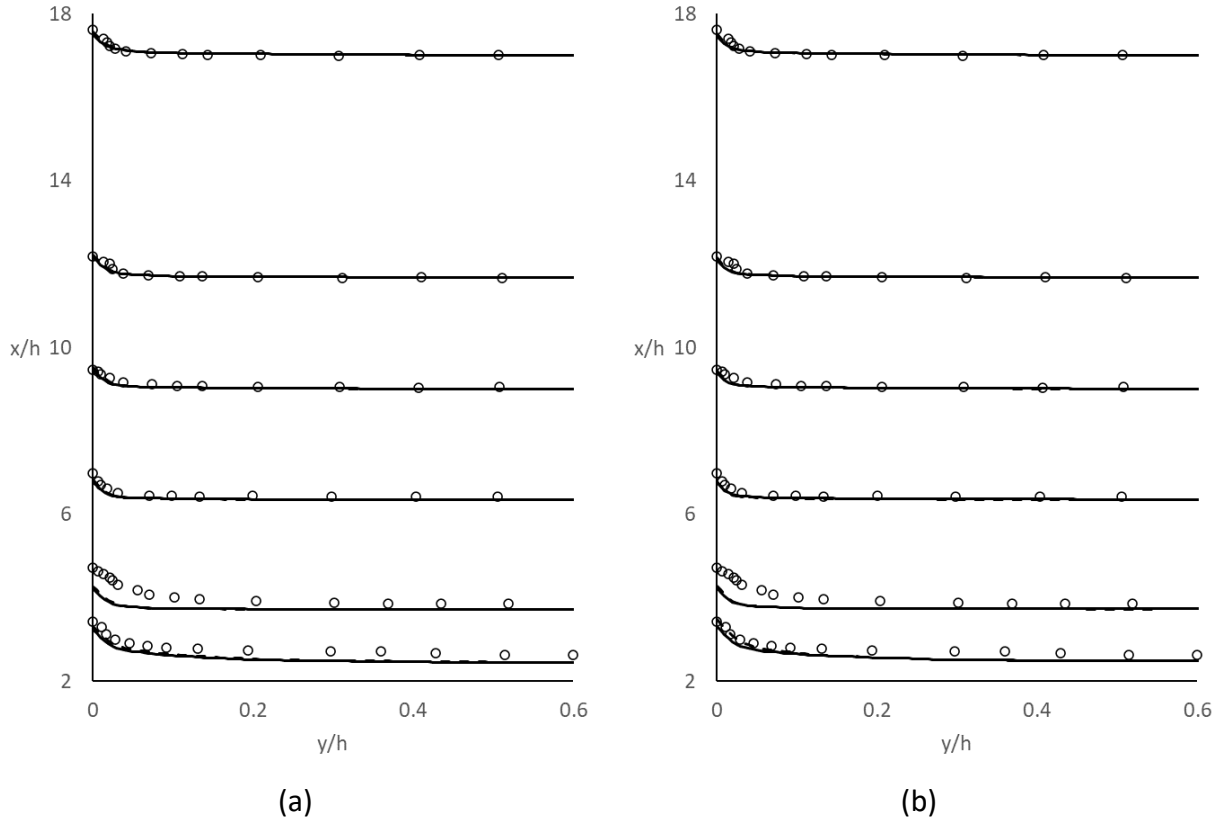
Figure 44: Temperature data for Vogel Eaton backward facing step, plotted with respect to x/H for (a) Standard k-eps (b) Realizable k-eps

Temperature data reflects results found in velocity plots. The models, though they follow the same trend as the DNS throughout, underpredict around the step. Underpredicting temperature significantly in the layers near the wall other than that of the viscous sublayer. The data follows a similar pattern as velocity, in that the models seem to predict much better outside of the recirculation zone.

The data seems to show that the realizable model is an improvement on the standard model in predicting low Pr number flows for backward facing step geometries. Though the results indicate a slight improvement to the models with the implementation of Kay's formulation, the difference is small. All data sets, with the exception of the x/h=0 data set presented in Figure 40, show favorable results for Kay's formulation, or are equivalent between models with Pr

modification and those without. The results for the backward facing step cases as a whole do not offer enough insight to conclude Kay's formulation as a clear improvement, however, results show that Kay's formulation does not result in any large differences to models without the modification except in regions of flow separation where buoyancy effects are not considered.

Benchmark Rod Bundle Case Results

The rod bundle cases were run as a benchmark case to validate the models for low-Pr number flows for more complex geometries, beyond standard plane channel and backward facing step simulations, particularly for use in the nuclear energy industry. Predicting behavior of these fluids is vital for further development of Gen IV reactor cooling technology.
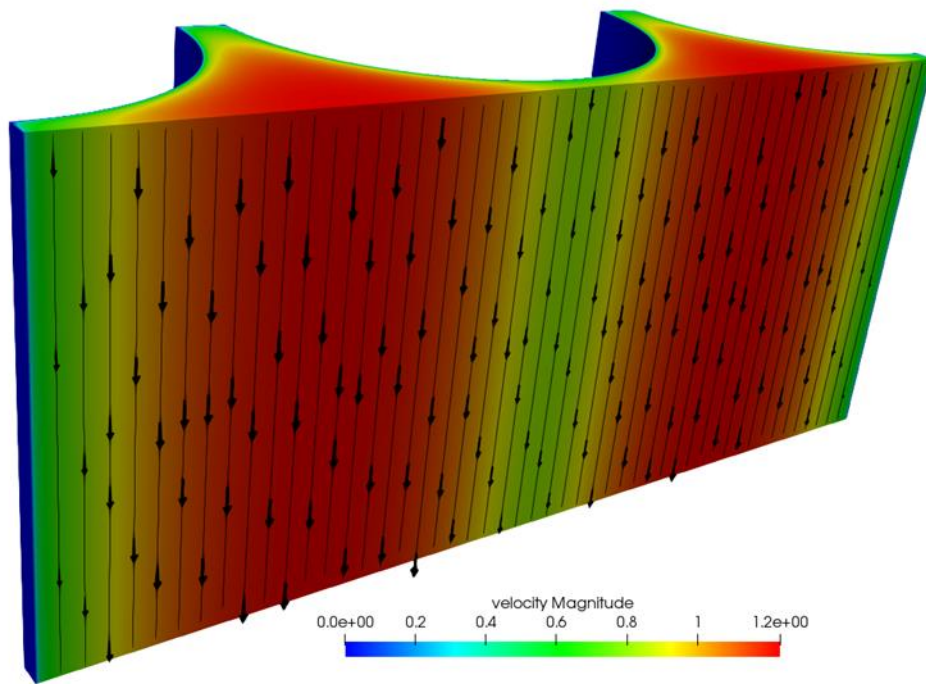
Figure 45: Velocity flow field with streamlines overlaid for the benchmark rod bundle case

Figure 45 shows that the flow behaves as expected. The velocity is maximum at the farthest distance away from the rods, in the middle of the flow field, and slower near the walls and spacers

where shear stress is higher. Though mostly qualitative the figure helps visualize the flow. To further help understand the data presented in this document, it is important to visualize where data was plotted in the flow field. Figure 46 shows the three lines of interest where the DNS data was compared to plotted model results.

Figure 46: Plot lines interposed on rod bundle geometry

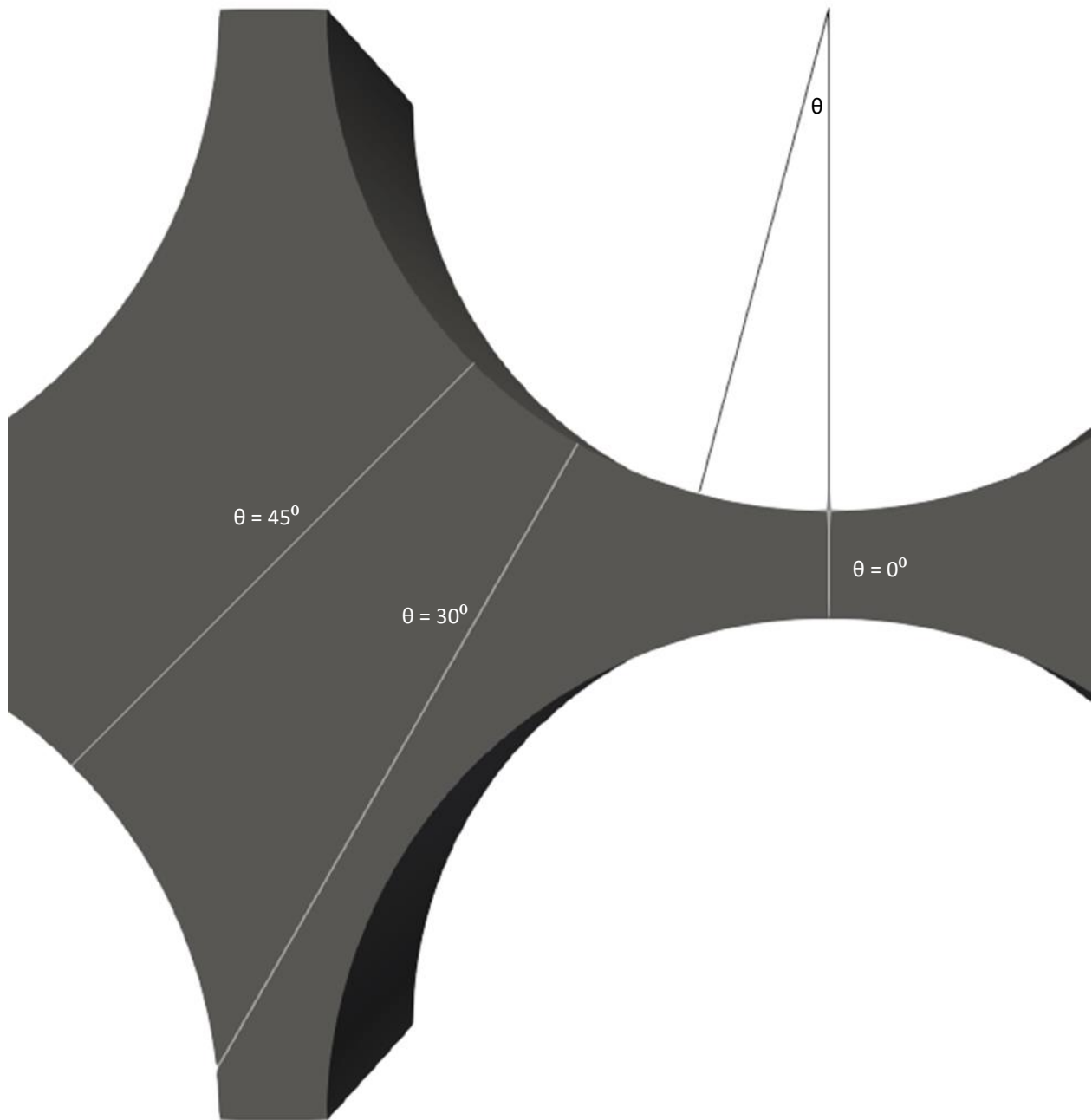Of particular interest are the values of θ at 0° and 45°. These locations have both momentum and thermal DNS data available where $\theta = 30^\circ$ has only velocity data to compare with.
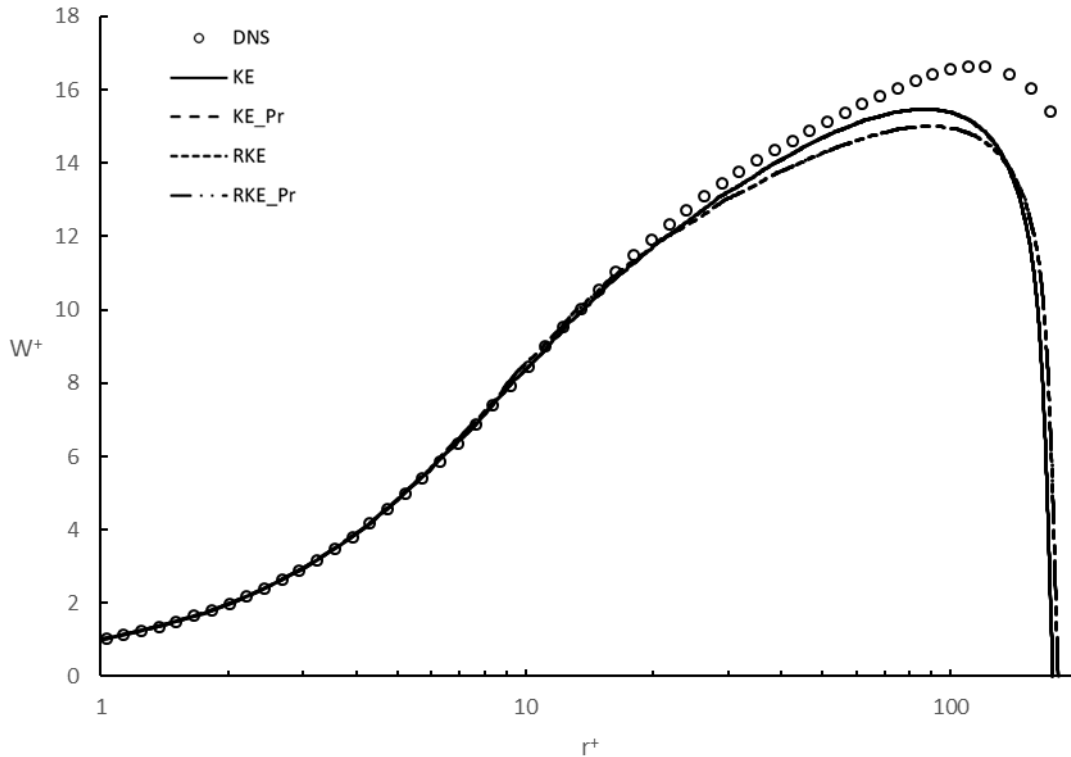

Figure 47: Velocity data non-dimensionalized by shear stress for $\theta=0^\circ$ (inner scaled)

The plot above is the plot of velocity at $\theta=0^\circ$ where the variables have been non-dimensionalized by inner scaling. This refers to the typical way fluid parameters are non-dimensionalized with the shear stress and the physical parameters, i.e. U+, y+, except in this case, W+ and r+. From Figure 47 the maximum value of velocity in the z direction for the DNS is substantially higher than the models predicted. The behavior in the viscous sublayer of the flow is predicted very well by the RANS models, as well as extending well into the buffer layer. One discrepancy in the models that can be seen in the plot is the plots for both realizable models are extended past their standard counterparts. This indicates a difference in shear stress between

models. This can be traced to the different values of the constant A_μ between the two models. This in turn affects μ_t causing a higher stress in the realizable case. A clearer comparison of the simulation data to DNS can be seen by plotting W/w_b vs r/r_{max} as shown in Figure 48.
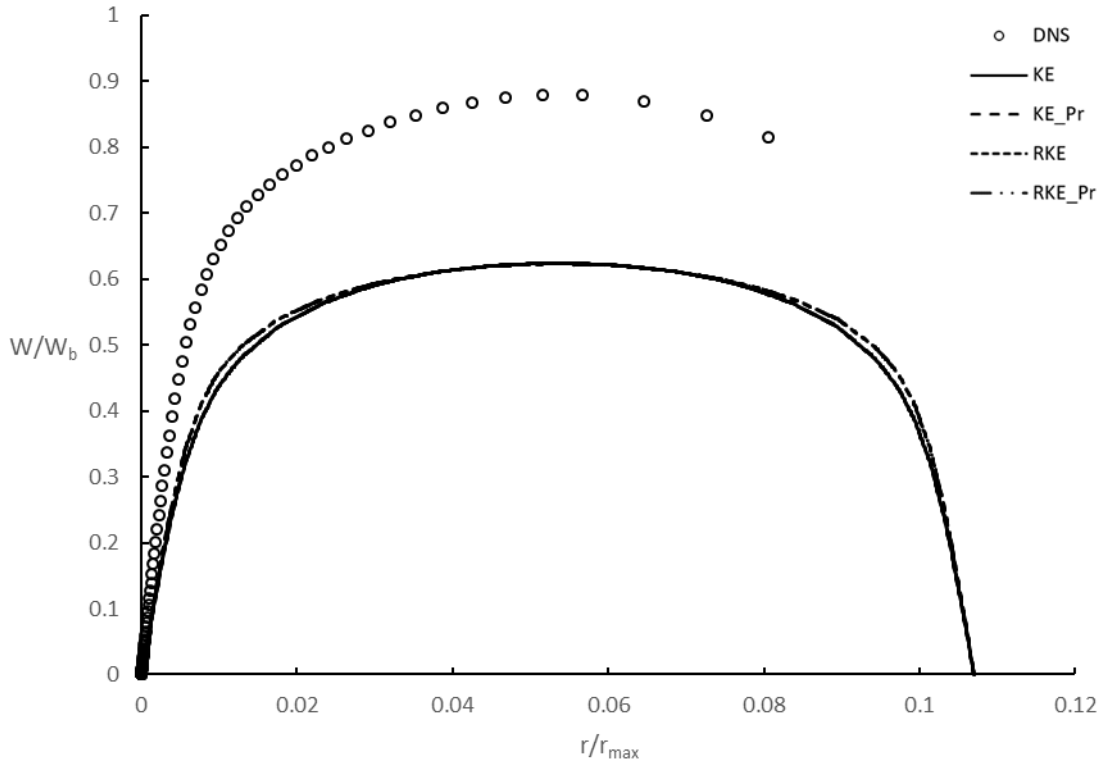

Figure 48: Velocity data non-dimensionalized by bulk velocity and maximum distance from the wall for $\theta=0^0$ (outer scaled)

From Figure 48 the behavior of the model compared to DNS is almost identical, however the magnitude is much different, about 28%. Due to assumption in RANS models of isotropic stress with the fact the stress is dictated primarily by the gradients in the wall normal direction, the fluctuations in the flow tangent to the wall are underpredicted. Figure 48 clearly indicates that there is much more flow in the streamwise direction than the RANS models predict. There is also a discrepancy in the prediction for the flow between the gaps in the rod bundle, this will be discussed further with temperature results.
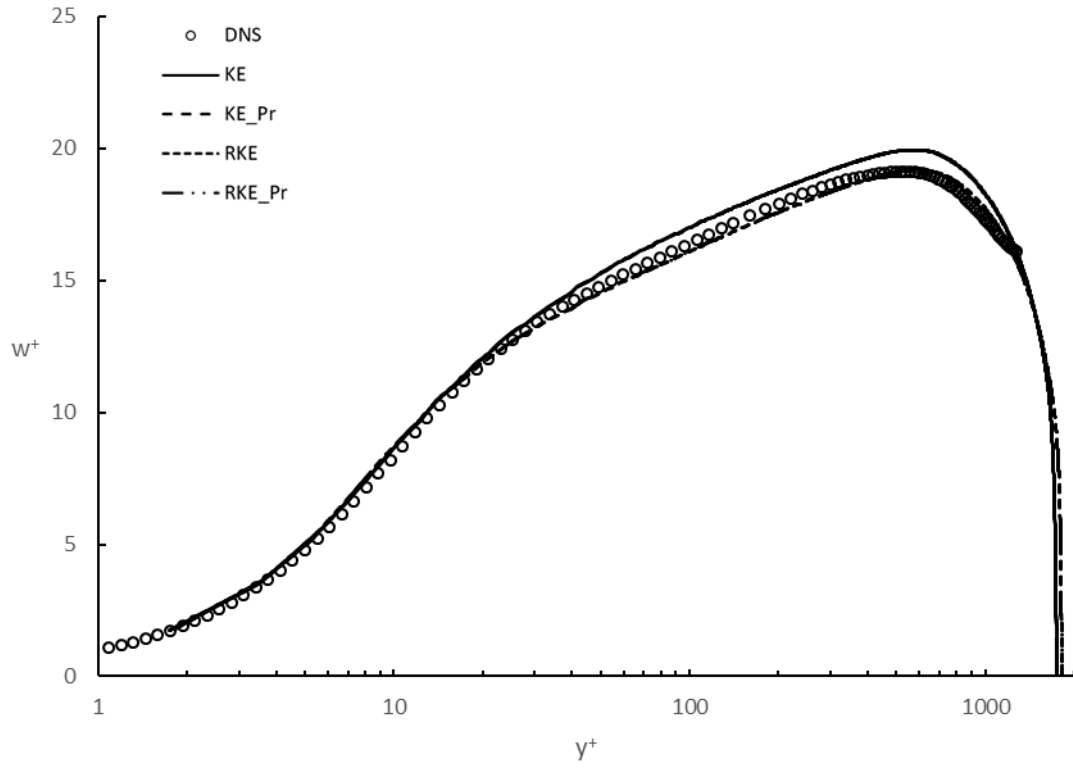
(a)
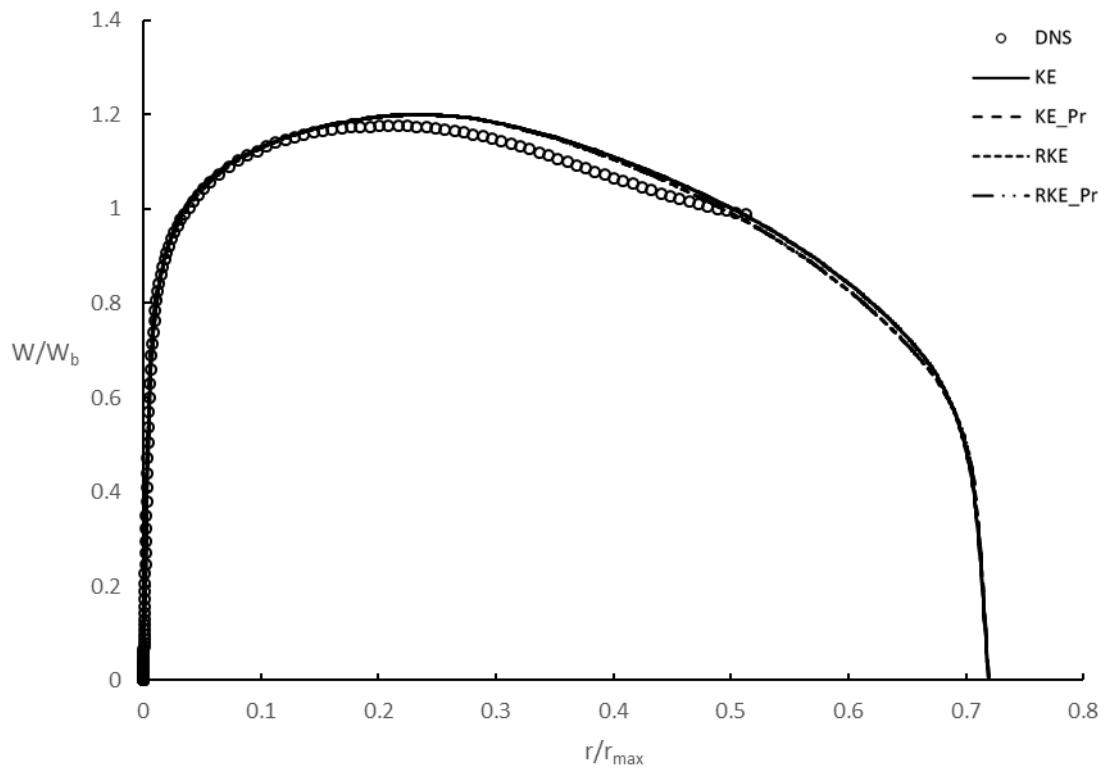
(b)

Figure 49: Non-dimensional velocity data for $\theta=30^{\circ}$ (a) inner scaled (b) outer scaled

The data at $\theta=30^\circ$ tells largely the same story as $\theta=0^\circ$ with exception in the magnitude inaccuracy. The models more closely predict the flow here than at $\theta=0^\circ$. From the inner scaled plot, Figure 49, one can see that in the same manner as before. The model shows good agreement in the viscous sublayer and buffer layer. Outside of those layers, it appears that the realizable models do a better job in the log-law region and then again toward the center of the channel.
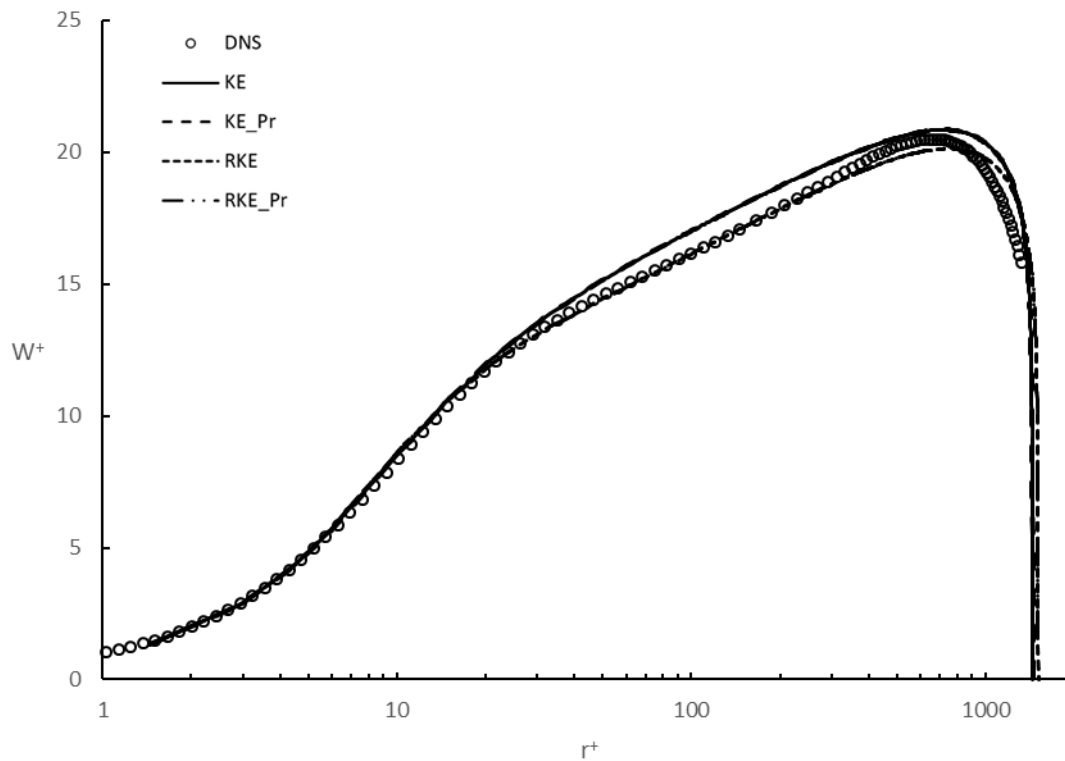
(a)
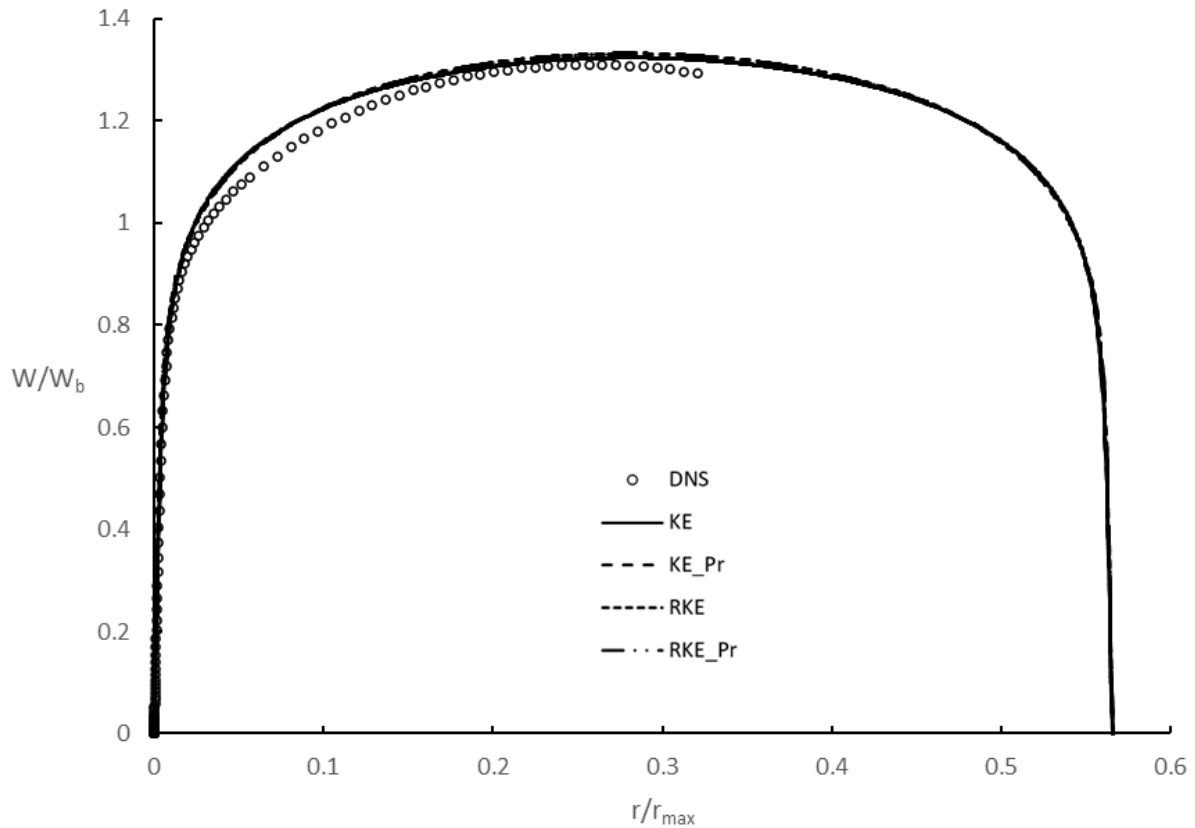
(b)
Figure 50: Non-dimensional velocity data for $\theta=45^\circ$ (a) inner scaled (b) outer scaled

A similar discussion follows for $\theta=45^\circ$, behavior in the viscous sublayer and buffer layer is nearly identical to DNS. The models deviate from DNS slightly in the log-law layer, where the standard models overpredict slightly, less than 5%, in this layer, the realizable models underpredict. However, both arrive at similar maximums in the center of the channel.

(a)

(b)
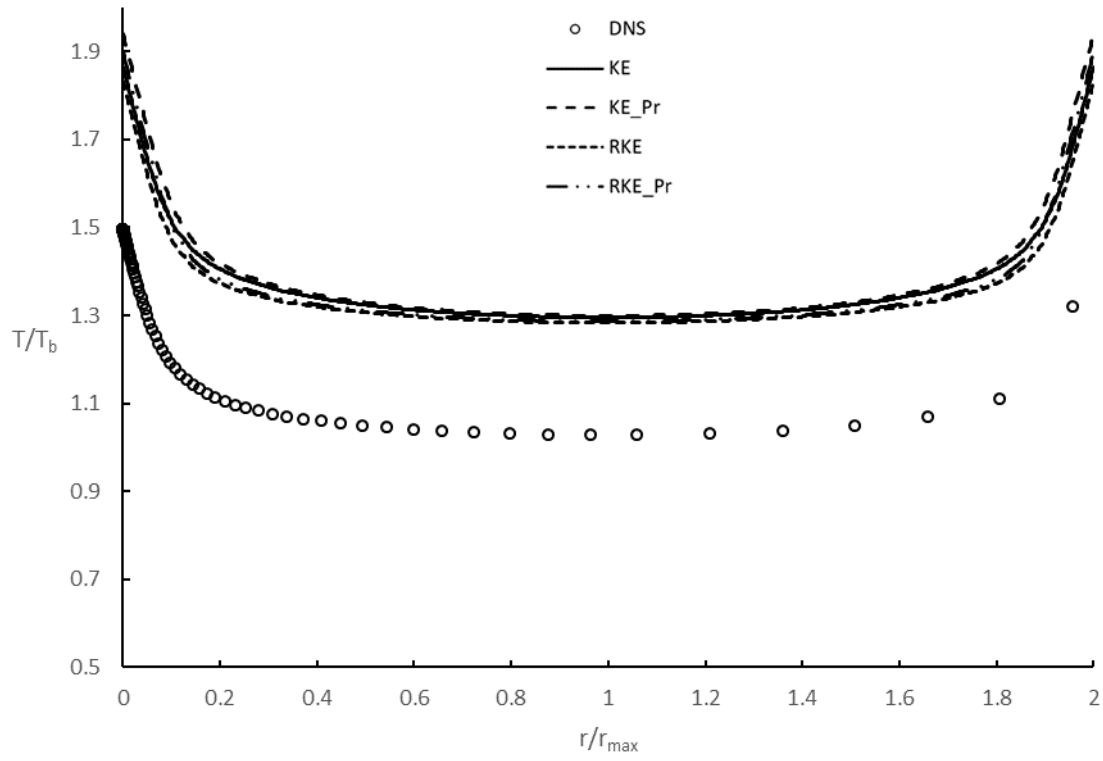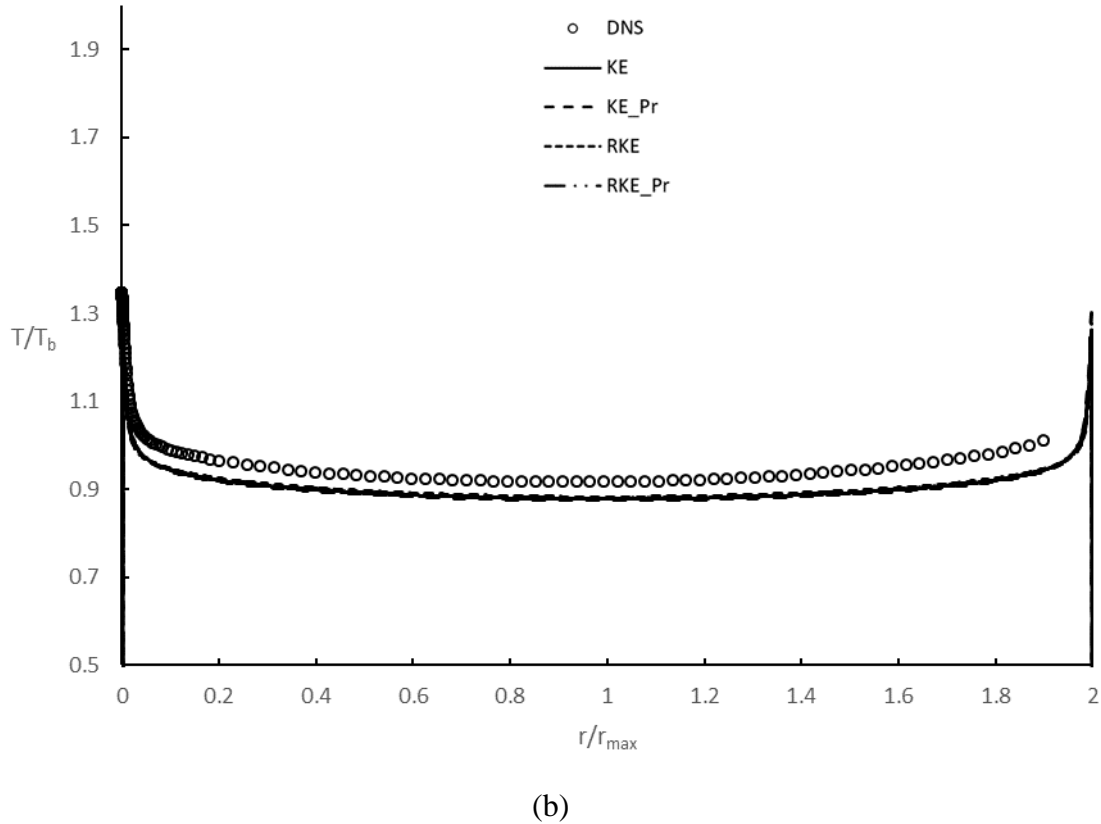
Figure 51: Non-dimensional temperature data for Pr=2 at (a) θ=0º and (b) θ=45º

The above plots, Figure 50 and 51, show the temperature data plotted at θ=0º and θ=45º respectively for the simulation with Pr=2. The models overpredict temperature at θ=0º and underpredict at θ=45º. However, if one considers how the RANS models wash out momentum fluctuations in flow between the rods, it follows that with less fluctuations, there will be less turbulent mixing, and with less mixing, less temperature diffusion in the working fluid. Therefore, this lack of turbulent mixing, accounts for the increased temperature profile when θ=0º and the decrease in temperature across the middle of the channel where θ=45º. This trend follows in all simulations with decreasing discrepancy between the DNS and the simulation data as shown in the following figures.
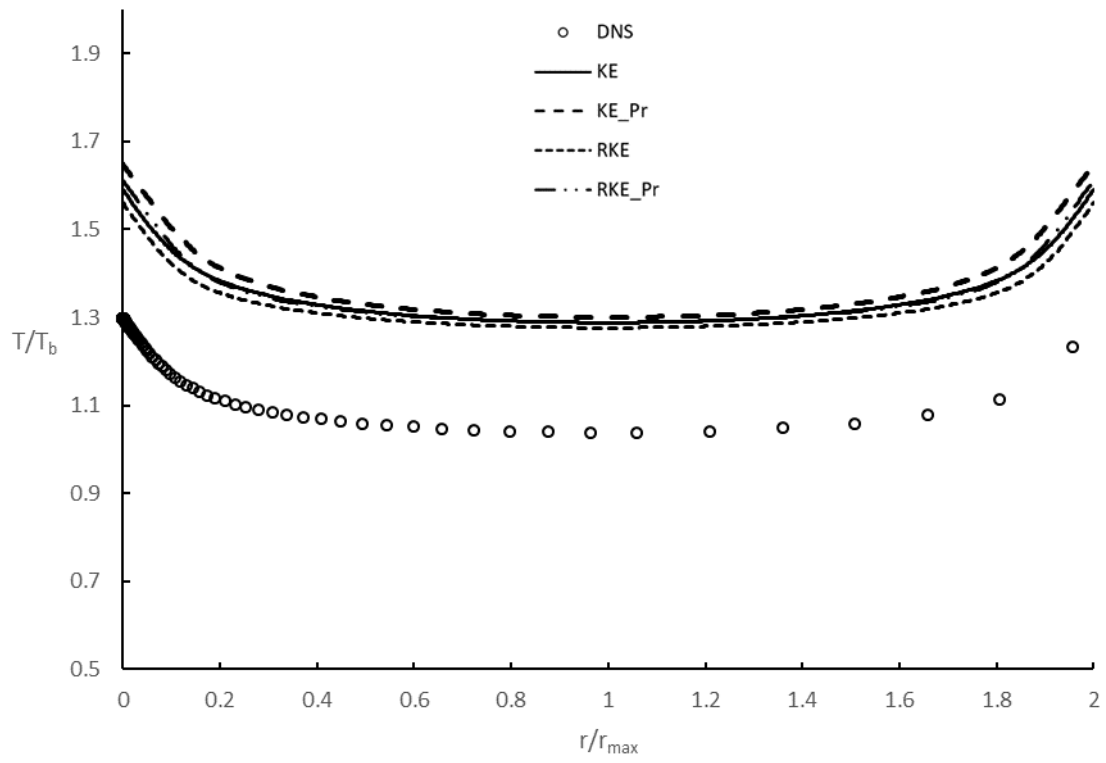
(a)
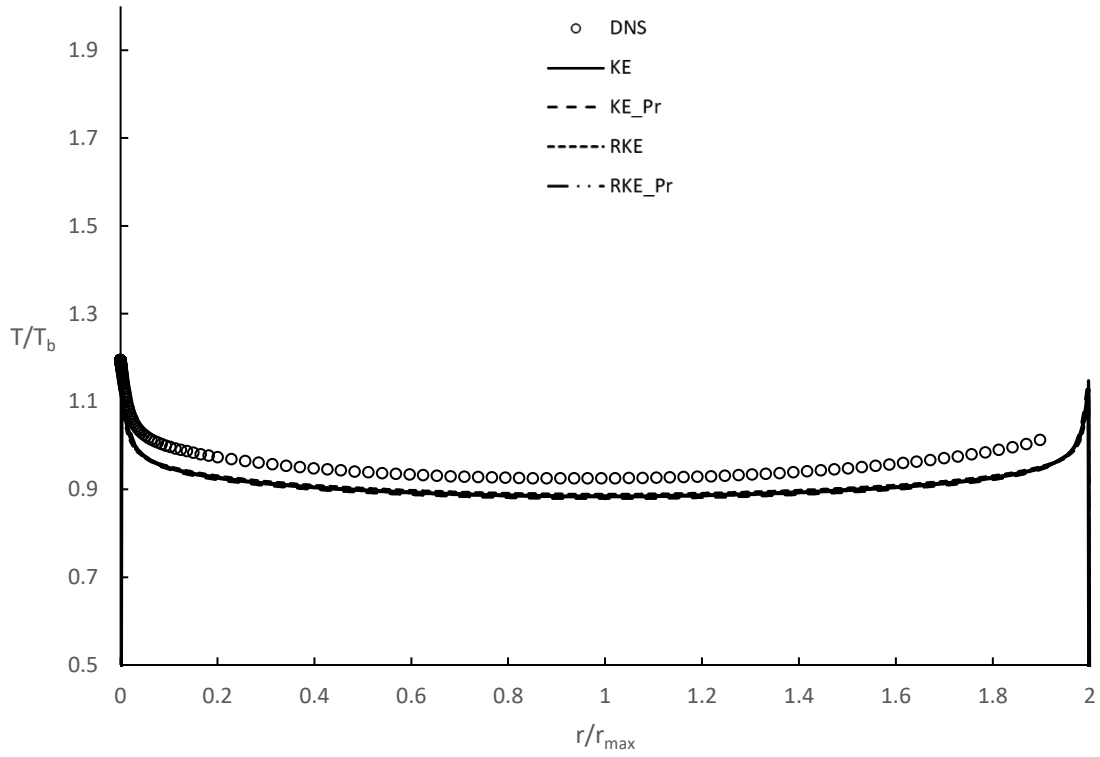
(b)

Figure 52: Non-dimensional temperature data for Pr=0.71 at (a) θ=0⁰ (b) θ=45⁰

Temperature profiles for the air-like Pr number mimic those of Pr=2, however, from the plots the difference is less drastic, as would stand to reason in a fluid with a relatively higher thermal conductivity than the first data set. Just as in the first data set, the profiles follow that of the DNS, yet the temperature discrepancy from the lack of mixing persists.
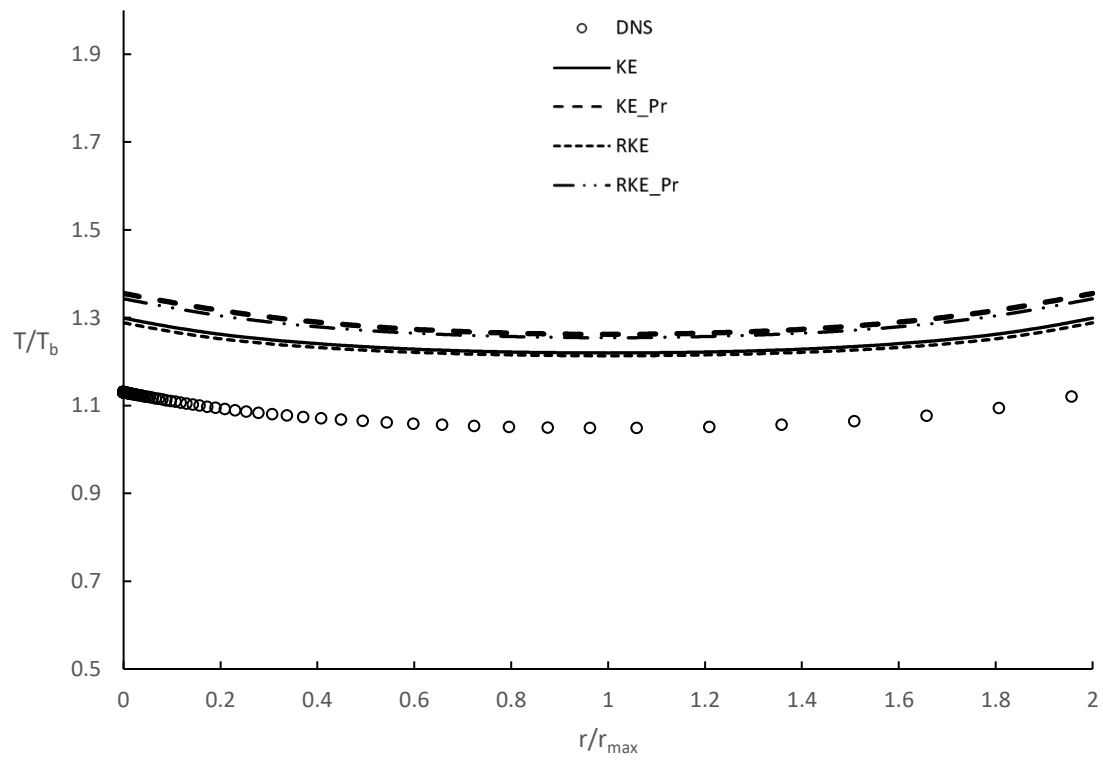
(a)
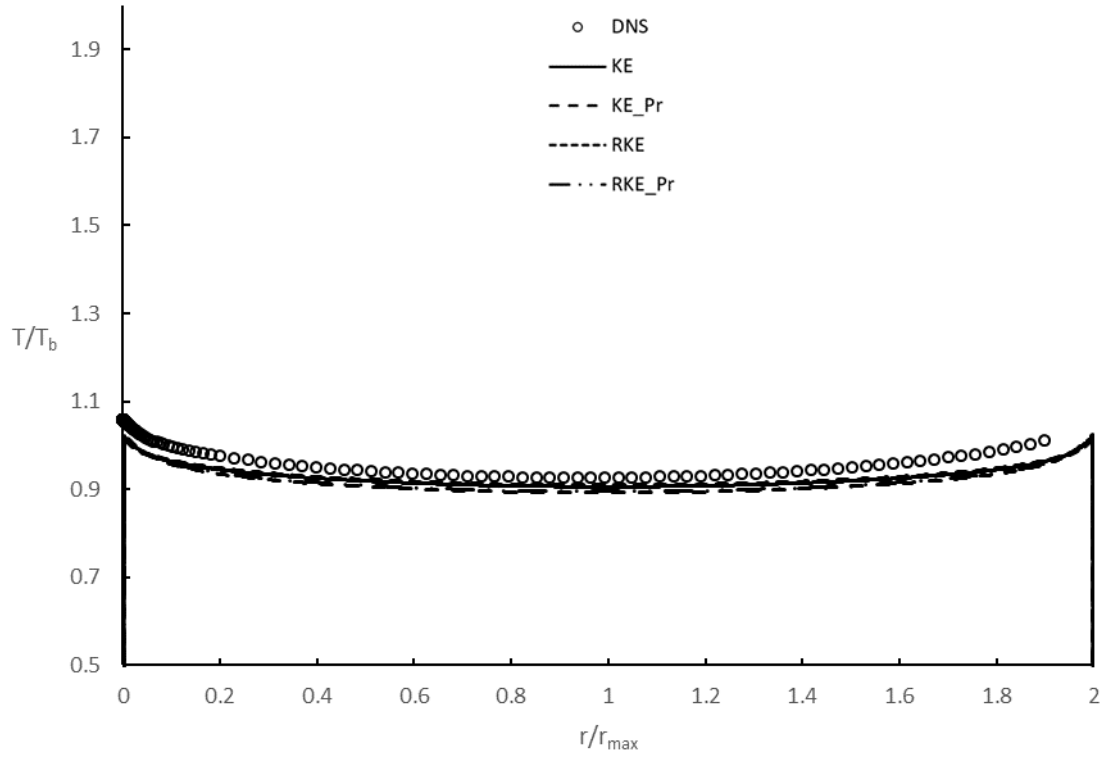
(b)

Figure 53: Non-dimensional temperature data for Pr=0.1 at (a) $\theta=0^{\circ}$ (b) $\theta=45^{\circ}$

For the temperature profiles for a lower Pr, one can see that the gaps between the DNS and the RANS data are narrowing. Though there is still some visible disagreement between values of the data, the profile continues to be consistently accurate over all models compared to DNS.
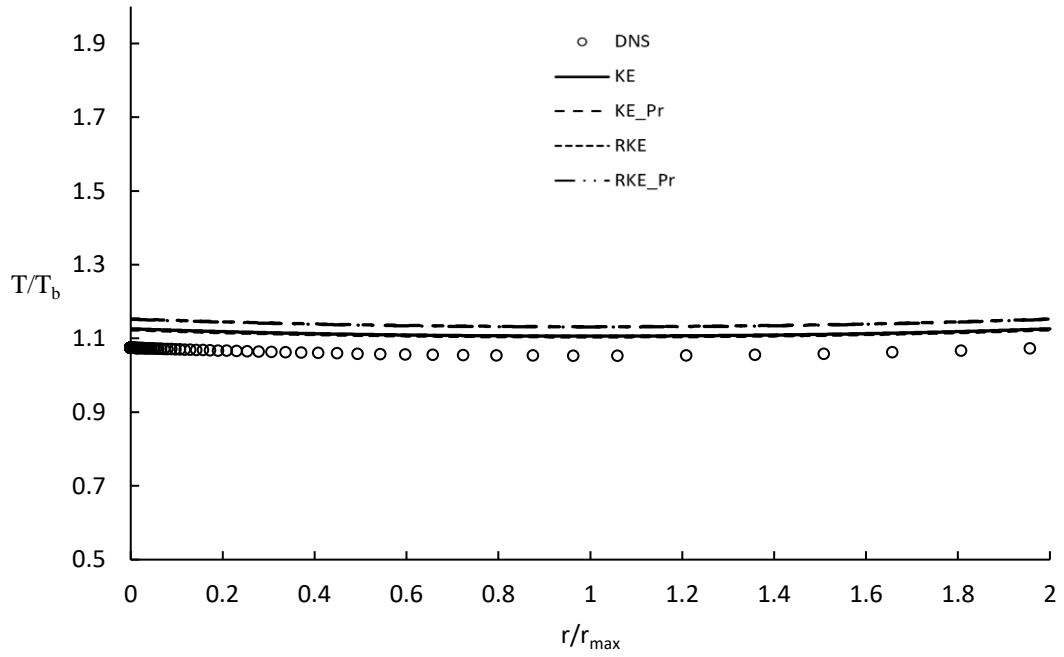
(a)
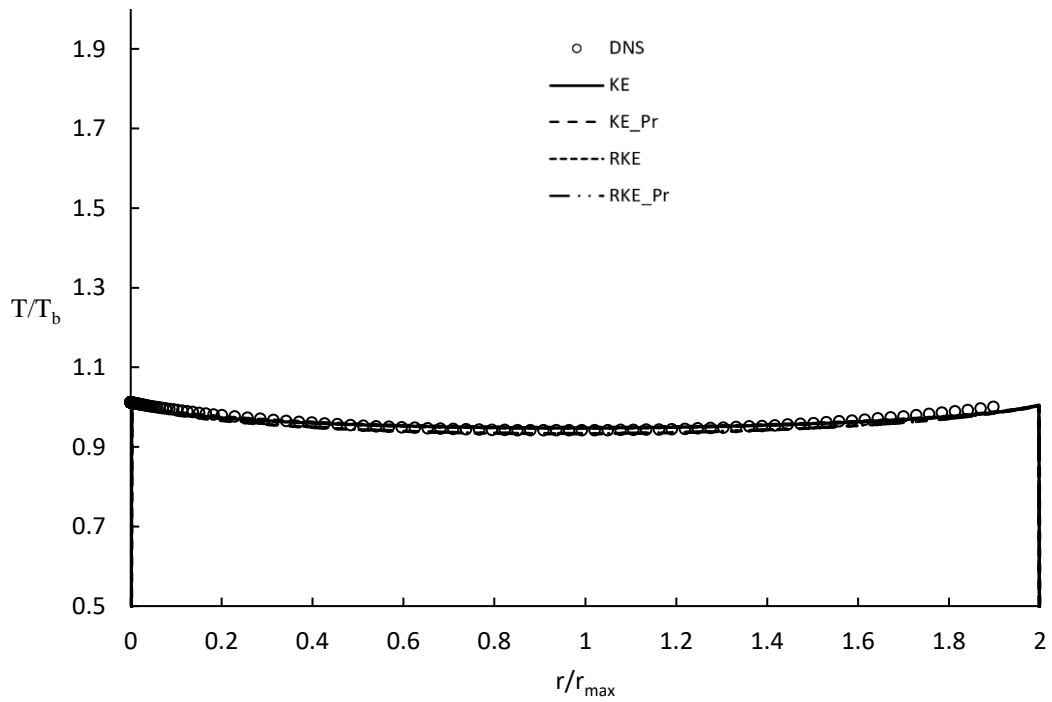
(b)

Figure 54: Non-dimensional temperature data for Pr=0.02 at (a) θ=0º (b) θ=45º

In Figure 54 the models show slightly different profiles than before, showing steeper gradients at the walls than DNS data indicates. However, the models have not exhibited behavior of the steep gradients at the walls that are so different than that of the DNS. This suggests that the DNS results in more turbulent mixing than the CFD results, which is why the models depict steeper gradients in the gaps and near the rod surface.
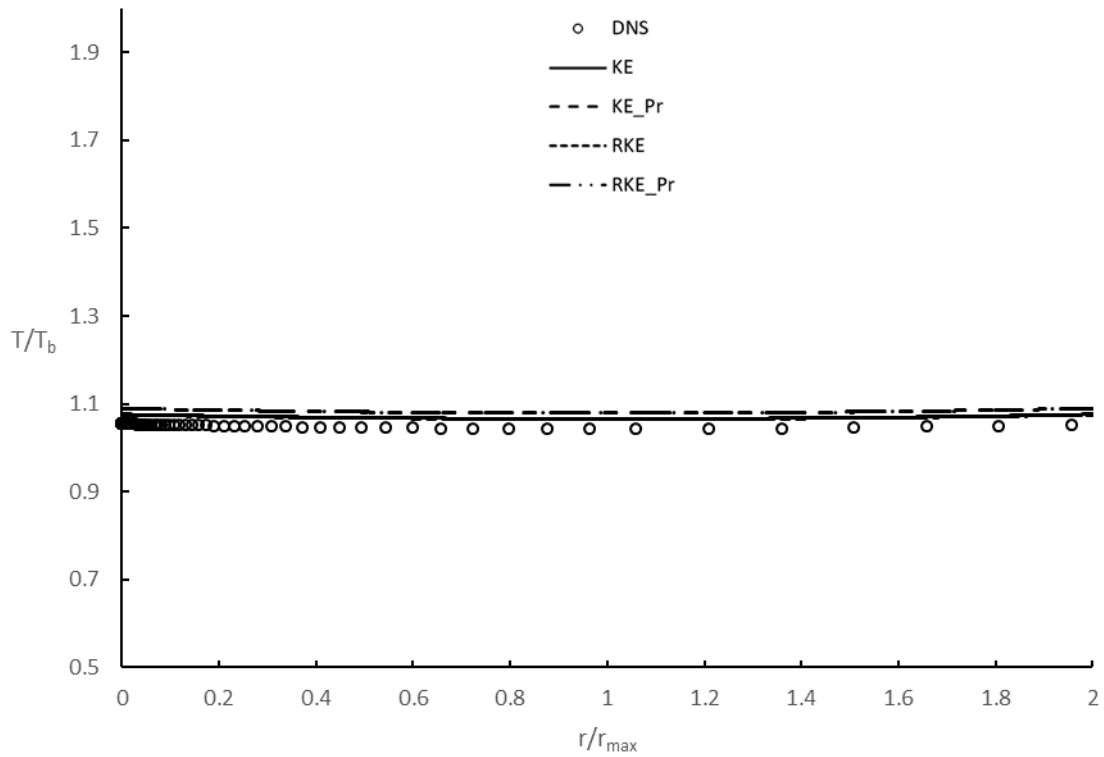
(a)
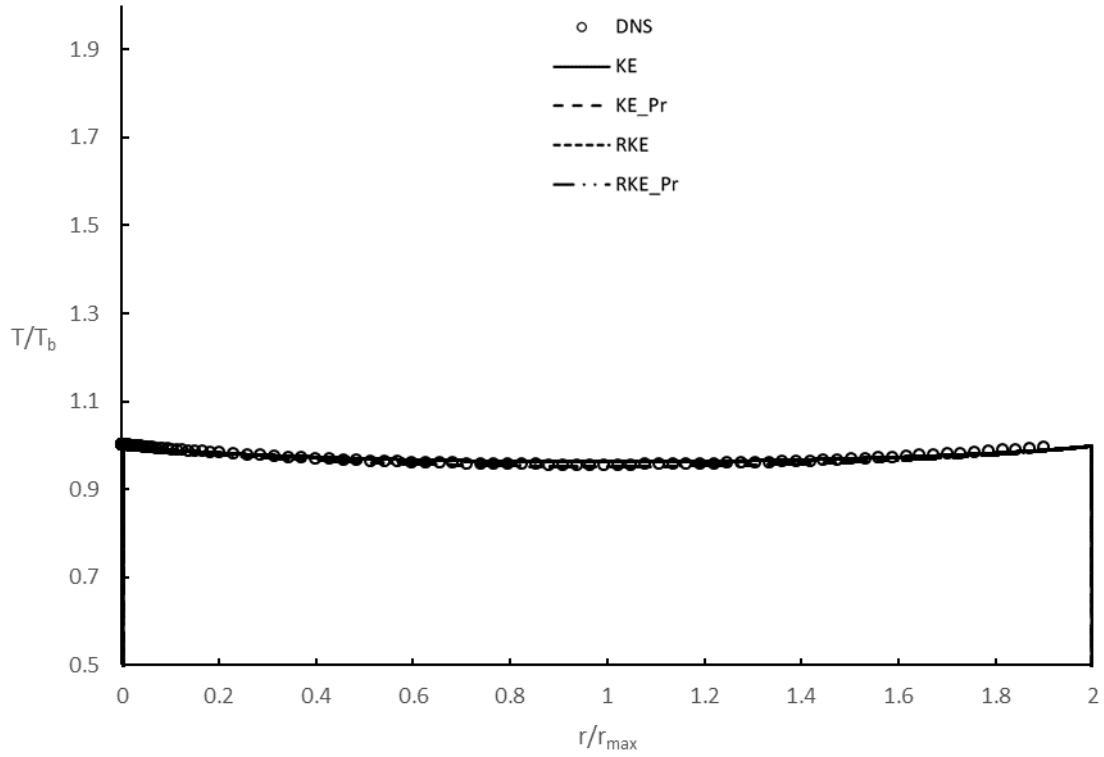
(b)

Figure 55: Non-dimensional temperature data for Pr=0.01 at (a) θ=0⁰ (b) θ=45⁰

As the Pr decreases the variation in temperature decreases due to how high the thermal diffusivity is relative to the other cases, in addition, causing much flatter profiles than that of the previous simulations. The trend of the models to overpredict the temperature at θ=0⁰ is still apparent just as they did at higher Pr numbers, only the effect it has is much smaller due to the thermal diffusivity.
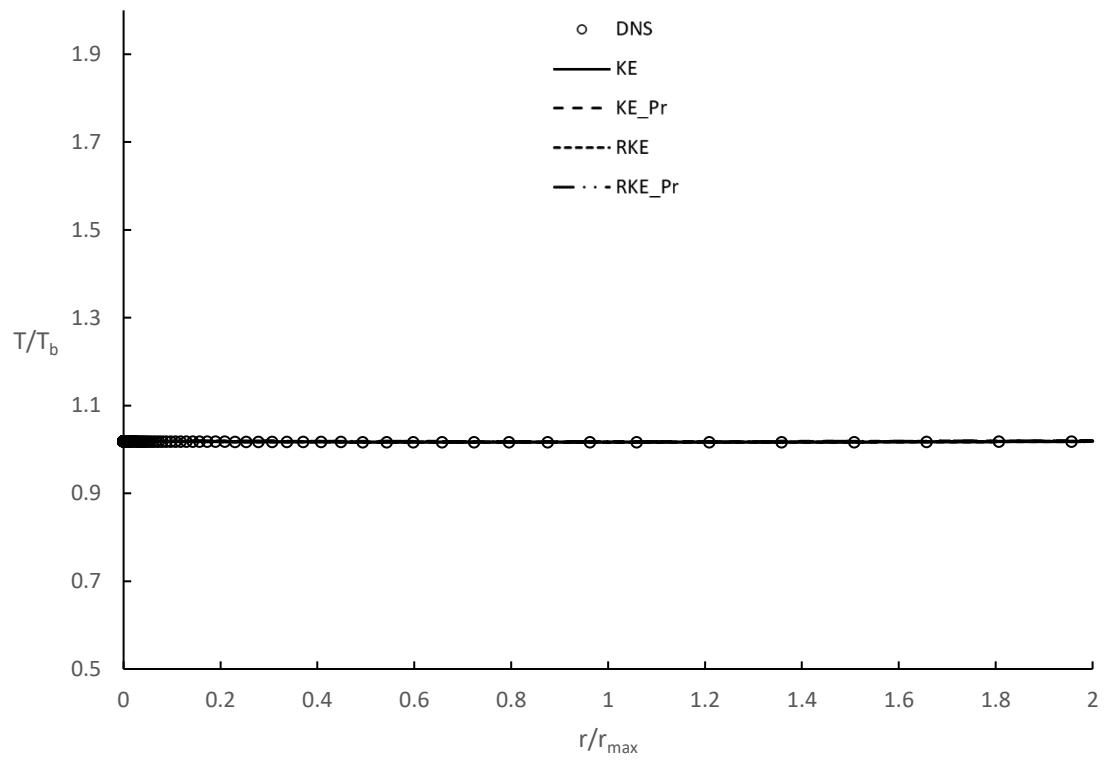
(a)
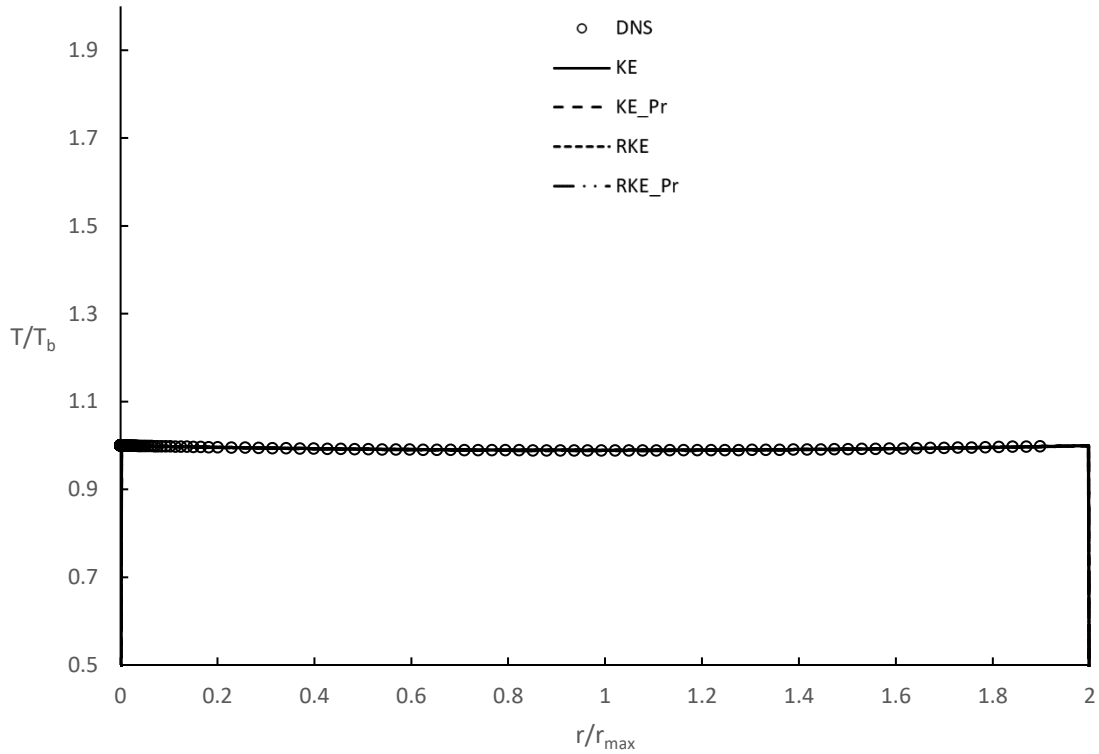
(b)

Figure 56: Non-dimensional temperature data for Pr=0.002 at (a) $\theta=0^o$ (b) $\theta=45^o$

Figure 56 shows data for the smallest value of Pr for the rod bundle geometry. Simulation results exhibit the same trends and behaviors as the previous values of Pr, however the issue of the fluctuations is small because of the obvious increase in thermal diffusivity.

All models seem to perform well in predicting velocity and temperature away from the gap between rods. Again, the isotropic assumption in the stress term for these RANS models causes issues when the highest stress component is tangent to the wall. Even though the profiles are largely the same, only shifted, some more testing with other RANS models without this assumption could potentially improve on the results presented in this study.

CONCLUSION

This document investigates the results of implementing and validating turbulence models for the purposes of evaluating low-Pr fluid flows. In addition to implementation, modifications were made to the models in the form of Kay's formulation, to achieve increased accuracy in computational solutions regarding fluids with low Pr. A standard and realizable k-ε model were tested with and without Kay's formulation to attempt to find a solution to modeling low-Pr fluids. Presented in this document are results ranging from simple channel geometries and backward facing step geometries, to a sample section for a square-lattice nuclear reactor rod bundle geometry. From all results laid out in this study:

- Simple RANS models such as k-ε and realizable k-ε models do not accurately predict the thermal flow field results for low Pr flows on their own.

- The models in conjunction with Kay's formulation better predicted thermal data for simulations involving low Pr flow. The models, even with this modification, do not appear to suffer any drawbacks for Pr that are close to air in accuracy or in computational cost.

- The RANS models investigated in this study do not show consistent agreement in regions with recirculation, as seen in the backward facing step results, and areas with low wall-normal stress and high tangential stress components, as exhibited by the results for the benchmark rod bundle geometry.

- Typical two equation RANS models may not be the most advantageous models to implement Kay's formulation due to their shortcomings with recirculation and the misprediction caused in areas with tight geometries when assuming isotropic stress components.

- The simplicity of Kay's formulation and how inexpensive it is to implement with respect to the overall improvement in accuracy for flows with low molecular Pr shows that it is an overall improvement on typical RANS models for low cost and effort.

FUTURE WORK

Though this study has shed some light on the applicability of turbulent heat flux modifications in low Pr fluid turbulence modeling, there are significant strides to be made. Improvement was made through a very small modification in the RANS codes presented in this document, however, Kay's formulation may see higher accuracy with more complex turbulence models, to include models that address non-isotropic stress components. Work stemming directly from this study include plans to run simulations using the k-ω SST model, as well as a Dynamic Hybrid RANS-LES model (DHRL). In addition to Kay's formulation, more complex turbulent heat flux models such as Algebraic Heat Flux Models (AHFM) are to be investigated.

LIST OF REFERENCES

Abe, H., Kawamura, H., and Matsuo, Y., 2004. "Surface Heat-Flux Fluctuations in a Turbulent Channel Flow up to Reτ=1020 with Pr=0.025 and 0.71." International Journal of Heat and Fluid Flow 25 (3): 404–419. doi:10.1016/j.ijheatfluidflow.2004.02.010.

Abe, K., and Kondoh, T., "A New Turbulence Model for Predicting Fluid Flow and Heat Transfer in Separating and Reattaching Flows. I. Flow Field Calculations," Int. J. Heat Mass Transfer 37, 139 (1994).

Abe, K., and Kondoh, T., "A New Turbulence Model for Predicting Fluid Flow and Heat Transfer in Separating and Reattaching Flows. II. Thermal Field Calculations," Int. J. Heat Mass Transfer 38, 1467 (1995).

Abram, T., and Ion, S., 2008. "Generation-IV Nuclear Power: A Review of the State of the Science." Energy Policy 36 (12): 4323–4330. doi:10.1016/j.enpol.2008.09.059.

Cheng, X., and Tak, N. I., 2007. Computational fluid dynamics analysis of heat transfer to heavy liquid metals in bare rod bundles. Nucl. Technol. 158, 229-236.

Fischer, P. F., Lee-Wing, H., Karniadakis, G. E., Rønouist, E. M., and Patera, A. T., 1988. "Recent Advances in Parallel Spectral Element Simulation of Unsteady Incompressible Flows." Computers & Structures 30 (1-2): 217–231. doi:10.1016/0045-7949(88)90228-3.

Ge, Z., Liu, J., Zhao, P., Nie, X., and Ye, M., 2017. "Investigation on the Applicability of Turbulent-Prandtl-Number Models in Bare Rod Bundles for Heavy Liquid Metals." Nuclear Engineering and Design 314: 198–206. doi:10.1016/j.nucengdes.2017.01.032.

Gibson, M.M., Dafa'Alla, A.A., 1995. Two-equation model for turbulent wall flow. AIAA J. 33 (August (8)), 1514–1518.

Grötzbach, G., 2013. "Challenges in Low-Prandtl Number Heat Transfer Simulation and Modelling." Nuclear Engineering and Design 264: 41–55. doi:10.1016/j.nucengdes.2012.09.039.

Heinzel, A., Hering, W., Konys, J., Marocco, L., Litfin, K., Müller, G., Pacio, J., et al., 2017. "Liquid Metals as Efficient High-Temperature Heat-Transport Fluids." Energy Technology 5 (7): 1026–1036. doi:10.1002/ente.201600721.

Hooper, J.D., and Wood, D. H., 1984. "Fully Developed Rod Bundle Flow over a Large Range of Reynolds Number." Nuclear Engineering and Design 83 (1): 31–46. doi:10.1016/0029-5493(84)90027-x.

Jones, W.P., and Launder, B. E., 1972. "The Prediction of Laminarization with a Two-Equation Model of Turbulence." International Journal of Heat and Mass Transfer 15 (2): 301–314. doi:10.1016/0017-9310(72)90076-2.

Kasagi, N., Tomita, Y., and Kuroda, A., 1992. "Direct Numerical Simulation of Passive Scalar Field in a Turbulent Channel Flow." Journal of Heat Transfer 114 (3): 598–606. doi:10.1115/1.2911323.

Kasagi, N. and Ohtsubo, Y., 1993, "Direct Numerical Simulation of Low Prandtl Number Thermal Field in a Turblent Channel Flow," in Turbulent Shear Flows VIII, F. Durst et al., eds., Springer-Verlag, Berlin, pp. 97-117.

Kasagi, N, and Nishimura, M., 1997. "Direct Numerical Simulation of Combined Forced and Natural Turbulent Convection in a Vertical Plane Channel." International Journal of Heat and Fluid Flow 18 (1): 88–99. doi:10.1016/s0142-727x(96)00148-8.

Kasagi, N. and Iida, O., 1999, "Progress in Direct Numerical Simulation of Turbulent Heat Transfer," Proceedings of the 5th ASME/JSME Joint Thermal Engineering Conference, San Diego, CA.

Kawamura, H., Abe, H., and Matsuo, Y., 1999. "DNS of Turbulent Heat Transfer in Channel Flow with Respect to Reynolds and Prandtl Number Effects." International Journal of Heat and Fluid Flow 20 (3): 196–207. doi:10.1016/s0142-727x(99)00014-4.

Kays, W. M., 1994. "Turbulent Prandtl Number—Where Are We?" Journal of Heat Transfer 116 (2): 284–295. doi:10.1115/1.2911398.

Kozelkov, A. S., Kurkin, A. A., Kurulin, V. V., Legchanov, M. A., Tyatyushkina, E. S., and Tsibereva, Y. A., 2015. "Investigation of the Application of RANS Turbulence Models to the Calculation of Nonisothermal Low-Prandtl-Number Flows." Fluid Dynamics 50 (4): 501–513. doi:10.1134/s0015462815040055.

Launder, B.E., and Spalding, D.B., 1974, "The numerical computation of turbulent flows", Computer Methods in Applied Mechanics and Engineering 3 (2), pp. 269–289.

Maciocco, Luca., 2002. "Assessment of Turbulence Models for Heavy Liquid Metals in Computational Fluid Dynamics" WP 7 of the ASCHLIM project.

Menter, F.R., 1994. Two-equation eddy-viscosity turbulence models for engineering applications. AIAA J. 32 (August (8)), 1598–1605.

Niemann, M., and Fröhlich, J., 2016. "Buoyancy-Affected Backward-Facing Step Flow with Heat Transfer at Low Prandtl Number." International Journal of Heat and Mass Transfer 101: 1237–1250. doi:10.1016/j.ijheatmasstransfer.2016.05.137.

Patera, A. T., 1984. "A Spectral Element Method for Fluid Dynamics: Laminar Flow in a Channel Expansion." Journal of Computational Physics 54 (3): 468–488. doi:10.1016/0021-9991(84)90128-1.

Rachkov, V. I., Sorokin, A. P., and Zhukov, A. V., 2018. "Thermal Hydraulic Studies of Liquid-Metal Coolants in Nuclear-Power Facilities." High Temperature 56 (1): 124–137. doi:10.1134/s0018151x18010145.

Reynolds, A.J., 1975. "The Prediction of Turbulent Prandtl and Schmidt Numbers." International Journal of Heat and Mass Transfer 18 (9): 1055–1069. doi:10.1016/0017-9310(75)90223-9.

Roelofs, F., Shams, A., Otic, I., Böttcher, M., Duponcheel, M., Bartosiewicz, Y., Lakehal, D., Baglietto, E., Lardeau, S., and Cheng, X., 2015. "Status and Perspective of Turbulence Heat Transfer Modelling for the Industrial Application of Liquid Metal Flows." Nuclear Engineering and Design 290: 99–106. doi:10.1016/j.nucengdes.2014.11.006.

Sommer, T. P., So, R. M. C., and Lai, Y. G., "A Near-Wall Two-Equation Model for Turbulent Heat Flux," Int. J. Heat Mass Transfer 35, 3375 (1992).

Thiele, R., and Anglart, H., 2013. "Numerical Modeling of Forced-Convection Heat Transfer to Lead–Bismuth Eutectic Flowing in Vertical Annuli." Nuclear Engineering and Design 254: 111–119. doi:10.1016/j.nucengdes.2012.09.006.

Vogel, J. C., and Eaton, J. K., 1985. "Combined Heat Transfer and Fluid Dynamic Measurements Downstream of a Backward-Facing Step." Journal of Heat Transfer 107 (4): 922–929. doi:10.1115/1.3247522.

Weigand, B., Ferguson, J. R., and Crawford, M. E., 1997. An extended Kas and Crawford turbulent Prandtl number model. Int. J. Heat Mass Transfer. 40, 4191-4196.

Wolfshtein, M. 1969. "The Velocity and Temperature Distribution in One-Dimensional Flow with Turbulence Augmentation and Pressure Gradient." International Journal of Heat and Mass Transfer 12 (3): 301–318. doi:10.1016/0017-9310(69)90012-x.

Yuan, H., and Merzari, E., 2015. "Direct Numerical Simulation of Turbulent Channel Flow with Heat Transfer for Low Prandtl and High Reynolds and Comparison With Algebraic Heat Flux Model." Volume 1: Symposia. doi:10.1115/ajkfluids2015-8740.